NTNU
Norwegian University of
Science and Technology

The Effect of Rapid Solidification on Ti-Zr Alloys for Application in Ni-MH Battery Anodes

Live Mølmen

Materials Science and Engineering (MTMT)
Submission date: June 2018
Supervisor: Ann Mari Svensson, IMA
Co-supervisor: Hans Jørgen Roven, IMA

Norwegian University of Science and Technology
Department of Materials Science and Engineering

Preface

This Master's thesis is written at NTNU Department of Materials Science and Engineering in the spring of 2018 and is a continuation of the specialization project of the fall semester, and so the results of both are discussed in this thesis. The project is a collaboration with PhD-student Ika Dewi Wijayanti. The metallurgical part of the project has been performed at NTNU, while the electrochemical characterization has been performed at the Institute of Energy Technology (IFE) under the supervision of professor Volodymyr Yartys. Furthermore, the melt spinning experiments were performed at CNRS-ICMCB in Bordeaux in the fall semester as the melt spinner at NTNU was not yet installed.

A Master's thesis is not made in solitude. First and foremost I want to thank my main supervisor, Volodymyr Yartys, for aid and guidance throughout the project and master work, both in discussing the results and in shaping the thesis, and motivation for always pursuing a deeper understanding of the processes that have been studied.

Furthermore, I owe a huge thank you to PhD-student Ika Dewi Wijayanti at NTNU and IFE for the collaboration on this project, for the time spent together in the lab working on the analysis and the fruitful discussions of our results, and shared frustrations whenever obstacles were met.

I am grateful for the opportunity to travel to CNRS-ICMCB in Bordeaux to perform the melt spinning in the fall, and want to thank the professors Stephane Gorsse and Jean-Luis Bobet as well as Christoph Cona for their time working on the experiments, and aid in the analysis of the ribbons. I also want to express my gratitude to my supervisors at NTNU: Ann Mari Svensson for helping me when writing this thesis and Hans Jørgen Roven for the metallurgical part of the project. I want to thank David Eide Brennhaugen and Jonas Einan Gjøvik for the help with the melt spinning experiments, and Trygve Lindahl Schanke, Yingda Yu and Kristin Høydalsvik Wells for the aid in the characterization of the samples, as well as Roman V. Denys for the help with the experiments at IFE.

Lastly, the writing of this thesis would not have been the same without the shared laughter and aid of my fellow students, both at NTNU and in the student office at IFE.

FME MoZEES is acknowledged for the funding of the project.

Live Mølmen
11.06.2018, Trondheim

Sammendrag

Metallhydrider er en gruppe materialer brukt for lagring av hydrogen og som anodematerialer i nikkelmetallhydridbatterier(Ni-MH). Egenskapene til disse materialene kan tilpasses gjennom valg av legeringselementer og kontroll av mikrostrukturen. Det overordnede målet for utvikling av metallhydrider er å produsere materialer med høy hydrogenlagringskapasitet, rask og reversibel hydrogenabsorpsjon og -desorpsjon, justerbar fasestabilitet (absorpsjon/desorpsjon av hydrogen ved 1 atm trykk i Ni-MH batterier) i tillegg til korrosjonsbestandighet også i kontakt med en 6-9 M KOH elektrolytt.

Formålet for dette prosjektet har vært å studere effekten av hurtigstøpning som en metode for å oppnå en nanostruktur, og undersøke de elektrokjemiske egenskapene for dette materialet i anoden i et Ni-MH batteri. Hovedfokuset var å forbedre utladningskapasiteten for batteriet også ved høyere strømtetthet. Legeringen som ble brukt er en TiZr-basert AB_2 Laves-faselegering, ettersom denne gruppen legeringer har et betydelig redusert innhold av sjeldne jordartsmetaller sammenlignet med de kommersialiserte legeringene brukt i dag, som er basert på $LaNi_5$ systemet.

Med utgangspunkt i tidligere eksperimenter utført ved IFE, ble to legeringer med sammensetning $(Ti_xZr_{1\text{-}x}La_y)(Ni_{1.2}Mn_{0.7}V_{0.12}Fe_{0.12})$ valgt, hvor x=0,15 og y=0,03 ble satt som legering 1, og x=0,20 og y =0,01 ble valgt som legering 2. Begge legeringene inneholder en liten tilsetning av La for å oppnå raskere aktivering av materialet.

Den høye avkjølingshastigheten be oppnådd ved hjelp av en smeltespinner, med overflatehastigheter under utstøpingen mellom 3,1 og 62,8 ms^{-1}. Det ble slått fast at smeltespinningen fører til ett tap av Mn fra smelten, så forsøk ble også gjort for å undersøke effekten av ekstra Mn-tilsetning for å kompensere for dette. Effekten av hurtigstørkning på mikrostruktur og fasesammensetning ble studert ved hjelp av SEM, EDS, AES og XRD. Videre ble de elektrokjemiske egenskapene til materialet studert ved voltametrisk sykling med varierende strømtetthet, EIS og PCT.

SEM mikrografiene viser en vellykket reduksjon i kornstrukturen ved hurtigstørkning. Kornstørrelsen ble gradvis redusert fra den opprinnelige 2 μm til rundt 250 nm for de raskest størknede materialene. Morfologien til legering 1 gjennomgikk en isotrop reduksjon i kornstørrelse i tillegg til at det ble dannet partikler av en sekundær fase på korngrensene. Legering 2, derimot, viste dannelse av en lamellær struktur ved høyere avkjølingshastighet.

Begge legeringene består av en blanding av to Laves-fasestrukturer, nemlig kubisk C15 og heksagonal C14. Den foretrukne C15 strukturen er dominant før smeltespinning, men andelen C14 øker etter smeltespinning. EDS og XRD bekrefter at hovedfasen sett i SEM er C15, mens den sekundære fasen er C14.

De elektrokjemiske resultatene viser at smeltespinningen har resultert i treg aktivering av anodene. I tillegg viser det seg at legering 2 har tregere aktivering enn legering 1, og har ett skrått potensialplatå.

Test av kapasiteten til anodematerialene ved høy strømtetthet viser at smeltespinning er en god måte å forbedre kapasiteten til Ni-MH batterier ved høyere strømtettheter, som et resultat av reduksjon av kornstørrelsen som forbedrer diffusjonen av hydrogen inn i materialet.

Abstract

Metal hydrides find applications in the storage of hydrogen and also as anode materials for the nickel-metal hydride batteries(Ni-MH). The properties of these materials can be tuned by selecting appropriate elemental composition and by controlling the microstructure. The overall goal in the development of advanced metal hydrides is to obtain materials with high hydrogen storage capacity, fast and completely reversible hydrogen absorption and desorption, and tunable phase stability (with an adsorption/desorption pressure around 1 bar at ambient conditions for the Ni-MH batteries), as well as good stability in the working environment (6-9 M KOH electrolyte in Ni-MH batteries).

The goal of the present work was to study the effect of rapid solidification(RS) as a nanostructuring technology applied to obtain novel and improved anode materials for the Ni-MH battery. The focus of the work was on the TiZr-based AB_2 Laves phase alloys, which contain significantly less rare earth metals (RE) compared to the commercialized alloys used today, which has the composition ($RE(Ni,Co)_5$). The alloys were melt spun to obtain a grain refinement, and consequently improve the discharge capacity and high rate discharge performance of the alloys.

Based on earlier experiments performed at IFE, two basic alloys with compositions $(Ti_xZr_{1\text{-}x}La_y)(Ni_{1.2}Mn_{0.7}V_{0.12}Fe_{0.12})$ were chosen. Particular compositions were selected as x=0.15, and y=0.03 (Alloy 1), and x=0.2 and y=0.01 (Alloy 2). Both alloys contain minor amounts of La to help achieving fast activation of the material.

The alloys were melt spun, with wheel surface speeds varying from 3.1-62.8 ms^{-1}. As the melt spinning process proved to modify the alloy composition, resulting in depletion of Mn which is easily vaporized, the effect of excess Mn addition to mitigate this problem was also studied for alloy 1. The effect of RS on the microstructure and phase compositions was characterized by using SEM, EDS, AES and XRD. Furthermore, the electrochemical properties were studied through electrochemical cycling performed at different current densities as well as by electrochemical impedance spectroscopy and PCT.

The SEM studies showed a successful refinement of the microstructure by RS. The grain size gradually decreased from the original 2 μm in the as cast alloys to around 250 nm for the alloys melt spun with the highest cooling rate. The morphology of alloy 1 showed an isotropic reduction in grain size with RS, with a related formation of small particles of the secondary phases at the grain boundaries. Alloy 2, on the other hand, showed a formation of a lamellar structure after the melt spinning.

The XRD data show that both alloys contain a mixture of two Laves phase compounds; cubic C15 and hexagonal C14 structure. The preferred C15 crystal structure is dominating for the initial alloys. RS however increases the amount of the C14 phase. The EDS and XRD results confirm that the main phase observed in the SEM micrographs corresponds to the C15 phase, while the particles or secondary phase consists of the C14 crystal structure. Electrochemical results showed that RS casted samples have a more sluggish activation performance. Furthermore, alloy 2 proved to have more sluggish activation than alloy 1, as well as a sloped working potential.

Lastly, for alloy 1, the high rate of discharge performance was improved by RS, as there is an increase in capacity for all tested current densities. This is a result of the refined microstructure leading to an increased diffusion coefficient of H through the material.

Contents

1. Introduction

When the main car manufacturers released their first hybrid electric vehicles at the beginning of the 1990's, one of the dominating battery technologies was the nickel metal hydride(Ni-MH) battery. It is both lighter and more environmentally friendly than the lead-acid battery that had been, and still is in use for gasoline and petrol fueled cars. Toyota even uses Ni-MH batteries in their very popular Prius hybrid cars today, although they now have the option to chose Li-ion batteries instead. However, the large amount of Toyota Priuses that are still in use today, both by private car owners and taxi drivers around the world is a statement to the durability and safety of the Ni-MH battery[1, 2].

The Ni-MH battery has in many applications replaced the NiCd battery, which was a dominating battery technology before the production has become limited in the later years due to the toxicity of cadmium. The Ni-MH is very similar to NiCd batteries, and even utilizes the same cathode based on NiOOH. The metal hydride is however less toxic than the cadmium anode, and utilizes some more abundant elements like nickel, manganese and iron, which also lowers the material cost.

Even though the Ni-MH battery has proved to be reliable over the years, it must be continually improved to keep up with the rapidly evolving battery technologies. The main criteria when choosing batteries is the energy and power density as well as the cost of the battery. The metal hydride anode is both the most expensive and the heaviest component of the Ni-MH battery[3], and it is therefore the area of research on these batteries where new advances is the most needed.

The most common anodes used commercially today are based on the AB_5 composition, with the model alloy $LaNi_5$. The A atoms are larger atoms, mainly rare earth metals, while the B atoms are smaller transition metals. These alloys have a good cycle life and a high discharge capacity of 330 $mAhg^{-1}$[4]. Studies have been made attempting to use cheaper metals in the AB_5 stoichiometry[3]. While the cost has been successfully reduced, the discharge performance of these anodes is equal to, or slightly under that of the more expensive anodes. The price reduction is therefore not enough to favor the use of these anodes. In addition, the large amount of rare earth metals is undesired, as they are expensive and there is a limited supply of these elements. Hence, new compositions are being studied. The main focus areas are either Mg-Ni based AB_3 or Ti-Zr based AB_2-stoichiometric alloys[3]. The latter will be the topic of this thesis.

In an earlier study by Wan et al.[5], alloys with the AB_2 stoichiometry with composition $(Ti_xZr_{1-x}La_y)(Ni_{1.2}Mn_{0.70}V_{0.12}Fe_{0.12})$ proved to have discharge capacities of up to 434 $mAhg^{-1}$. However, the discharge capacity of the alloys decrease significantly when the current density is increased. It has been suggested that a nanocrystalline microstructure can improve the capacity of the anode also at higher current densities by increasing the amount of grain boundary and producing a more homogeneous phase distribution in the electrode. Rapid solidification processing is a common method to produce nanocrystalline materials.

Objectives of the Master Work

This thesis is a continuation of the work by Wan et al.[5] and will therefore study the same alloy, with four main objectives:

1. Study the effect of rapid solidification on the $(Ti_xZr_{1-x}La_y)(Ni_{1.2}Mn_{0.70}V_{0.12}Fe_{0.12})$ alloys with respect to phase composition and morphology.
2. Improve the discharge capacity of the alloys
3. Improve the high rate discharge ability of the alloys
4. Analyze the reaction mechanism of this type of metal hydride anodes

2. Theoretical Background

This chapter provides the theoretical background necessary for the discussion of the results in this thesis. It is assumed that the reader has a basic knowledge of materials science. The chapter is separated into four main parts: batteries, the AB_2 metal hydrides, solidification, and characterization techniques.

2.1 Batteries

A battery is a term used for devices that chemically store energy. When attached to an external circuit, the battery will release the energy through a chemical reaction, creating an electric current. In general, the three main parts of the battery is the two electrodes and the electrolyte. The two electrodes are also called the anode and the cathode, depending on which way the the electrochemical reactions are going. Through a spontaneous reduction and oxidation reaction at the electrode surface, an electron and an ion are released. A porous separator between the electrodes allows for conduction of the ions in the electrolyte from the anode to the cathode, while the electrons go through the external circuit, where they perform electrical work like power a light bulb, or the propulsion of a car.

2.1.1 Comparison of Battery Technologies

Batteries are divided into primary and secondary batteries, where the primary batteries have irreversible reactions, while the secondary batteries have reversible reactions and can therefore be recharged. Battery technologies have been strongly improved in the later years, and as green energies are sought after, and the need to store larger amounts of energy only increases, the advancement in the technology will continue . Secondary batteries are now smaller and lighter, as well as have longer lifetime both with respect to being stored for a longer time (shelf life) and going through numerous charge-discharge cycles (cycle life). Thus, the secondary batteries have become an invaluable part of the modern society.

By choosing different chemistries for the anode and the cathode, batteries can be tailored towards high power density and high energy density. When comparing different batteries the main focus is three main parameters: the potential, the gravimetric density (density by weight) and the volumetric density. As the potential can be adjusted by adding several batteries in series, the two latter are often plotted against each other to analyze and compare the different types of batteries. A plot of this is presented in Figure 2.1. From the figure, it is clear that Li-ion batteries are superior to other battery chemistries when it comes to both volumetric and gravimetric density. Thus, most of new batteries for portable applications today have the Li-ion chemistry.

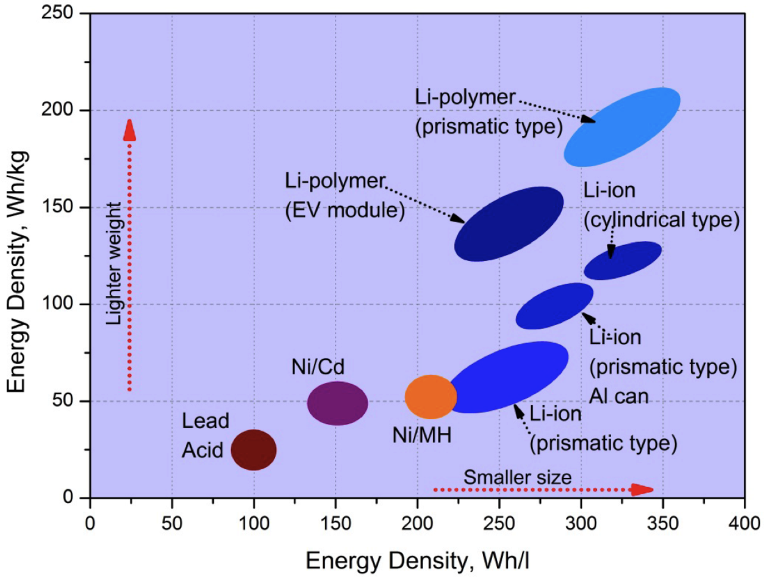

Figure 2.1: Comparison of different batteries with respect to volumetric and gravimetric energy density [6]

A common problem with many batteries is parallel reactions occurring, especially when the battery is completely charged or discharged. Depending on the type of batteries, these reactions can either form solid phases that may short-circuit the battery, or undesired gases. An example of this is the Li-ion batteries. If these batteries are overcharged, gas evolution will occur. These gases are highly inflammable, and as the reactions are exothermic, the temperature will increase, eventually leading to thermal runaway. Li-ion batteries therefore require circuits to avoid overcharging as well as a cooling system so that the battery does not overheat. For applications where high power is more important than weight, Ni-MH batteries may therefore be a better choice[7]

2.1.2 The Electrode Reaction

When studying the reactions in the battery, one has to separate them into the reactions on each electrode, called the half reactions, and the different transport mechanisms. The general half reaction is written:

$$\mathrm{O} + \mathrm{ne}^- \rightleftharpoons \mathrm{R} \tag{2.1}$$

where O is the oxidizing species, R is the reducing species, and n is the number of electrons being transferred in the reaction. As with all chemical reactions the free energy of the system is the key to determine which reactions will occur, and in electrochemistry also to finding the electrochemical potential. This is done through the relation:

$$\Delta G = \Delta G^0 + RTln\frac{[R]}{[O]} = -nFE \tag{2.2}$$

where ΔG^0 is the standard free energy of the system, R is the gas constant, T is temperature in K, $[R]$ and $[O]$ are the concentrations of the reducing and oxidizing species, respectively, F is Faraday's constant and E is the potential. It should be noted that the activity of the reducing and oxidizing species are assumed to be equal to their respective concentrations. By rearranging this equation, and defining E^0 as the potential at standard conditions, the potential as a function of only the concentrations can be written as:

$$E = E^0 + \frac{RT}{nF}ln\frac{[R]}{[O]} \tag{2.3}$$

This is the Nernst equation[8]. In a battery, there are many different chemical species present, resulting in several competing half reactions. As the free energy of the system is the driving force, and a larger change in free energy results in a larger potential difference, the two half reactions with the largest difference in potential will be dominating in an ideal battery.

In addition to considering the potential of the reactions in the battery, the current being passed through the battery must be accounted for. When discussing the current with respect to the electrodes, it is common to use the term current density. As the chemical reactions occur on the electrode surface, the current density is defined as the current divided by the area of the electrode, or alternatively on the weight of the electrode if it is porous. When the current is passed through the battery, a series of different reaction steps occur, all together described as the reaction mechanism. There are four main reaction steps of the total reaction mechanism that can limit the rate, which further determines the maximum current. These are the diffusion of the reacting species to the electrode surface, chemical reactions before and after the charge transfer reaction, the charge transfer reaction and adsorption/desorption reactions[8]. This is illustrated in Figure 2.2.

The diffusion step is rarely rate determining in a battery as the electrolyte is sufficiently concentrated. However, an ohmic loss in potential will always be present due to the electrolyte resistance[7]. On the other hand, the absorption of reactants can be slow, or hindered by slow desorption of the reaction products effectively blocking the surface. Also the diffusion of the reaction products into the electrode may be the rate limiting step.

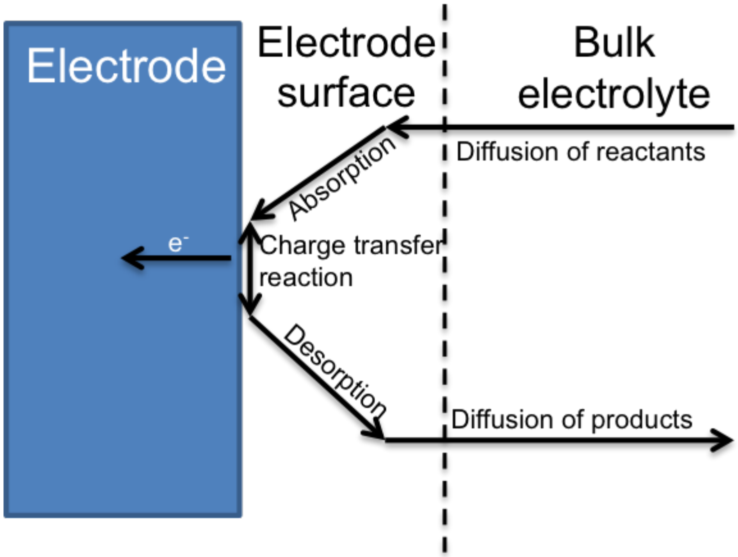

Figure 2.2: An example of process steps involved in the electrode reaction. Figure adapted from [8]

Each step in the reaction mechanism leads to resistances and capacitances in the batteries, which further causes potential drops. These potential drops are defined as overpotentials. In a real electrochemical system it is the potential difference which can be found from Equation 2.3 summed with the overpotential that determines which half-reactions will be dominating, as well as which total electrochemical potential can be extracted from the battery.

2.1.3 The Nickel-Metal Hydride Battery

As the names indicates, the cathode of these batteries are nickel based, more specifically NiOOH, which reacts with the electrolyte to take up hydrogen to form $\mathrm{Ni(OH)_2}$. The anode is a metal hydride. This in an intercalation electrode, meaning that the hydrogen atoms take take up interstitial sites in the metal crystal structure. The reaction equations for the Ni-MH battery are:

$$\begin{aligned} Cathode &: \mathrm{Ni(OH)_2 + OH^-} \underset{\text{Discharge}}{\overset{\text{Charge}}{\rightleftarrows}} \mathrm{NiOOH + H_2O + e^-} \\ Anode &: \mathrm{M + H_2O + e^-} \underset{\text{Discharge}}{\overset{\text{Charge}}{\rightleftarrows}} \mathrm{MH + OH^-} \\ Total &: \mathrm{Ni(OH)_2 + M} \underset{\text{Discharge}}{\overset{\text{Charge}}{\rightleftarrows}} \mathrm{NiOOH + MH} \end{aligned} \tag{2.4}$$

and a schematic of the battery can be seen in Figure 2.3

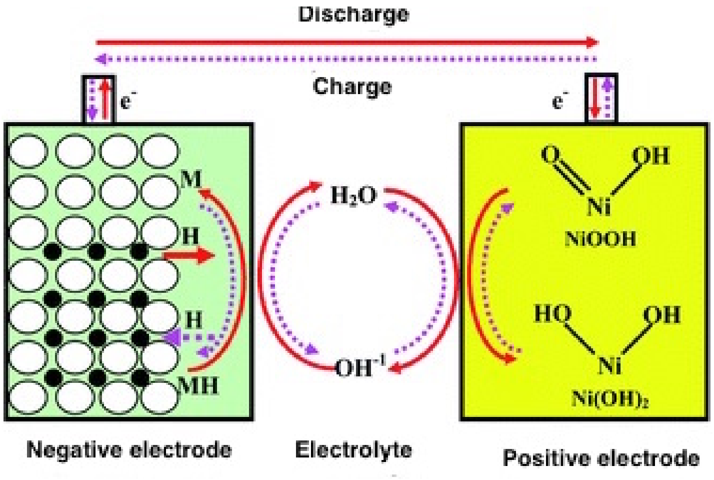

Figure 2.3: Schematic of a Ni-MH battery. Figure from [9]

2.2 The AB_2 Metal Hydrides

2.2.1 Laves Phase Crystal Structures

There are two main crystal structures for the AB_2 system of metal hydride alloys. These are both Laves phases, which are a group of layered crystal structures. Every other layer has either a Kagome 6363 geometry based on B atoms or a buckled net of A and B atoms[10], as can be seen in Figure 2.4a, where A, B and C are the Kagome nets, and a, b and c are the triangular buckled nets. By stacking these in different ways, new crystal structures are formed. The two most common stacking sequences are AcBc forming a hexagonal unit cell that is called C14, and AcBaCb which forms a face centered cubic structure called C15[4]. The stacking sequences are shown in Figure 2.4b and c, respectively.

Which of the two crystal structures dominates for a specific alloy, is dependent on the composition. The A atoms have a larger atomic radii and fewer valence electrons compared to the B atoms. The ratio of B/A atoms is therefore one of the key parameters to adjust the amount of C15 to C14, and it has been found that C15 is more dominant for hyperstoichiometric alloys, i.e. when $B/A > 2$[4]. One of the reasons for this is the geometric factors derived directly from the atomic radii. Furthermore, several studies have concluded that the main parameters determining the phase composition of the Laves phases is the average electron density, e/a[4, 11, 12]. According to the study by Nei et al.[12] the transition region between the C14 and C15 crystal structure for Zr dominated AB_2 alloys is for e/a somewhere between 6.8 an 7.0. This further explains why a hyperstoichiometric alloy, which has an excess of atoms with many valence electrons, are more stable in the C15 structure.

The main reason why the Laves phase crystal structures are desired for the metal hydride

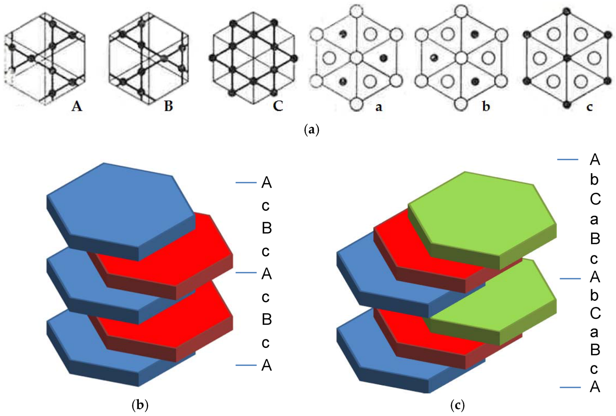

Figure 2.4: (a)Layer units for the AB_2 Laves phase crystal structures. The black points are B atoms while the circles are A atoms. The stacking of these layers for (b) the C14 and (c) the C15 crystal structure. Figure from[4].

anode is their ability to store hydrogen atoms. Due to the variation in atomic size of the different alloying elements, there is an abundance of relatively large interstitial sites which the hydrogen atoms can occupy. The tetrahedral interstitial sites of the C14 and C15 crystal structures are shown in Figure 2.5. The probability for a H-atom to occupy a free interstitial site is dependent on the neighboring atoms. The A_2B_2 sites are proven to be filled before the AB_3 and the B_4, respectively. This is mainly because the A_2B_2 sites are the largest due to the two adjacent A-atoms, and the sites are filled in decreasing order related to their size[13]. In addition, occupancy of one interstitial site will negate occupancy of a neighboring interstitial site if they share a triangular interface. This results in a theoretical maximum H-storage for C14 and C15 of 6.33 and 7 H per AB_2 unit, respectively[4].

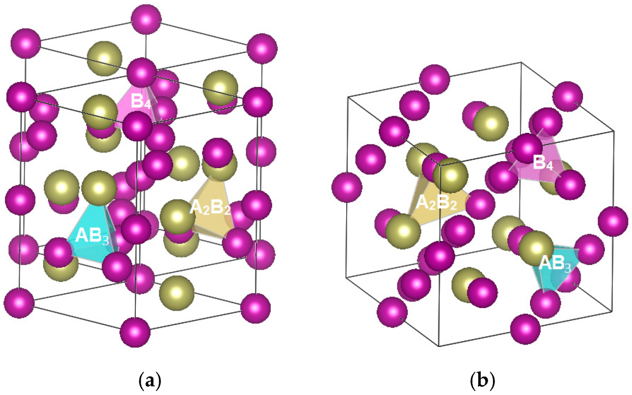

Figure 2.5: The unit cell of (a) C14 and (b) C15. The colored tetrahedra show the three different interstitial sites which the hydrogen atoms may occupy.[14]

While many studies have compared C14 and C15 to find the best crystal structure for use in Ni-MH batteries, the results are not consistent. The assumption can therefore be made that the microstructure and chemical composition of the alloy is equally if not more important for the H-storage performance of the hydride[4].

2.2.2 Metal Hydrides for Ni-MH Batteries

When the metal allo is used as a metal hydride anode, one has to consider the reactions and phase transitions occurring during the charge-discharge cycles of the battery. The metal alloy will generally be crushed to a fine powder before being pressed with a current collector to form the electrode to secure sufficient conductivity. It is therefore common to assume the presence of spherical metal hydride particles when discussing the kinetics of the metal hydride anode[15]. When the battery is charged, the anode goes through a phase transition from the metal phase, called the α-phase, to the metal hydride β-phase[16]. In the previous section, it was stated that the H-atoms occupy the interstitial sites of the metal crystal structure. As more and more interstitial sites are filled, there will be a volume expansion of the unit cell due to the phase transition from α- to β-phase. In the initial cycle, this volume expansion may cause cracking of the particles as the core will be α-phase while the outer shell of the particle already is expanded to the β-phase. New surface will then be exposed, and the hydrogenation of the next layer of the particle can begin. However, rarely does the whole particle go through the full phase transition in the first cycle, and so several cycles are required for sufficient cracking of the particle to occur for the complete phase transition to finish. This is called the activation period, and it is common to cycle a battery at least 3-5 times before full activation is reached [4, 11]

When the alloy is fully activated, it is possible to analyze the reaction mechanism of the metal hydride anode. It is common to describe the reaction mechanism of charging in the five following steps[15]:

1. Transport of H_2O molecules to the metal surface.
2. Volmer step: Splitting of water to H_{ads} and OH^- with the transfer of one electron.
3. Absorption of the H_{ads} into an interstitial site in the crystal lattice of the surface layer of β-phase.
4. Diffusion of interstitial H_i to the α-β interface.
5. Phase transition from the α to the β-phase.

The shrinking core model for the phase transition is here assumed, where the surface layer is first transformed to the β phase before it starts to expand into the center of the particle.

2.2.3 Alloying Effects

The alloys used for metal hydrides have complex compositions. By changing the elemental composition of the alloy, the thermodynamic stability of the metal hydride phase will change, and the hydrogen absorption and desorption ability of the alloy, mainly observed by the plateau pressure of hydrogen absorption and desorption, will be adjusted[16]. One of the advantages of the AB_2 system is the flexibility to adjust the phase composition without a change of crystal structure[17]. The balance between the A and B atoms, as well as e/a are, as explained earlier, crucial for the stability of the crystal structure. However, the substitution of different A and B atoms will change both the electrochemical properties, as well as the cost, availability and recyclability of the final product.

Rare earth metals are gradually being replaced by other, more readily available metals. In the AB_2 system La is substituted by Ti and Zr. However, a small amount of La is kept in the alloy as it stabilizes the plateau pressure of hydrogen absorption[18]. In addition, it has been proved that La increases the surface exchange current due to an increase in surface area, effectively increasing the high rate of discharge(HRD) performance of the alloy[4].

Of the two other A-elements, Zr has proved to be advantageous to improve activation properties and avoid oxidation occurring on the anode, thereby improving the cycle life of the battery[19]. Ti on the other hand has been found to oxidize easily, thereby being a source of corrosion in the battery[19]. However, the oxide is porous, and so it does not passivate the metal surface after formation[11]. In addition, Zhang et al.[20] found that the unit cell volume increases with Ti content for Laves phase alloys. This was, explained by the Ti atoms partially occupying B sites when added in larger concentrations. As Ti has a smaller atomic radius compared to Zr, as seen in Table 2.1, the Ti will go from the A to the B positions when the alloy is understoichiometric. However, Ti has a larger radius than the other B-elements, and so the addition of Ti into the B sites will naturally enlarge the unit cell.

For the B-elements, the major component is Ni. One of the reasons is that nickel is cheaper than many other metals, and as it also is present in the cathode and often used as the current collector for the anode, several studies has shown a potential for recycling the Ni from used Ni-MH batteries[21, 22]. Mn forms a very stable hydride, an thus increases the amount of H absorbed in the alloy and improve the charge capacity[23], although it might hinder the desorption of H if it is added in excess, hence having the opposite effect on the discharge capacity[24]. In addition, the solubility of larger alloying elements is improved by the addition of Mn. Hence, less segregation of the heavier elements[24]. Improved activation by increased pulverization during cycling[23] is also an argument for why Mn is one of the major constituents of the alloy.

Small additions of V and Fe are also added to the alloy. Fe, in addition to being cheap, is important to improve the plateau region of the anode as well as decreasing the hysteresis[25]. Furthermore, Fe is advantageous for the activation performance of the alloy[19, 25]. Similarly to Mn, V forms a very stable hydride, and so it improves the absorption of H by the alloy, but has a negative effect on the discharge capacity[26].

Table 2.1: Table showing the metallic radius and melting temperature of each alloying element as well as the vapor pressure of the elements at a temperature of 1400 K, which corresponds to approximately the casting temperature of rapid solidification.[27, 28]

Element	Metallic radius, pm	Melting temperature, °C	Vapor pressure, atm
Ti	145	1660	$9.33 * 10^{-11}$
Zr	159	1852	$1.22 * 10^{-14}$
La	187	920	$5.15 * 10^{-10}$
Ni	125	1455	$4.82 * 10^{-9}$
Mn	137	1244	$3.01 * 10^{-4}$
V	131	1910	$5.10 * 10^{-12}$
Fe	124	1535	$1.42 * 10^{-8}$

2.3 Solidification

The final properties of a material is a product of many factors, like the elements it contains and the shape of the final product, as well as the solidification and subsequent heat treatments of the material. The transition from melt to solid material has a large impact on the material properties by way of changing the microstructure as well as the phase composition.

When the metal is cooled from the molten condition, small particles will be nucleated. Upon further cooling the particles will start to grow until the whole material is solidified. The particles are now called grains, and inside of a grain, the atoms are organized in the same crystal structure with a specific orientation. Both the crystal structure and the orientation may differ from one grain to another, and they are separated by grain boundaries. The speed of the solidification will determine how many particles are nucleated, and how fast they are growing. This will result in metals either consisting of a large single crystal, or consisting of millions of small grains[29].

The properties of these different cases varies greatly. Larger grains result in a more ductile material, while smaller grains will leave the material very brittle. In addition, particles made by segregation of alloying elements from the main phase can form, either inside of larger grains or, more commonly, on the grain boundaries. These will also have a large effect on how the material adapts to different kinds of stress or change of environment. Traditionally, the result of the solidification process has been changed mainly by adjusting the alloy composition or by different heat treatments of the product in the solid state, post solidification. However, already in the 1950's it was discovered that rapid solidification has a dramatic refinement effect on the microstructure, going as far as to remove all grain structure completely, forming metallic glasses[30]. To understand and control the effect of the rapid solidification, it is important to first understand the basic thermodynamics of solidification.

2.3.1 Nucleation and Growth

When discussing the nucleation and growth of new phases, one needs to consider the free energy of the system, ΔG. A chemical change in the system will occur only if the overall free energy of the system is reduced by the change. The free energy is dependent on composition, temperature and pressure. By changing either one or more of these the free energy of another phase may reduce sufficiently for a phase transition to occur.

In addition to looking at the free energy of the volume of each phase before and after the phase transition, one must always consider if there will be an energy barrier for the transition. When a solid phase is nucleated in a melt, a surface needs to be formed. To the surface there is a related surface energy, and so there is an additional energy barrier that must be overcome. There is a critical radius, r^* which is the smallest possible radius for a stable nucleus where the reduction in free energy due to the change of phase is equal to the energy needed to form the surface of the nucleus, see Figure 2.6. The surface energy is dependent on the phases which the new interface lies between. Consequently, some new phases have a lower energy barrier of formation due to a lower surface energy. In addition, the surface energy between two solid phases is generally lower than that which is between a solid and a liquid, so it is common to see the solidification process beginning on some substrate surface[29].

After a stable nucleus is formed, it starts to grow. Also the growth stage is dependent on thermodynamics, as the free energy of the volume and surface tension still needs to be minimized. The surface tension is the most complicated term of the two, as this not only changes between the different phases like the volume free energy, but also is dependent on the crystallographic orientation, hence growth in some directions can be preferential to other.

In addition to the thermodynamic side of the growth, one must also consider the kinetics of the phase transition in terms of the diffusion. The solubility of alloying elements is higher in the liquid phase than in the solid. Some alloying elements can therefore be segregated in front of the solidification front. When the liquid phase becomes enriched in some elements, and depleted of others, new phases might be more stable and be nucleated. Depending on the

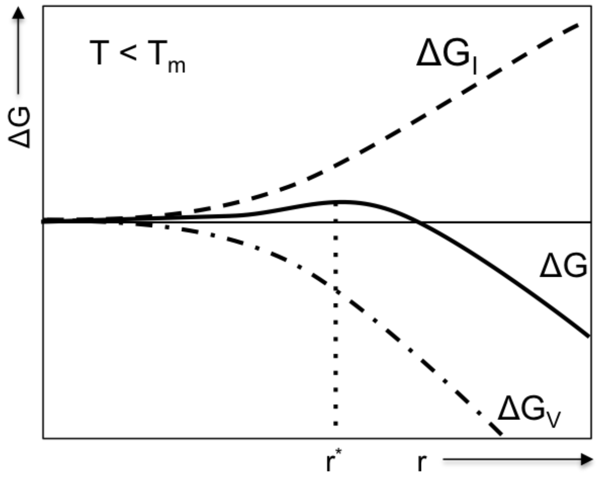

Figure 2.6: The evolution of the free energy of the interface, ΔG_I, the free energy of the volume, ΔG_V, and the free energy of the total system, ΔG. The critical size for a stable nucleus, r* is indicated. Figure adapted from [31].

speed of the solidification, these secondary phases are present either as lamellar structures where there is close to equal amounts of both phases, as smaller grains or particles between the larger grains of the main phase, or as a thin but almost continuous layer on the grain boundaries of the main phase.[29]

2.3.2 Rapid Solidification

Rapid solidification(RS) is a term used for new solidification methods that instead of the cooling rates of traditional casting techniques, which are around $10^{-1} - 10^{-2}$ °C/s, reach rates higher than 10^5 °C/s. This has four main effects on the solidified product[32]:

- Refinement of the microstructure
- Extended solid solubility
- Formation of metastable phases
- Formation of bulk metallic glasses

The large undercooling as a result of the rapid solidification results in a large number of nucleation sites, and a rapid growth. Due to this, the grain structure is refined. However, the diffusion that occurs in front of the solidification front during standard casting is oftentimes too slow too occur when the solidification rate is increased. Consequently, a larger amount of the alloying elements will be in the solid solution of the main phase after RS. Furthermore, the change in composition of the main phase causes strains in the crystal structure, which further causes an increase in the number of defects in the crystals.

In addition to this, the increased undercooling might result in the nucleation of new phases that has a higher energy barrier of formation, and is not the global minimum in free energy. These are called metastable phases. In a traditional casting, this phase would have gone through the phase transition to the stable phase, but due to the rapid solidification rate the metastable phases can still be present in the final product after RS processing.

At very high solidification rates there is no nucleation of crystalline phases. In these cases the atoms will freeze in the same positions as they occupy when they are in the liquid state, in the same way as is observed in glasses. These materials are therefore called bulk metallic glasses. The positioning of the atoms lack the long range order of crystalline phases, although each metal atom will have a coordination number, which is the number of neighbouring atoms. The coordination number is specific to each element, as the net neutrality must be kept and metallic glasses have metallic bonds between the atoms, and so a short range order will be observed[31].

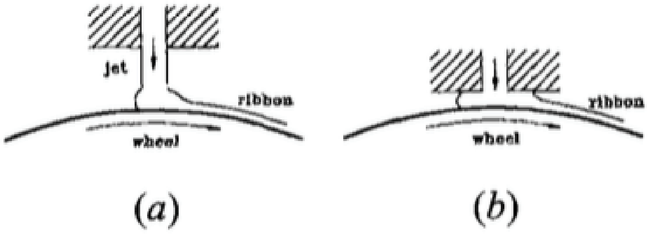

Figure 2.7: Sketches of (a) chill block and (b) planar flow melt spinning [33]

2.3.3 Melt Spinning

One method of rapid solidification is through casting thin ribbons by use of a melt spinner. Melt spinning can be done in several ways. The common factor is that the sample is melted by induction melting. An inert gas is generally used to push the melt out of the crucible and onto a massive, rotating cooling wheel. The cooling wheel effectively extracts the heat from the melt forming thin ribbons. This is the step where the variations occur. There are setups where one can use either one or two cooling wheels. Although two cooling wheels give a higher degree of control of the thickness of the ribbons and a more efficient extraction of heat since there are heat sinks on both sides, it is a more complicated setup, hence one wheel is more commonly used. The one wheel setup is often described as either chill block melt spinner(CBMS) or planar flow melt spinner(PFMS), as shown in Figure 2.7. The main difference is the distance between the wheel and the crucible, G, as planar flow melt pinning is defined as melt spinning where the wheel is at a distance of 1 mm or less above the cooling wheel, while chill block melt spinning has larger distances[33]. The effect of this change is that in CBMS, the melt first forms a steady flow in the air before it impacts on the wheel, while the PFMS instead has the formation of a puddle between the crucible and the wheel. Since the melt is in contact with both the crucible and the wheel, PFMS is a more stable configuration. The resulting ribbons have a more controlled geometry, and the casting is more homogeneous[32].

A schematic of the PFMS puddle region is shown in Figure 2.8. When choosing operability parameters, the main goal is to stabilize the liquid puddle. If the puddle is stable throughout the casting, the ribbons will have close to equal width and thickness, and the probability of producing continuous ribbons increases. The operability window for steady puddle formation was defined by Steen and Karcher[34]. The main limiting parameters are found to be the overpressure from inert gas pressing the melt onto the wheel and the wheel speed, forming a triangular operability window shown in Figure 2.9. If the wheel speed is too high, the melt will be transported away too quickly, and the solidification will occur after the melt has lost contact with the wheel. In this case, there will be little to no formation of flat ribbons. There might be some flakes if the solidification initialize on the wheel, but mostly atomization of spherical shapes will be found.

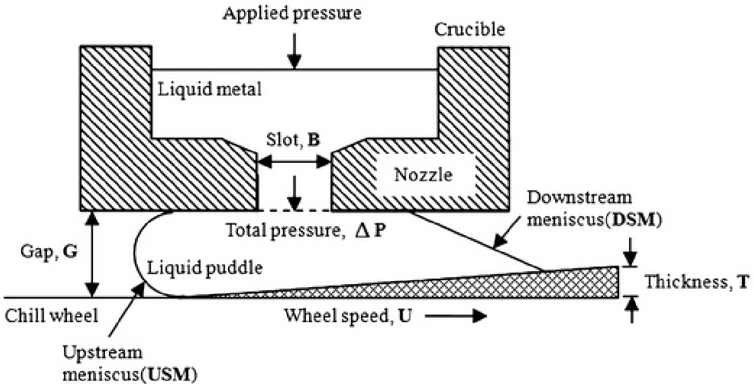

Figure 2.8: A schematic of the puddle region in a planar flow melt spinner[35].

On the other hand, if the speed is slower, but the pressure is too high, the upstream meniscus, as shown in Figure 2.8 will be pushed to the left, and eventually extend outside of the nozzle. Also the downstream meniscus will be pushed out from underneath the nozzle, and the puddle will be flapping, resulting in a non-homogeneous distribution of the ribbon width and thickness.

The last edge of the operability window is when the wheel speed is too high in relation to the pressure, so that the upstream meniscus is moved to the right, extending as far as to end underneath the nozzle gap. The result of this is an increased interaction with the surrounding air, as well as a shredded ribbon. Furthermore, the stability of the puddle varies when changing geometric factors like the nozzle to wheel gap, G, or the slot size, B or when the viscosity of the melt is changed[34].

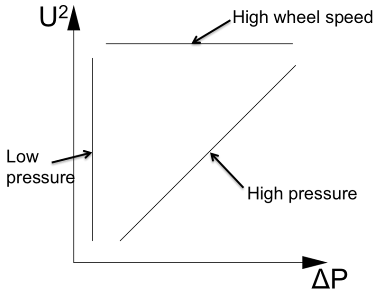

Figure 2.9: The operability diagram for PFMS showing the triangular window for steady casting. Figure adapted from [34]

While the operability window is used to form consistent castings, and by tuning the pressure and wheel speed, the solidification rate will change, Liebermann[32] described the change in solidification rate in the lateral direction of the ribbons. The bottom side, which is the side that is in contact with the cooling wheel, will naturally have a higher solidification rate than the top, as the heat is extracted by the cooling wheel. Consequently, the microstructure is different from the top to the bottom. For a nickel-base superalloy, Liebermann described four characteristic microstructures found at different distances from the cooling wheel, as presented in Figure 2.10. This shows that closest to the substrate, there are equiaxed grains with no specific orientation. Further from the substrate, the grains are more columnar and have a preferred orientation of growth. In the third layer, the columns are broken to a cellular structure, but still with the same orientation, before the last layer has a dendritic growth in the columns. In any melt spun ribbon only one, all four or different combinations of the four may be present, depending on the solidification rate of the sample. If the casting is unstable, different microstructures can be observed in the ribbons.

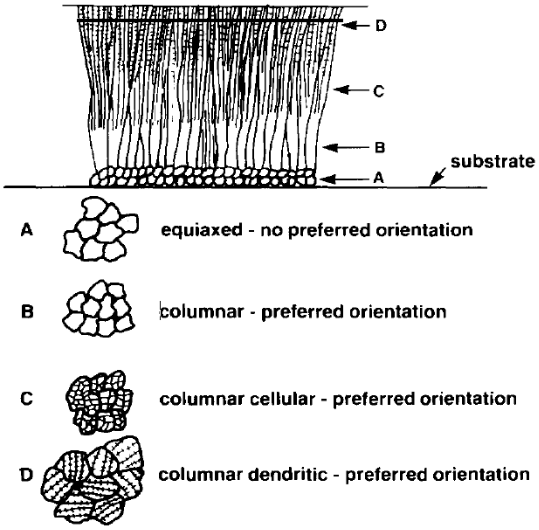

Figure 2.10: Schematic of the microstructures which may be found in the cross-section of a melt spun ribbon. Figure from [32].

2.4 Characterization Techniques

2.4.1 X-Ray Diffraction (XRD)

The X-Ray diffractometer is used to study the crystal structures present in the sample. The working principle is based on Bragg's law of diffraction[29]:

$$n\lambda = 2d_{hkl}sin\theta_{hkl} \tag{2.5}$$

where λ is the wavelength of the X-Ray, d_{hkl} is the distance between the hkl planes, and θ_{hkl} is the incident and reflection angle[36]. Depending on the angle of the impending X-Rays and the distance between the atomic planes from which they are reflected, the reflected beams will have constructive or destructive interference. The result of the XRD analysis will be a spectra with the angles studied on the x-axis and the detected X-Ray intensity on the y-axis. For every peak in the spectra, the added length to the path for an X-Ray satisfies Bragg's law, thus resulting in constructive interference. As both the wavelength and detection angle is known, the distance between the crystallographic planes can be calculated[36], as shown geometrically in Figure 2.11.

The diffraction spectra are characteristic for each crystal structure and elemental composition. For simple systems, the peak positions are known, as also the lattice parameters

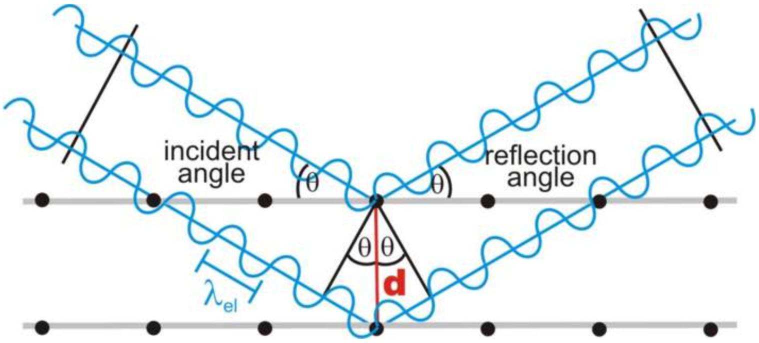

Figure 2.11: An illustration of Bragg's law of diffraction. [37]

and atomic radii are tabulated. The crystal structures present can easily be determined by simply matching the spectra obtained to the standard spectra from a database. If the sample is a mixture of a few simple crystal structures, the standard spectra may be superimposed to determine the structure and composition of the new sample.

If, however, the crystal structure and alloy composition are more complex, there will not be any database entry corresponding to the exact crystal structure and lattice parameters of the sample, and a more thorough analysis is required. One way to do this is by Rietveld refinement[38]. Instead of superimposing peaks at the expected positions and fitting them to the observed curve, the refinement takes all aspects of the powder pattern into account when calculating the expected spectra. This is compared to the experimental result, and the least squares method is used to optimize the parameters of the calculation to find the best fit to the experimental data[39].

The concept of the least squares method can be summarized by the equation:

$$Min \sum_{i=0}^{n-1} (w_i(Y_{obs_i} - Y_{calc_i})^2) \tag{2.6}$$

where Y_{obs_i} is the observed intensity in position i, Y_{calc_i} is the calculated intensity in position i, w_i is the weight that is derived from the variance in Y_{obs}, and $i \in [0, 1, ..., n-1]$ represents angular positions of the measurement, given by:

$$2\theta_i = 2\theta_{start} + i\Delta 2\theta \tag{2.7}$$

Y_{calc_i} is the calculated spectrum. The calculation is defined slightly differently in the literature[38, 39], but the definition given by Mittemeijer et al.[39] is:

$$Y_{calc_i} = \sum_{ph=1}^{phases} (S_{ph} \sum_{hkl_{ph}} (K_{hkl}|F_{hkl}|^2 \phi_{hkl}(2\theta_i - 2\theta_{hkl}))) + b_i \tag{2.8}$$

where ph is the phases present and hkl is the planes in phase ph. The calculated value is based on the different contributions to the spectra from both the sample and the instrument.

There is a certain degree of random scattering from the sample, so a small amount of X-Rays will be detected for all angles θ. This is called the background, and in the refinement this is added to the calculated intensity through the term b_i.

The intensity of the peaks are proportional to the weight fraction of the phase it originates from. The scaling factor S_{ph} is therefore multiplied to all the peaks for each respective phase. To fit the peaks that are positioned for perfect crystals to samples with lattice strain and defects, K_{hkl} is a product of correction factors. $|F_{hkl}|^2$ is the reflection intensity of each peak and lastly $\phi_{hkl}(2\theta_i - 2\theta_{hkl})$ is the profile function of the Bragg reflection relative to the scanner angle.

When doing Rietveld refinement, it is possible to choose which of the terms that should be optimized and which are to be set constant. This helps both in making the computation faster, and giving the operator the ability to assure that all parameters are kept within the reasonable intervals[39].

2.4.2 Scanning Electron Microscopy(SEM)

The scanning electron microscope is used to obtain images of objects that are too small to be seen by the use of light microscopy. As the name implies, the scanning electron microscope has an electron beam that is scanned across the surface of the sample. This results in both elastic and inelastic scattering, generating the numerous signals, as shown in Figure 2.12. The volume from which the signal originates is dependent on the type of radiation. By analyzing the different signals from the elastic and inelastic scattering, information about the chemical composition as well as the topography of the sample can be found[29].

There are two main imaging modes of the SEM, the secondary electron (SE) image and the back scattered electron (BSE) image. Secondary electrons are electrons resulting from the impacting electrons colliding with atoms in the topmost layers of the sample. The energy from the collision releases K-orbital electrons through inelastic scattering. The amount of secondary electrons that are released is almost independent of the type of atom, but if there is any roughness or edges in the sample, the signal will be affected. SE imaging is therefore used to study the topography of the sample[41].

Back scattered electron imaging is, on the other hand, sensitive to elemental composition. The back scattered electrons are electrons that have an elastic interaction with the nucleus of the atoms in the sample. The trajectory of the electrons are bent around the nuclei so that they reemerge from the sample surface. The intensity of the BSE signal is dependent on the strength of the elastic interaction. Heavier atoms have a larger nucleus with a more positive charge, and so the heavier elements give a more intense back scattered signal[41]. If the sample is a multiphase system with a difference in composition between the phases, a

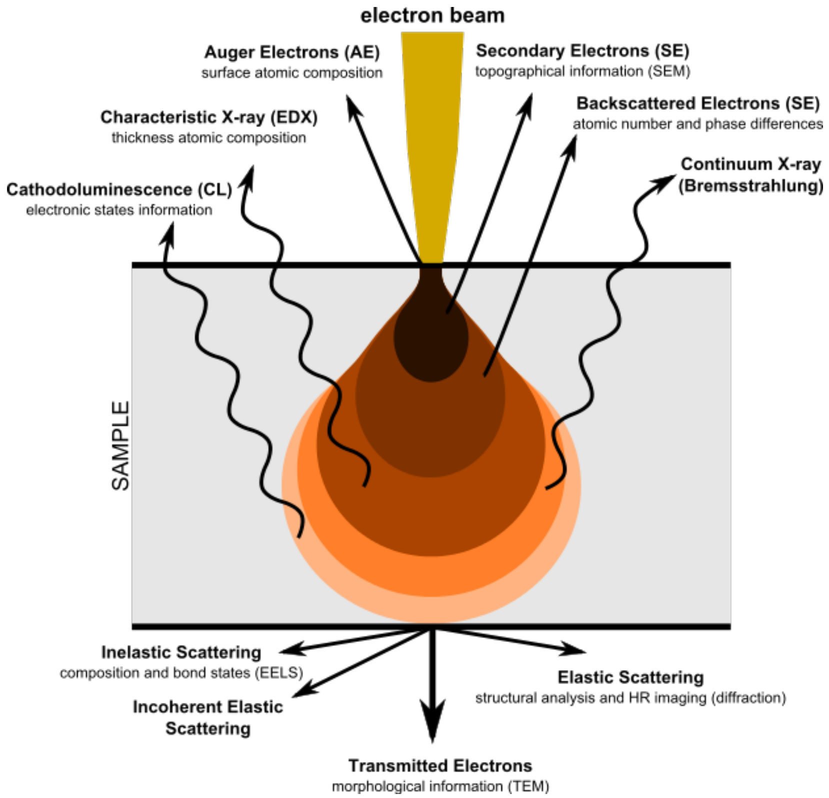

Figure 2.12: An illustration of the interaction volume for different types of radiation as a result of an impending electron beam[40]

contrast will be observed where that the phase with the heaviest elements are the brightest. It is therefore possible to analyze the microstructure of the sample from the BSE image. The back scattered electrons have higher energy than the secondary electrons, and so they can originate from deeper into the sample than the SE[42].

2.4.3 Energy Dispersive Spectroscopy (EDS)

In addition to inelastically and elastically scattered electrons, SEMs are often equipped with X-Ray detectors. As the electron beam impacts on the atoms in the sample, there are occurrences where instead of the inelastic scattering producing a new electron, it will just excite an electron to a higher energy level of the orbitals of the atom. It is not a stable state for an atom to have excited electrons in its electron orbits, and so a relaxation back to the stable state will occur. During the relaxation, an electron goes from a high energy level to a lower one. Consequently energy is released in the form of an X-Ray. The X-Rays that are released due to relaxations are characteristic for the elements. By detecting the X-Rays emitted from the sample, it is possible to estimate the composition of the sample. However, a peak, which ideally has the shape of a narrow line, is broadened in the detection process, and so peak overlaps are almost impossible to avoid[41]. The peak positions of some elements relevant for this thesis are shown in Table B.1.

It is possible to choose the area for EDS analysis by focusing the electron beam onto either one small point to investigate the composition of a specific phase, or one may choose a larger area to get the average composition of the sample. It is, however, important to know that the X-Rays can travel further through the sample than both the BSE and SE. It is therefore possible to see a phase in the BSE imaging mode, but when doing EDS on a point in this phase, the detected signal might have just as large a contribution from another phase lying beneath the surface. One should therefore be very thourough when doing EDS to take several scans and compare to be assured of concluding with the correct composition. In addition, even though the probe of the SEM is small enough to image fine details like particles in the microstructure, the interaction volume of an EDS analysis can exceed five times the probe size, or ca. 1 μm for a beam of 15 keV[41].

2.4.4 Auger Electron Spectroscopy (AES)

To avoid the problem of the large interaction volume of the EDS, one may instead study the elemental composition by Auger Electron Spectroscopy(AES). By using AES, one obtains elemental data from the topmost 2-10 nm of the sample, with a lateral resolution down to 10 nm[43]. This method is therefore a better choice for studying the elemental composition of smaller particles and lamellar features of the microstructure. The principle of AES is similar to EDS in that it is a result of the inelastic scattering of electrons. When an electron is ejected form the K orbital due to a colliding electron from the electron beam, another electron, this time from the L orbital moves to the electron hole i the K orbital. If the energy gap between the L and K orbital is larger than the binding energy of the L orbital electron, another electron will be released[44]. These are called the Auger electrons, and since they are dependent on the electron orbital energy of the atom, they are characteristic to each element. As these electrons stems from the L orbital, they are low energy electrons, hence the shallow interaction volume of the detected Auger electrons, as can also be seen in Figure 2.12.

2.4.5 Pressure-Composition-Temperature(PCT) Diagrams

When studying the interaction between the metal and hydrogen in its gas form, a change in hydrogen absorption with changing pressure and temperature can be observed. It is therefore natural to plot the absorption curve for the metal hydrides in so called pressure-composition-temperature(PCT) diagrams as shown in Figure 2.13. The PCT-diagram has three parts, characterized by the stage in the phase transition between the α- and β-phase of the sample. Initially, the sample is in its pure metal α-phase, and as the pressure of hydrogen increases, atomic H is absorbed into the interstitial sites of the metal crystal lattice. At a critical point, A, the phase transition to the β-phase begins. As more hydrogen is added to the system, the amount of the β-phase is increased. As this is a phase transition, the pressure above the metal is constant, or close to constant, during this transition. At a second critical point, B, the phase transition to the β-phase is complete, and there is no longer any α-phase present in the system. After this point, increased pressure of hydrogen gas above the sample will fill the interstitial sites of the metal hydride with hydrogen, but as the structure is more compact, little excess hydrogen can be absorbed, so the pressure will increase asymptotically[16]. By studying the PCT diagram, the total hydrogen storage capacity of the sample as well as the stability of the hydride phase can be found.

2.4.6 Chronopotentiometry

When comparing different electrode materials, it is elemental to study and quantify the electrochemical interaction of the material in contact with the electrolyte and counter electrode. The common setup is a three electrode system as is shown in Figure 2.14. The electrode being characterized is called the working electrode (WE). The weight and size of the active material in the working electrode must be measured before starting the testing. The counter electrode (CE) is necessary to have a working galvanic cell. It is chosen so that it

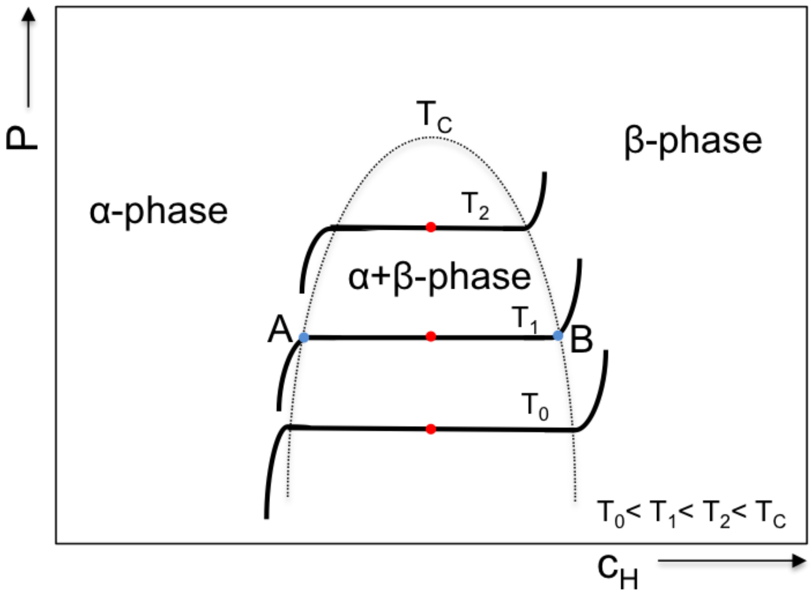

Figure 2.13: PCT diagram with three different isotherms drawn in. The red dots indicate the plateau pressure, P_P, for the respective temperatures. The limits of the phase transition, A and B, are marked for one of the isotherms. Figure adapted from [45]

has higher capacity and faster kinetics than the WE so that it is not the limiting factor of the. Lastly, the reference electrode (REF) is placed close to the WE. It is only connected to the potentiostat and not the main circuit. There is therefore no current flow through the REF, thus no polarization on the REF surface. As potential is a relative measurement, the REF is necessary to be able to compare the measured potentials to other experiments. In the metal hydride field, the Hg/HgO REF is the most common. By placing the REF sufficiently close to the WE, also the ohmic drop of the electrolyte between the REF and the WE can be minimized, thereby only the kinetic polarization of the WE surface and the transport polarization associated with the WE will affect the measured potential drops. The electrochemical setup is in this way optimized to give feedback only on the properties of the WE active material[7].

The battery testing program chosen in this work is chronopotentiometry. In this constant-current method, the resulting potential is measured for different current densities. The electrode reactions will occur at a constant rate corresponding to the applied current, and the potential will change to a value characteristic of the redox pair. When the concentration of one of the reactants becomes too low, the reaction can no longer sustain the current, and the potential drops to the characteristic value of the next electrochemical reaction[46].

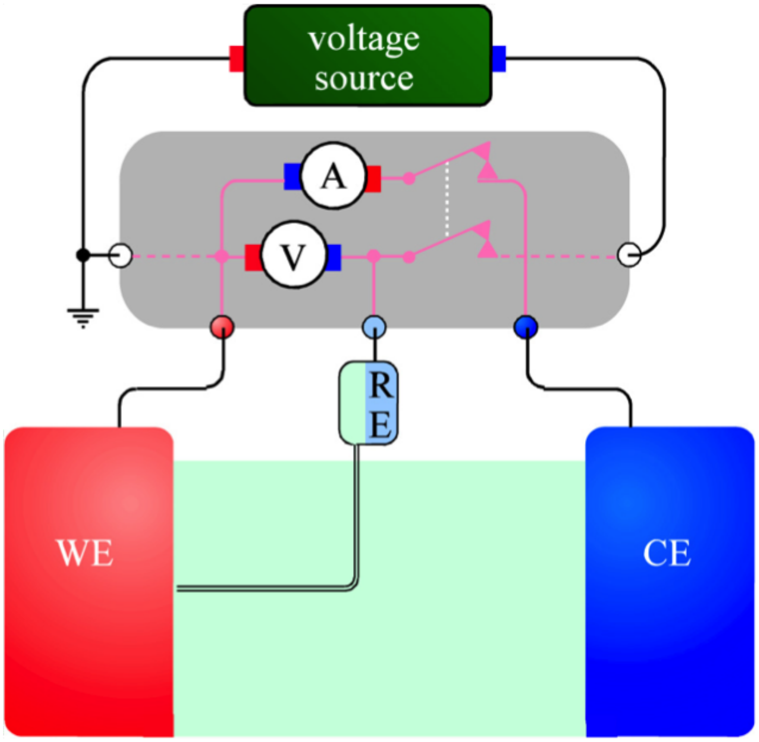

Figure 2.14: The set-up for an electrochemical test, with the working electrode (WE), counter electrode (CE) and the reference electrode (REF). The grey box signifies the potentiostat.[7]

2.4.7 Electrochemical Impedance Spectroscopy (EIS)

Electrochemical impedance spectroscopy is a common analysis technique used to study the electrochemical properties of the different reactions occurring on the electrode. While the cyclic voltammetry uses a constant current and monitors the change in potential, the excitation in impedance spectroscopy is an a.c. perturbation of the current. The frequency of the perturbation is varied over a wide range. The resulting ac potential will have shifts in phase and amplitude at the various frequencies. All the steps in the reaction mechanism has a contribution to the total potential drop of the electrode. Some of these drops can be described as ohmic resistances, as for example the electrolyte resistance, R_E. Others are more complex and frequency dependent. These are called impedances, and is defined as:

$$Z \equiv |E|/|I| \tag{2.9}$$

Both resistance and impedance share the unit Ω [7].

The results of the EIS are commonly presented in Nyquist plots, as shown in Figure 2.15a. As both the input potential and output current signal of the impedance measurement are sinusoidal, and the impedance is defined as the potential over current, the impedance can be described in a complex representation. The negative imaginary part of the total impedance is plotted against the real part for all frequencies recorded in the Nyquist plot. The various reaction steps can be deconvoluted from the result, as long as the time constants does not overlap.

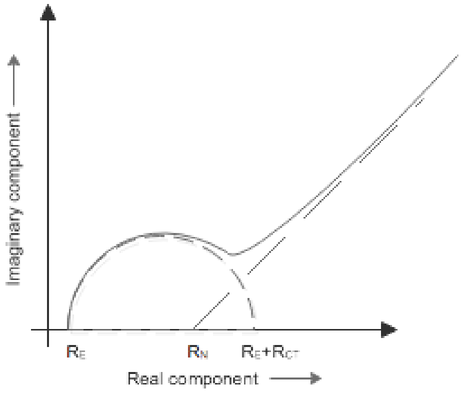

(a) Nyquist plot showing combined effect of charge transfer and diffusion on the impedance results.

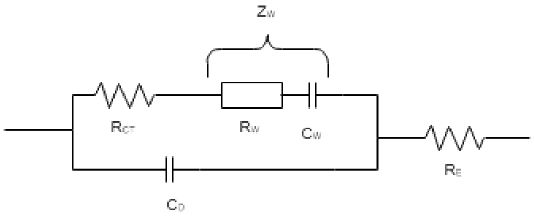

(b) The corresponding equivalent circuit,, where R_{CT} is the charge transfer resistance, $Z_W = R_W + 1/i\omega C_W$ is the Warburg impedance, R_E is the electrolyte resistance and C_D is the double layer capacitance

Figure 2.15: Figures adapted from [47]

To decipher the result of the EIS, it is common to make equivalent circuits of the electrodes. Every element in the circuit represents a step in the reaction mechanism. A typical equivalent circuit for a half-cell is shown in Figure 2.15b, and is called the Randles circuit. The two reaction mechanisms that are taken into account in this circuit is the resistance caused by the charge transfer reaction, R_{CT}, and the diffusion that results in the Warburg impedance, Z_W. In addition, the double layer capacitance, C_D, and the electrolyte resistance, R_E will always contribute to the measured signal. The voltage-current relationship for the different circuit elements are well known. From the equivalent circuit it is therefore possible to form a mathematical expression for the impedance, which can be fitted to the Nyquist plot. Numerical methods can further be used to fit the data and thereby quantify the potential drops and resistances from each step in the reaction mechanism.

For real systems, additional resistances and capacitances to what is shown in Figure 2.15b will also have an impact on the impedance response of the electrode. More complicated equivalent cicuits must therefore be used. As new elements are added, the physical meaning of the new elements must also be determined. For porous metal hydride electrodes, several different equivalents circuits have been proposed, depending on the electrode condition and battery setup [15, 48, 49, 50].

3. Experimental

In this project, two groups of alloys have been studied. Alloy 1 is produced at IFE from pure metals of >99.7% purity that were mixed using an arc melter. The composition of alloy 1 is $(Ti_{0.15}Zr_{0.85}La_{0.03})(Ni_{1.2}Mn_{0.70}V_{0.12}Fe_{0.12})$. However, due to the low vapor pressure of Mn, an excess of Mn needed to be added before the arc melting and melts spinning to compensate to achieve the targeted end composition. Alloy 2 was produced by BASF and has the composition $(Ti_{0.20}Zr_{0.80}La_{0.01})(Ni_{1.2}Mn_{0.70}V_{0.12}Fe_{0.12})$

Each sample was named according to if they were produced at CNRS in Bordeaux (B) or at NTNU (N), which alloy was used (1 or 2), for the amount of excess Mn added and the rotation speed during melt spinning, given in Hz, as explained in Figure 3.1.

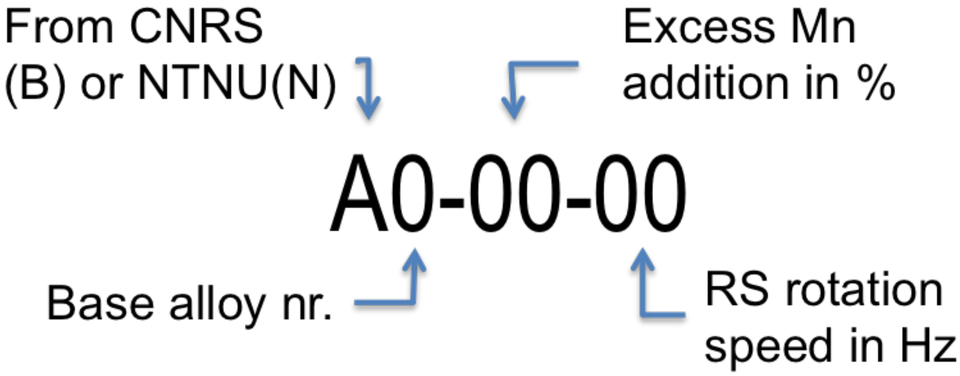

Figure 3.1

3.1 Melt Spinning

Melt spinners of the type Edmund Bühler SC were used for the experiment. A schematic of a melt spinner is presented in Figure 3.2. The copper cooling wheel has a diameter of 20.0 cm, and was polished between each run. For the samples produced at CNRS, the crucible was moved manually. The induction coil was therefore placed sufficiently close to the wheel so that the crucible to wheel distance could be optimized while the crucible was centered inside the induction coil. The system was pumped using a rotary vane pump, and Ar gas was used to purge the chamber as well as for the inert atmosphere during casting. An overview of the casting parameters for the experiments from CNRS is given in table 3.1.

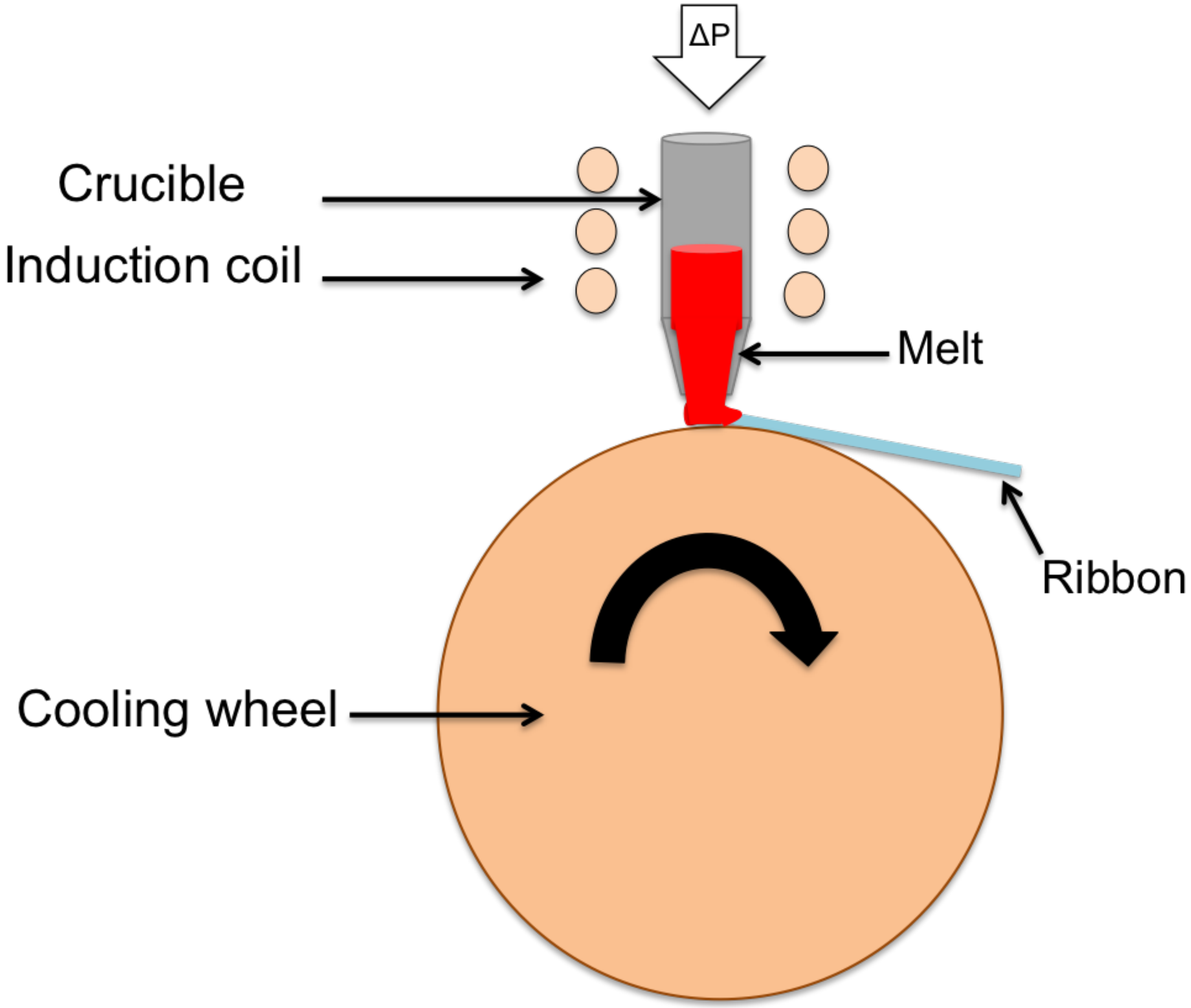

Figure 3.2: A schematic of a melt spinner.

Table 3.1: Specification of the crucible height above the quenching wheel, and number of rotations per second (Hz) for the different alloys produced at CNRS in Bordeaux.

Sample	Casting	Alloy	Crucible height	Speed [Hz]	Speed [m/s]
B2-100	1	2	0.3 mm	100	62.80
B2-33	2	2	1.1 mm	33	20.72
B2-16	3	2	1.1 mm	16.4	10.36
B2-5	4	2	1.0 mm	5	3.14
B1-33	5	1	1.0 mm	33	20.72

At NTNU, the crucible can be automatically adjusted. The induction coil is thus placed higher to avoid heating of the wheel. Before vacuuming the system, the height for heating and for casting is set by adjusting two initiators. During the casting, the crucible could easily be switched between these two by using the automatic controller. Helium was used for the inert gas as the heat conductance of He is better than for Ar, thus resulting in higher solidification speeds. The chamber and gas tanks were evacuated to pre-vacuum and purged with helium using a rotary vane pump, before a turbo pump was used to reach high vacuum at below $5 * 10^{-5}$mBar. A base pressure of 400 mBar He was used during the casting and the wheel to crucible distance was 1.0 mm in the casting position. The alloys, speeds, and overpressure used for each casting are summarized in Table 3.2.

Table 3.2: Specification of the crucible height above the quenching wheel, and number of rotations per second (Hz) for the different alloys produced at NTNU.

Sample	Alloy	Mn addition	Pressure in Tanks/Chamber	Speed [Hz]	Speed [m/s]
N1-25-66	1	25 %	600/400	66	41.44
N1-25-5	1	25 %	600/400	5	3.14
N1-10-33	1	10 %	650/400	33	20.72
N1-10-16	1	10 %	650/400	16.5	10.36
N1-10-5	1	10 %	650/400	5	3.14
N1-5-33	1	5 %	650/400	33	20.72

3.2 Metallographic Analysis

The length, width and thickness of the samples were measured using a caliper. The ribbons and initial alloys were subsequently casted in Epofix epoxy and polished, first with SiC grinding paper of mesh sizes ranging from 800-4000, then with diamond solution of particle size 3 and 1 μm. Aluminum foil and carbon tape was used to ensure electric contact between the sample and the sample holder of the SEM. A LV-FE-SEM of the type Zeiss Supra 55VP with EDS was used to analyse the microstructure and phase composition of the samples. Back scattered electron imaging was used with magnification 5000 and 10000. The images were post-processed by adjusting the grey scale to maximize the contrast in the images.The EDS analysis of each phase in each sample was done by calculating the average of 10 point scans, while the average composition of the samples were found by scanning a larger area of the sample. Furthermore, Auger analysis of one of the samples was performed at CNRS in Bordeaux.

The samples were crushed in a mortar to a fine powder. The powders from the castings in Bordeaux were analyzed by a Bruker D8-Focus X-Ray diffractometer. While for the samples produced at NTNU, the powder sizes smaller than 40 μm were sent to UiO for XRD analysis with a Rigaku multiflex XRD. Furthermore, Rietveld Refinement was performed using the GSAS II software[51].

3.3 Electrochemical Analysis

The powders of particle size 40-60 μm were further processed for electrochemical testing, as illustrated in Figure 3.3. A pellet was formed by pressing the powder mixed with carbonyl nickel (mixing ratio 1:4) in a circular dye at a pressure of 12 MPa for 3-5 minutes. The carbonyl nickel was used to assure good conductivity of throughout the pellet. The real weight of the pellet was measured to be used in later calculations. The pellet was then pressed between two pieces of nickel foam to secure the electrical conductivity in the anode also after the pulverization during the activation stages of the electrode testing. The nickel foam were welded to a strip of nickel to be used as a contact for the anode. The finished anode was subsequently wrapped with a separator sheet, put inside a stainless steel pouch and inserted into the plastic battery container along with the separator and cathode. The container was filled with a 9M KOH electrolyte and the reference electrode (Hg/HgO) was inserted. Finally the electrodes were attached to the Land Battery CT2001A potentiostat and the cell was ready for electrochemical testing. The fully assembled battery can be seen in Figure 3.4.

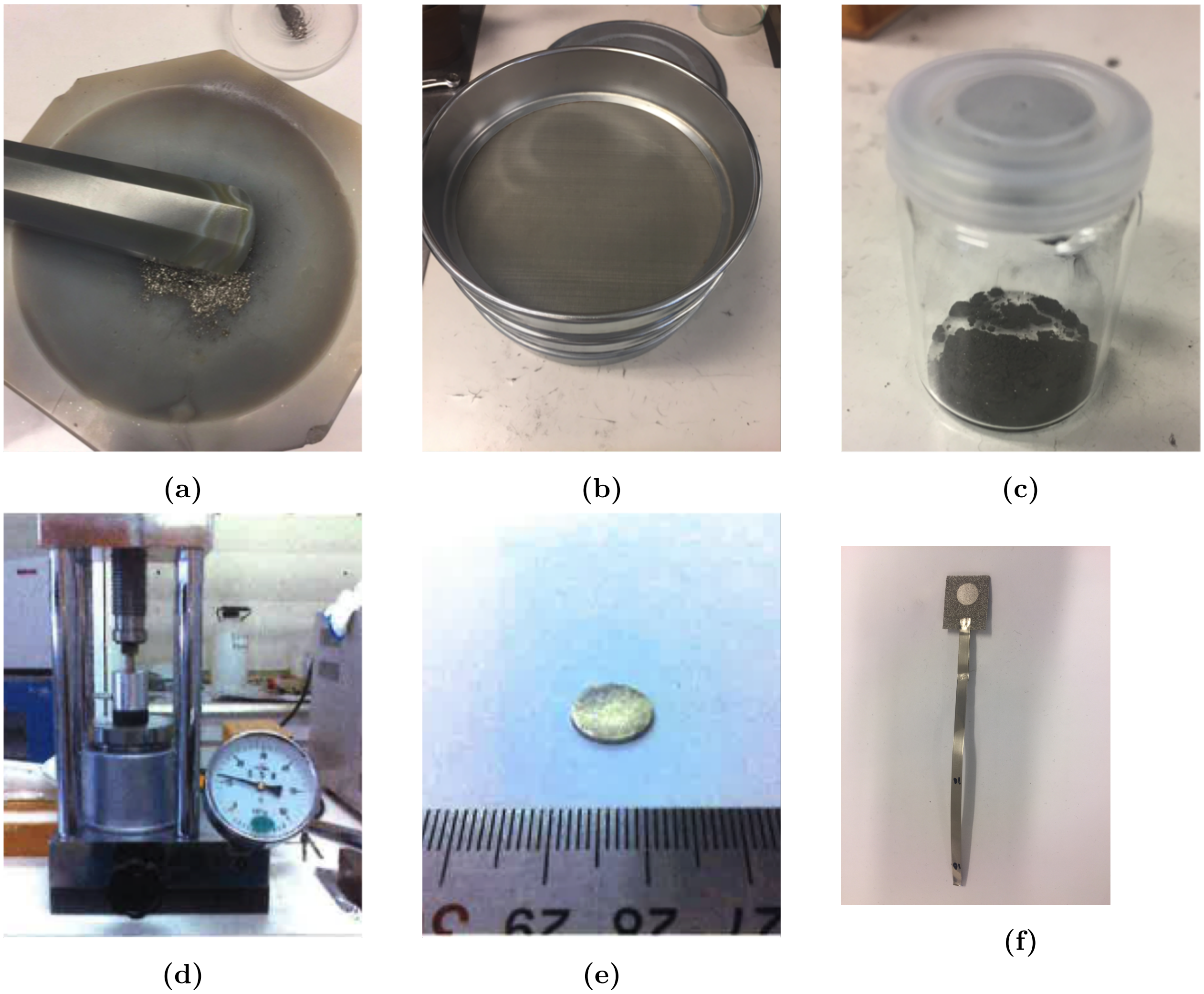

(a) (b) (c) (d) (e) (f)

Figure 3.3: Some of the steps of the making of the electrodes. (a) crushing of the powder in a mortar. (b) The sieve used to select the correct particle size. (c) The mixture of carbonyl nickel and metal powder. (d) The press used to make the pellets. (e) The pellet. (f) The finished electrode.

After assembling the battery, the sample was first given a rest of 1 hour for the KOH electrolyte to soak through the electrode. Three programs for electrochemical testing were used. First, activation was done by cycling the battery with a charging current density of 100 mA/g for 5 hours, a 30 minutes rest, and the discharge down to 0.7 V with a discharge current density of 100 mA/g. The cycles were repeated with a 30 min rest in between. In the initial experiments, only 11 cycles were used, but due to sluggish activation of the melt spun ribbons the number of cycles were increased.

After activation, all electrodes went through the High Rate Discharge ability (HRD) program. Each cycle began with charging with a current density of 100 mA/g for 5 hours. A subsequent rest of 30 minutes was given before the discharge was performed down to the cut-off voltage of 0.6 V. The HRD program for the samples from CNRS was based on C-rates to determine the rate of discharge, while for the samples produced at NTNU the program was split into two separate programs to study the change in capacity in more detail. The current densities used for all three programs are described in Table E.1. After each discharge, a rest of 30 minutes was given before the next charging began.

To test the maximum discharge capacity of the alloys, an additional cycle with the discharge current density of 10 mA/g was tested for the alloys made in Bordeaux.

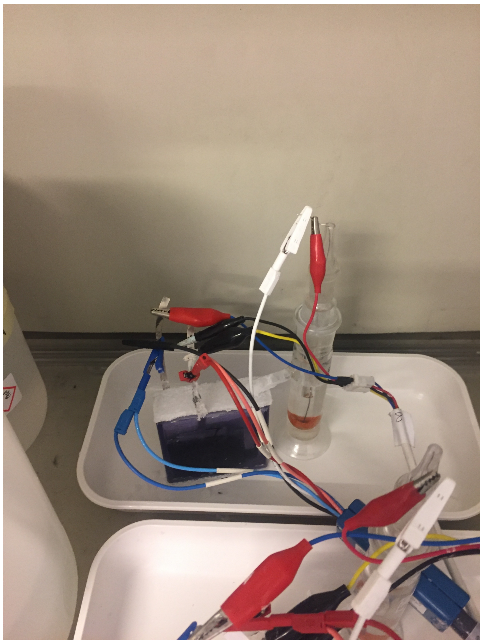

Figure 3.4: The fully assembled battery used for testing the metal hydride electrode

To further study the decrease in discharge capacity by increasing current density, a Low Rate Discharge ability (LRD) program was used for the alloys produced at NTNU. The cycling program was similar to that of HRD, but this time with discharge current densities in the range of 2.4-100 mA/g. Also for the LRD the cut-off voltage was set to 0.6 V.

3.4 Study of Metal-Hydrogen Interaction

Electrochemical impedance spectroscopy was used to study the change in electrochemical performance by varying alloy preparation as well as at different depth of discharge (DOD) of the batteries. A BioLogic SP-300 potentiostat was used for the EIS, and the data were analyzed and fitted using the EC-lab software with Z-fit. The two electrodes with poor HRD performance were chosen for the analysis, as well as the initial alloy as a reference. The EIS was applied at 0, 30, 70, and 100 % DOD. Galvanostatic electrochemical impedance spectroscopy (GEIS) mode was used with the range frequency of measurements from 20 kHz-0.5 mHz and the amplitude of 10 mA for the current.

PCT of one of the samples was performed to study the metal gas interaction of the sample. A Sieverts setup was used, measuring the hydrogen absorption by using the volumetric method of PCT. The powder samples of size < 40 μm were used for the PCT measurements. After the sample was connected to the system, the complete system was evacuated, and subsequently heated under vacuum for 30 minutes at 350°C to desorb any oxygen or other contaminations on the sample surface, before the measurements were commenced.

3.5 Overview of the Characterization

Due to a limited number of cells to perform the electrode testing, the samples with the largest deviations from the targeted compositions were not studied further after solidification. An overview of the characterization steps performed for each samples is given in Table 3.3

Table 3.3: Overview of the characterization method used on the initial alloys as well as all of the melt spun ribbons.

Sample	SEM	EDS	XRD	Activation	HRD1	HRD2	LRD	EIS	PCT	Auger
Alloy 1	X	X		X	X					
Alloy 2	X	X	X	X		X	X			
Alloy 1-5	X		X	X		X	X			
Alloy 1-10	X	X	X	X		X	X	X		
Alloy 1-25	X	X								
B1-33	X	X	X	X	X					
B2-5	X	X	X	X	X					
B2-16	X	X	X	X	X					
B2-33	X	X	X	X	X					
B2-100	X	X	X	X	X					
N1-25-66										
N1-25-5	X	X								
N1-10-5	X	X	X	X		X	X			
N1-10-16	X	X	X	X		X	X	X		
N1-10-33	X	X	X	X		X	X	X	X	X
N1-5-33	X		X	X		X	X			

4. Results

4.1 Melt Spinning at CNRS Bordeaux

From the visit to CNRS, 5 castings were performed. The size of the casted ribbons are presented in Table 4.1. The initial alloys, also discussed as the as cast alloys, for the rapid solidification has additionally been studied for each alloy as references.

Table 4.1: Size of the largest solidified ribbon for each samples produced at CNRS

Sample	Width	Length	Thickness
B2-100	1.5 mm	0.5 cm	43 μm
B2-33	1.9 mm	2.5 cm	57 μm
B2-16	2.0 mm	4.3 cm	125 μm
B2-5	4.0 mm	7.5 cm	213 μm
B1-33	3.5 mm	2.1 cm	64 μm

4.1.1 Alloy 1: $\mathbf{Ti_{0.15}Zr_{0.85}La_{0.03}Ni_{1.2}Mn_{0.70}V_{0.12}Fe_{0.12}}$

Metallographic Analysis

Refinement results for the XRD diffractograms of alloy 1 is shown in Table 4.2. The XRD refinement was performed with a C14 phase with space group $P6_3/mmc$, and a C15 phase with space group $Fd\bar{3}m$. Even though the alloy is hyperstoichiometric with B/A ratio 2.17, the B atom fractions were normalized down to an AB_2 stoichiometry. The refinement initialization parameters are presented in Appendix C. The refinements were successfully performed to weighted residuals of less than 10 %.

The rapidly solidified sample contains a larger amount of the C14 phase, and a small increase of the unit cell is observed both in the C14 and C15 phase.

Figure 4.1 shows the SEM images of alloy 1, both before and after the melt spinning. The reduction in the grain size is evident, as the grain size for the as casted alloy is between 2 and 6 μm while the melt spun alloy contains grains of sizes below 300 nm.

Table 4.2: XRD data for alloy 1

Cell parameter	As cast		B1-33	
	C14	C15	C14	C15
a (å)	4.979±9	7.023±6	4.966±2	7.031±3
c (å)	8.118±2		8.119±7	
Volume (å^3)	173.401±2	346.413±8	174.25±1	347.565±4
Abundance (wt%)	5.4896 %	94.510 %	36.223 %	63.777 %

The EDS results of alloy 1 are summarized in Table 4.3. It appears that the main change in composition from the as casted to the rapidly solidified sample is a loss of Ni and Ti, as an effect of the levitation melting and subsequent melt spinning.

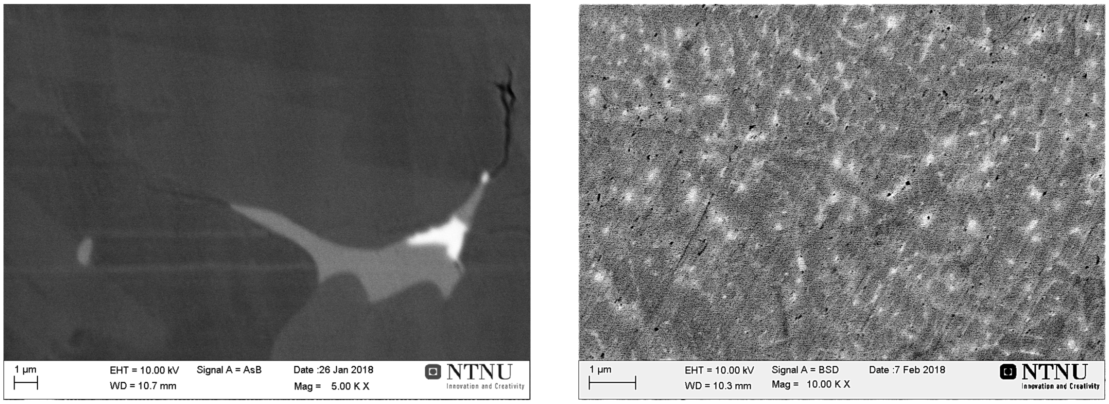

(a) **(b)**

Figure 4.1: SEM images of alloy 1 as casted with magnification 5000(a) and melt spun with rotation speed 33 Hz with magnification 10 000(b)

Electrochemical Analysis

The effect of the rapid solidification on the electrochemical performance of alloy 1 is shown by the voltage profiles in Figure 4.2a and b. The activation of the melt spun alloy requires more cycles compared to the as casted sample. The initial alloy reaches stable performance after only 4 cycles, while the melt spun alloy does not show a stable discharge capacity until at least 11 cycles have been performed. On the other hand, the final discharge capacity of the melt spun ribbon after the activation has been completed is higher than the as casted alloy by 20 mAhg^{-1}.

The high rate discharge performance of the two samples is compared in Figure 4.2c-

Table 4.3: EDS results for alloy 1, given by the average at% of 10 point scans with the standard deviation (SD). As the grains of B1-33 are too small for phase analysis by EDS, only the average composition is given.

	As cast				B1-33	
	Particles		Matrix		Average	
	Mean	SD	Mean	SD	Mean	SD
Fe	0.47	0.05	2.24	0.43	4.89	0.26
Ni	54.70	0.38	38.84	2.50	29.33	0.55
Zr	30.34	0.44	23.40	0.29	27.45	0.43
Ti	9.86	0.36	4.56	0.77	5.08	0.16
La	0.94	0.22	0.50	0.17	1.68	0.20
V	0.29	0.14	3.62	0.73	4.03	0.18
Mn	3.96	0.19	26.85	2.29	27.55	0.62

f. The melt spun alloy shows a higher discharge capacity for all current densities, with a maximum current density of 397 mAhg^{-1} achieved at an applied current density of 10 mAg^{-1}. Both samples show a significant decrease in discharge capacity when the current density is increased from 10 to 25 mAg^{-1}, and before the discharge capacity decrease more steadily with further increase in the applied current density.

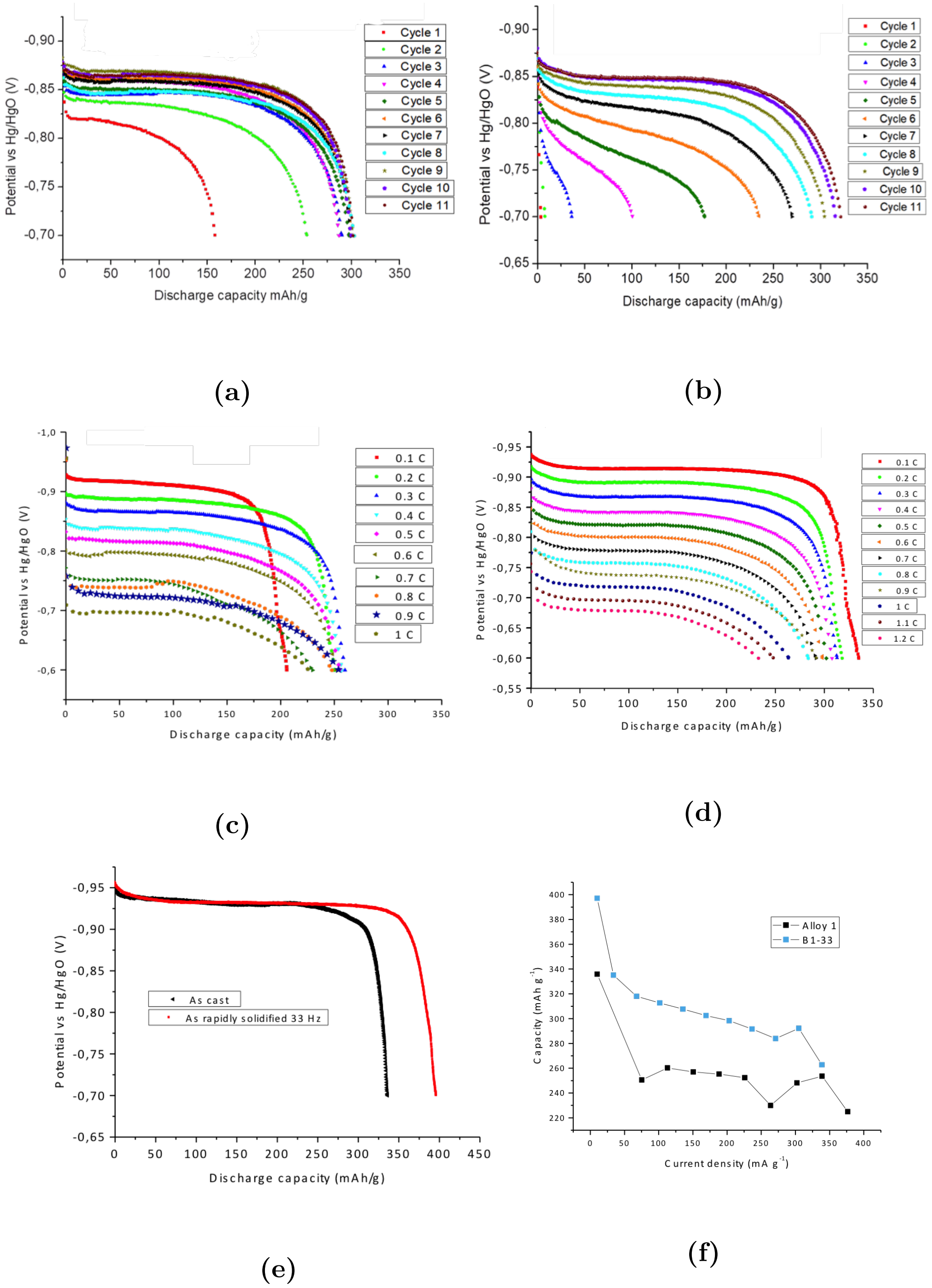

(a)

(b)

(c)

(d)

(e)

(f)

Figure 4.2: Voltage profiles of as casted (a) and melt spun alloy 1 with rotation speed 33 Hz (b) during the activation. High rate dischargeability results of as casted (c) and melt spun alloy 1 with rotation speed 33 Hz (d). The voltage profile for both samples at 10 mAg^{-1} current density are shown in (e). A comparison of the discharge capacity as related to the applied current density for the two samples is shown in (f)

4.1.2 Alloy 2: $Ti_{0.2}Zr_{0.8}La_{0.01}Ni_{1.2}Mn_{0.70}V_{0.12}Fe_{0.12}$

Metallographic Analysis

For the alloy 2, which has an increased ratio of Ti:Zr and a reduced amount of La, four different rapid solidification speeds were studied. The results of the phase fraction of C15 determined by XRD and the grain size determined from the SEM imaging are summarized in Table 4.4.

Table 4.4

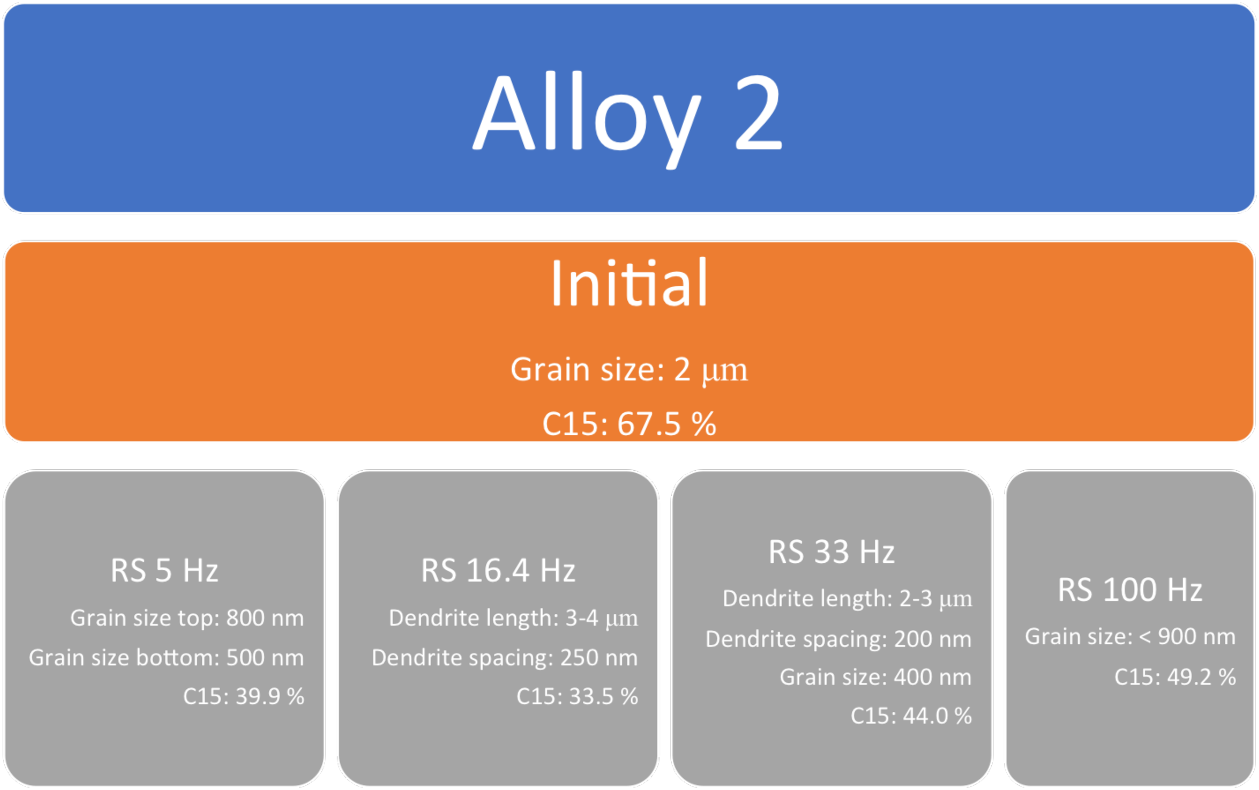

Alloy 2

Initial
Grain size: 2 µm
C15: 67.5 %

RS 5 Hz
Grain size top: 800 nm
Grain size bottom: 500 nm
C15: 39.9 %

RS 16.4 Hz
Dendrite length: 3-4 µm
Dendrite spacing: 250 nm
C15: 33.5 %

RS 33 Hz
Dendrite length: 2-3 µm
Dendrite spacing: 200 nm
Grain size: 400 nm
C15: 44.0 %

RS 100 Hz
Grain size: < 900 nm
C15: 49.2 %

The effect or rapid solidification on the crystal structures and phase compositions of alloy 2 as studied by XRD can be seen in Figure 4.3 and Table 4.5. The amount of the C14 crystal structure increase from as casted to the rapidly solidified samples, but decrease with respect to the rapid solidification speed. The maximum amount of C14 is found for the sample with 16.4 Hz rotation frequency. The unit cell of the C14 crystal structure increases with increasing cooling rate, while C15 has a unit cell contraction from the as casted to the melt spun sample of 5 Hz rotation frequency, before it increases with further increase in solidification rate.

For alloy 2, the different rotation speeds during the rapid solidification resulted in a large change in the morphology of the casted ribbons. Also here the as casted sample has grains

Table 4.5: XRD data for the alloy 2

Cell parameter	As cast		B2-5		B2-16	
	C14	C15	C14	C15	C14	C15
a (å)	4.940±4	7.006±6	4.946±4	6.997±6	4.959±4	7.008±9
c (å)	8.037±2		8.056±4		8.079±1	
Volume (å^3)	169.874±2	343.852±8	170.684±4	342.617±8	172.101±4	344.226±1
Abundance (wt%)	32.50 %	67.50 %	60.141 %	39.859 %	66.488 %	33.512 %

Cell parameter	B2-33		B2-100		
	C14	C15	C14	C15	
a (å)	4.957±7	7.009±9	4.964±7	7.026±1	
c (å)	8.074±2		8.087±6		
Volume (å^3)	171.811±5	344.371±1	172.552±5	346.853±3	
Abundance (wt%)	55.953 %	44.047 %	50.845 %	49.155 %	

of size range above 2 μm, as shown in Figure 4.5a, while all melt spun ribbons have grains of submicron sizes. With the rotation speed of 5 Hz, the ribbons were studied from both sides, an it is shown in Figure 4.5b that the top side has grains of equal size in all direction with average size around 800 nm. The bottom side, which was in contact with the cooling wheel during the solidification, is shown in Figure 4.5c, and particles are here observed in addition to some secondary phases at the intercepts between multiple grains of the matrix phase. There are continuous areas of the matrix phase with diameters up to 2 μm, however it is not possible from the BSE image to conclude if this is a single grain or several smaller ones due to the low contrast between grains of the same phase. The grains of the secondary phase does, however, show grain size of 500 nm for the bottom of this sample, while the particles are under 0.1 μm. There also appears to be a phase of similar contrast to the particles that lie on some of the grain boundaries, especially between the matrix phase and the secondary phase.

Increasing the rotation frequency of the rapid solidification changes the microstructure to a lamellar structure. This is clear for both the samples solidified at 16.5 Hz and at 33 Hz rotation frequency. The former has slightly coarser dendrites of width 250 nm, and the primary dendrite length is 3-4 μm. The sample B2-33 consists of a mixed morphology as shown in Figure 4.5e, part of the samples have a lamellar morphology with primary dendrite length varying from 2-3 μm and dendrite width of 200 nm. Other areas consist of grains of average size around 400 nm and particles of size 200 nm and smaller.

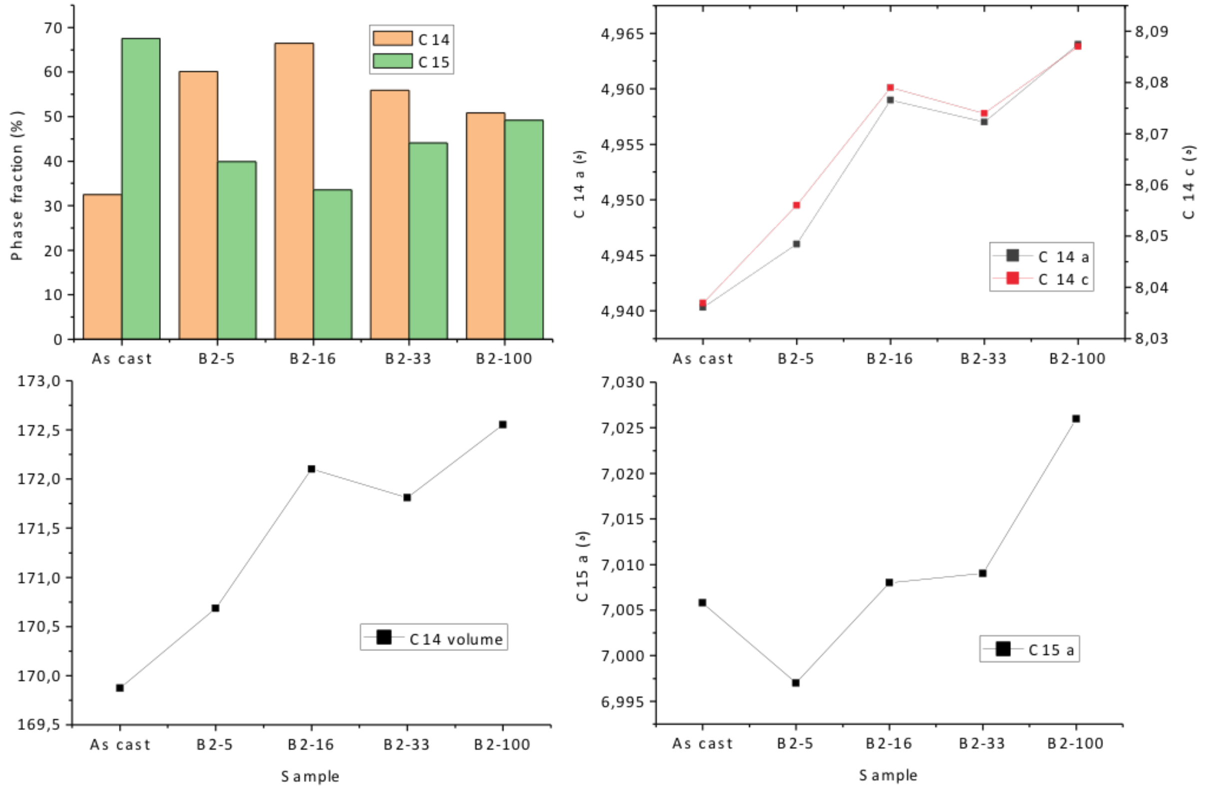

Figure 4.3: The XRD refinement results of the phase fraction, unit cell parameters and unit cell volume of the C14 and C15 phase for alloy 2.

Finally, with rotation frequency of 100 Hz, the morphology is more constant, with a matrix phase and a secondary phase that forms a continuous layer on the grain boundaries. The areas of the main phase have a size of approximately 900 nm, however this is again most likely consisting of multiple grains.

Figure 4.4 shows the EDS results for alloy 2 both for the main and secondary phase, and the tabulated EDS results can be seen in Table D.1. The compositions change slightly from the as cast to the RS-samples, but there is no large variation with change in RS cooling rate. The main change is the loss of Mn as well as Zr and La. However, as all of the RS samples have microstructural features of submicron size, the results are not valid for quantification of the secondary phase composition.

Electrochemical Analysis

The activation performance for alloy 2 is shown in Figure 4.6. There is no flat plateau region during the activation of these alloys. The activation is sluggish, also for the as casted samples.

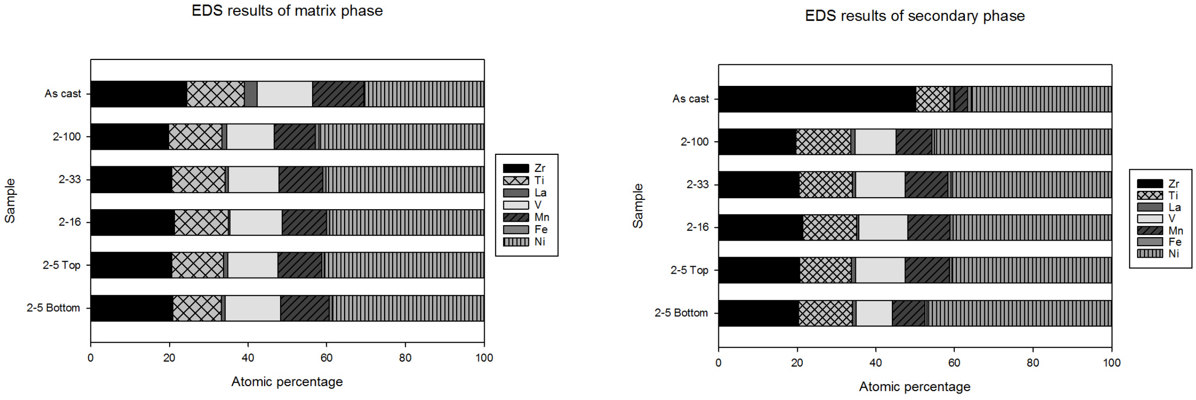

(a) **(b)**

Figure 4.4: EDS results for the matrix phase (a) and the secondary phase (b) for all ribbons and the as cast sample of alloy 2.

The best activation performance is found for the sample B2-16, which reaches full capacity after 8 cycles. The discharge capacity for the as casted sample after 11 cycles is 270 mAhg^{-1}, while the maximum discharge capacity after the activation for a melt spun alloy is found for the sample with rotation frequency 16.4 Hz, with 180 mAhg^{-1}.

The discharge capacity increases when the current density is lowered. As shown in Figure 4.7a, all melt spun alloys have a discharge capacity around 400 mAhg^{-1} for current density 10 mAg^{-1}, with the highest current density again for the sample with rotation frequency 16.4 Hz. The comparison of discharge capacity as related to the applied current density for all samples of alloy 2 is shown in Figure 4.7b. This shows that also this alloy has a significant decrease in current density from 10-50 mAg^{-1} current density, before a more steady decrease is observed. The slope of the curve is smallest for the sample with rotation speed 100 Hz, resulting in a higher discharge capacity at high current densities.

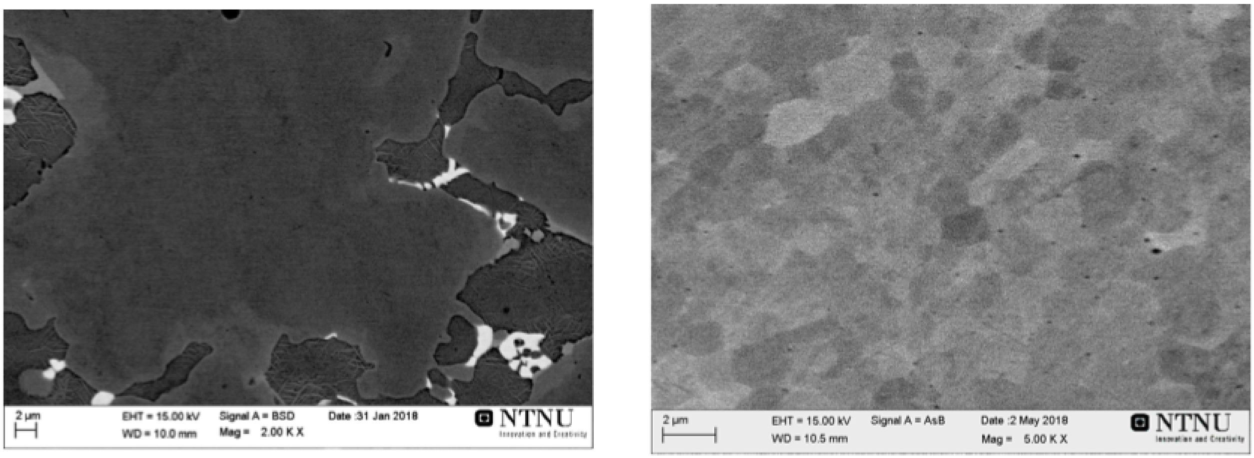

(a) As cast

(b) B2-5 top

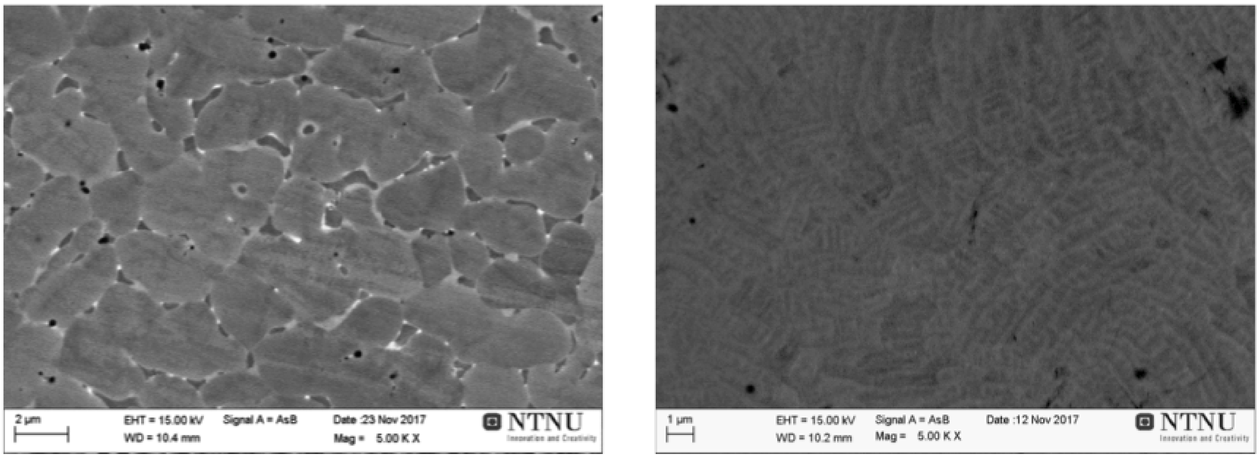

(c) B2-5 bottom

(d) B2-16

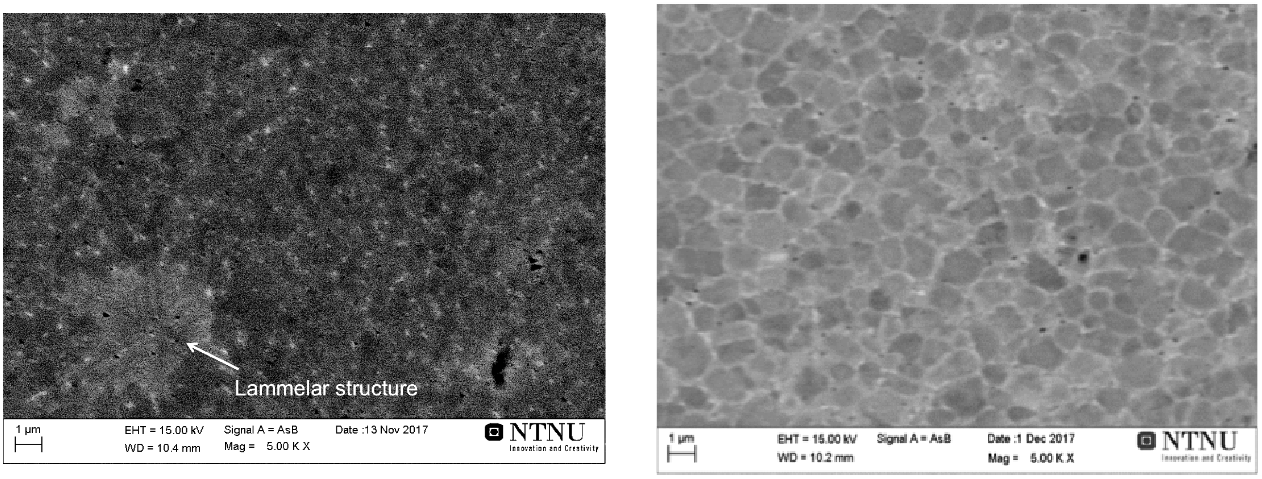

(e) B2-33

(f) B2-100

Figure 4.5: SEM images of casted samples of alloy 2, (a) base alloy with magnification 2000x, and with RS rotation speed (b) and (c) 5 Hz, (d) 16.4 Hz, (e) 33 Hz and (f)100 Hz. All images are in back scattered electron mode and magnification for RS alloys are 5000x.

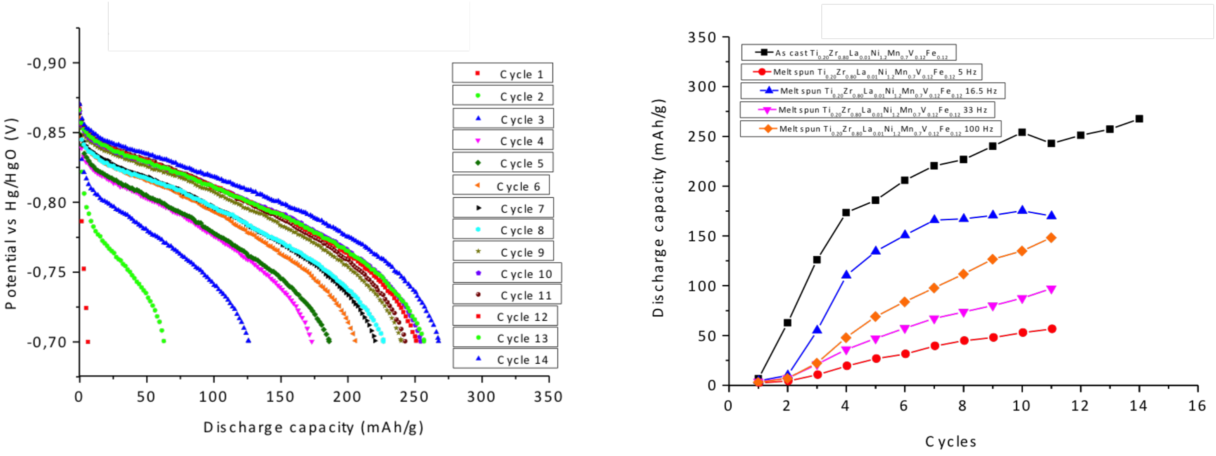

(a)

(b)

Figure 4.6: The voltage profile of alloy 2 as casted during the activation (a) and a comparison of the discharge capacity with respect to the cycle number for all tested samples of alloy 2 during the activation(b). All activation voltage profiles can be seen in Figure F.1

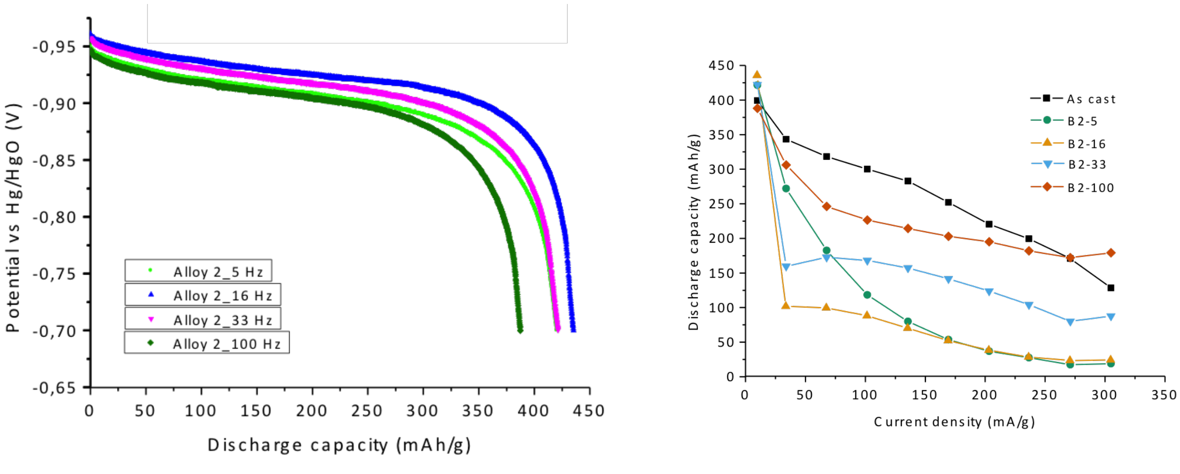

(a)

(b)

Figure 4.7: (a)The voltage profiles for all samples of alloy 2, with an applied current density of 10mAg^{-1} and (b) a comparison of the discharge capacity as related to the applied current density for all samples of alloy 2. The voltage profiles of all of the cycles are presented in Figure F.3.

4.2 Melt Spinning at NTNU

The resulting size of the ribbons casted at NTNU are presented in Table 4.6. As expected the ribbon thickness decreases with increasing solidification speed. It is however similar for the different alloy compositions casted with equal speed.

Table 4.6: Specification of length, width and thickness of the samples prepared at NTNU.

Sample	Alloy	Mn addition	Speed [Hz]	Length	Width [mm]	Thickness [mm]
N1-25-66	1	25 %	66	<4 mm	0.35	0.012
N1-25-5	1	25 %	5	2-3 cm	1.95-2.32	0.19
N1-10-33	1	10 %	33	0.5-1.5 cm	2.90-3.53	0.04
N1-10-16	1	10 %	16.5	10-15 cm	2.48-2.72	0.08
N1-10-5	1	10 %	5	14-21 cm	0.31-1.35	0.22-0.06
N1-5-33	1	5 %	33	<1 cm	2.03-4.54	0.03

The results of the phase fraction of C15 determined by XRD and the grain size determined from the SEM for all samples of alloy 1 are summarized in Table 4.7.

Table 4.7

Alloy 1

Initial
Grain size: 4 µm
C15: 94.5 %

5 % Mn Addition
C15: 94.5 %

10 % Mn Addition
Grain size: 3.5 µm
C15: 94.8 %

RS 33 Hz
Grain size: 300 nm
C15: 95.9%

RS 33 Hz
Grain size top: 500 nm
Grain size bottom: 300 nm
C15: 99.3 %

RS 5 Hz
Grain size top: 750 nm
Grain size bottom: 500 nm
C15: 70.9 %

RS 16.5 Hz
Grain size top: 300 nm
Grain size bottom: 500 nm
C15: 85.3 %

RS 33 Hz
Grain size: 250 nm
C15: 90.4 %

4.2.1 Alloy 1-25: $\mathbf{Ti_{0.15}Zr_{0.85}La_{0.03}Ni_{1.2}Mn_{0.70}V_{0.12}Fe_{0.12}}$ with 25 % excess Mn

Metallographic Analysis

The SEM images of alloy 1 with 25 % added Mn both in the as casted and melt spun state with rotation frequency 5 Hz both from the top and bottom side. The sample casted at 66 Hz rotation frequency is too fine to be polished and further obtaining microstructure images. Also for this alloy the as casted sample has a grain size of about 2 μm. The melt spun alloy has a grain size of around 0.25 μm on the bottom side that increases to 0.5 μm on the top. As the solidification rate decreases between the three images, the particles also increase in size, and are more spread out. The EDS results in Table D.2 and D.3 show that the alloy also after RS has a composition of more than 40 wt% Mn which is significantly larger than the targeted content. Both samples casted with 25 % excess of Mn has therefore not been further analyzed.

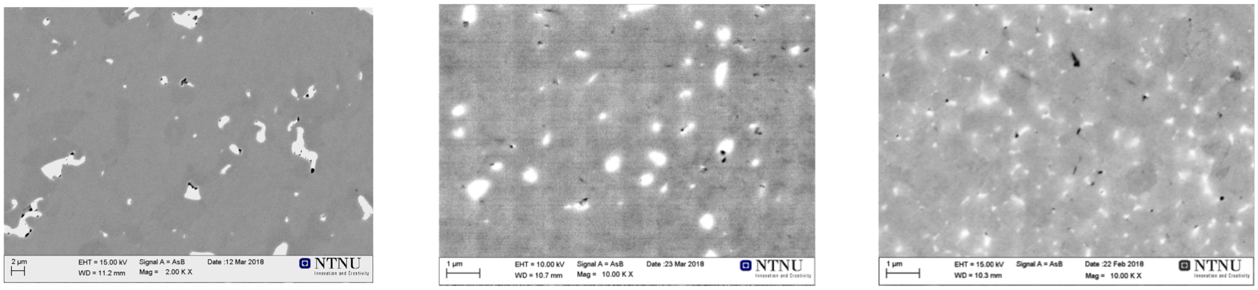

(a) **(b)** **(c)**

Figure 4.8: SEM images of alloy 1 with 25 % added Mn (a) as casted and (b) the top and (c) the bottom of the alloy melt spun with rotation frequency 5 Hz.

4.2.2 Alloy 1-10: $\mathbf{Ti_{0.15}Zr_{0.85}La_{0.03}Ni_{1.2}Mn_{0.70}V_{0.12}Fe_{0.12}}$ with 10 % excess Mn

Metallographic Analysis

For the alloy 1 with 10 % added Mn, the SEM images are presented in Figure 4.9. The as cast sample show a similar microstructure to the other initial alloys with a grain size of approximately 3.5 μm. Rapid solidification has refined the microstructure, but for this composition, little to no dendrite structure is observed. For the alloy with RS speed 33 Hz, a fine grained structure of diameter approximately 250 nm is shown. The phase contrast is very small, indicating that any particles present are too small to be observed by SEM.

Reducing the speed to 16.5 Hz increases the grain size slightly, but the main difference is the observation of smaller particles. The particles, as well as the grains, appear to increase in size from the bottom to the top of the ribbon with a grain size 300 nm at the bottom and 500 nm at the top.

With a further decrease in RS speed to 5 Hz, the grain size increases to approximately 500 nm on the bottom and 750 nm on the top of the ribbons. Also here there are particles present at the junctions between the matrix phase grains. The SEM images from a cross section of these images, presented in Figure 4.10, confirm that there is a small increase in grain size from the bottom to the top, and that the number of particles increases closer to the bottom, but the size of the particles simultaneously decreases. Furthermore, there is a clear contrast between the grains of the main phase at the bottom, which disappear at the top.

A selection of the EDS data are shown in Figure 4.11, and the full set of data is presented in Table D.2 and D.3. The change in composition from the matrix phase to the particles show that La is segregated to the particles, while Mn and V is present mainly in the matrix phase. In the as casted samples it is clear that there is less Ti and Zr in the particles than the main phase, while the amount of Fe and Ni is fairly evenly distributed in both phases.

From the EDS data the B/A ratio and average electron density *e/a* was calculated, as seen in Figure 4.12. It is clear that the main phase has higher B/A ratio as well as *e/a* compared to the secondary phase. In the matrix phase, the lowest B/A ratio can be found for sample N1-10-5, while the *e/a* continuously increase with rapid solidification speed.

Furthermore, Auger analysis was performed on sample N1-10-33, to obtain the exact quantification of the matrix and particle elemental composition. The results are shown in Table 4.8. It is further proof that the particles contain almost 50 wt% La, while there is only about 0.5 wt% in the matrix phase. In addition, the O content is increased in the particles.

A mapping of the elemental distribution, shown in Figure 4.13, shows that the La-rich particles are depleted in the two other A-elements, Ti and Zr.

Table 4.8: The Auger analysis results for the sample N1-10-33

Phase	O	Ti	V	Mn	Fe	Ni	Zr	La
Matrix	4.59	4.02	3.84	22.33	0.47	37.37	26.87	0.31
Matrix	4.51	4.56	4.05	26.51	0.19	33.91	25.85	0.42
Matrix	3.36	6.67	2.70	25.28	0.33	34.66	26.33	0.66
Particle	11.10	1.84	1.72	13.03	0.07	15.80	9.27	47.17
Particle	16.62	0.19	0.68	8.32	0.06	15.42	9.41	49.30

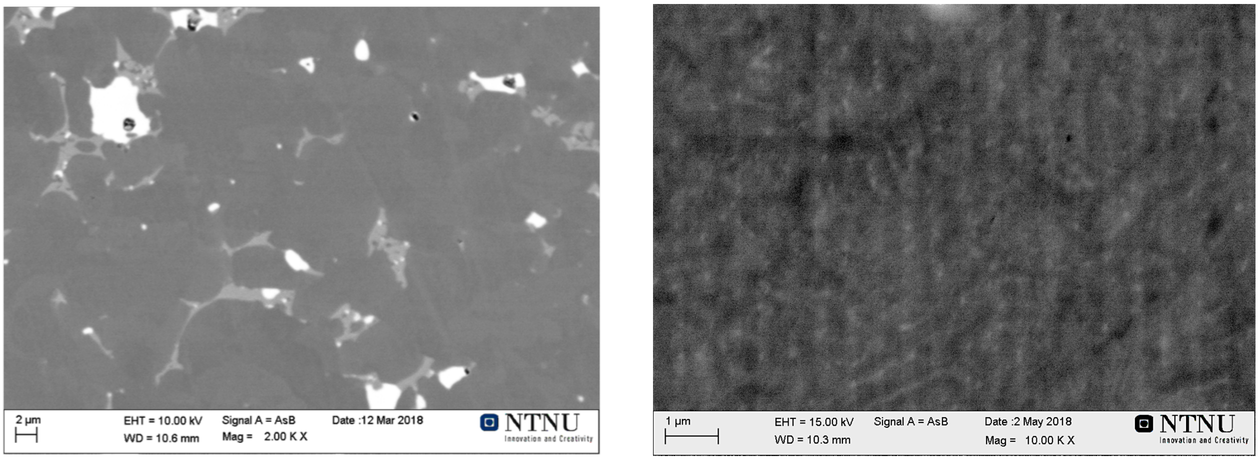

(a) As cast

(b) N1-10-33

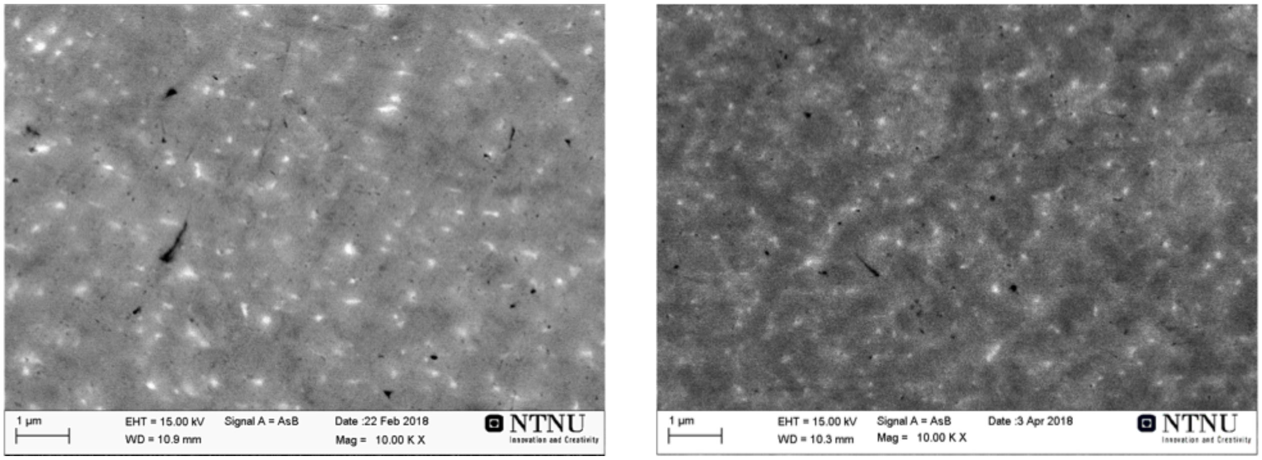

(c) N1-10-16 top

(d) N1-10-16 Bottom

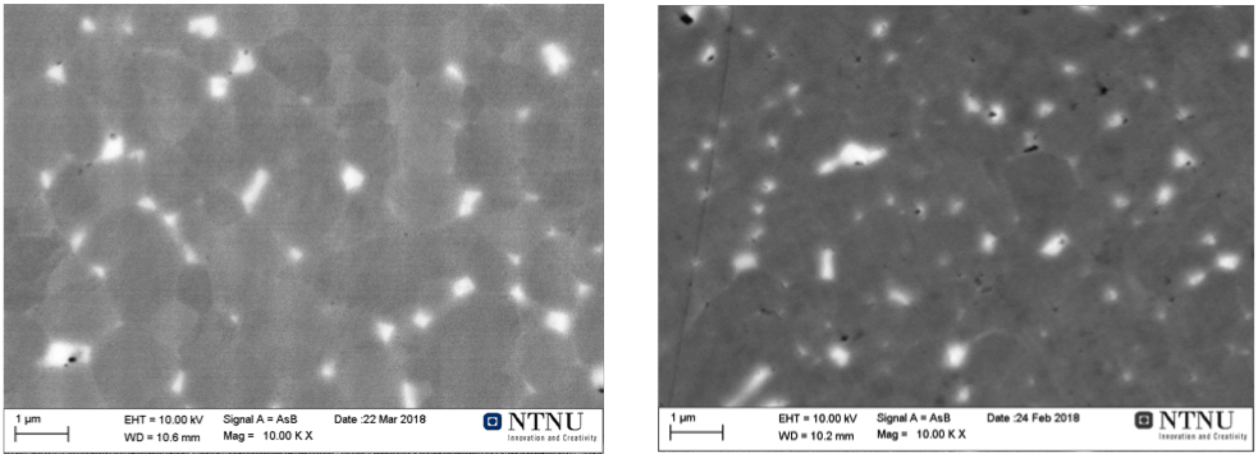

(e) N1-10-5 top

(f) N1-10-5 bottom

Figure 4.9: SEM images of casted samples of alloy 1 with 10 % added Mn, (a) initial alloy with magnification 2000x, and melt spun alloy with rotation speed (b) 33 Hz, (c) and (d) 16.5 Hz, and (e) and (f) 5 Hz. All images are in back scattered electron mode and magnification for RS alloys is 10 000x.

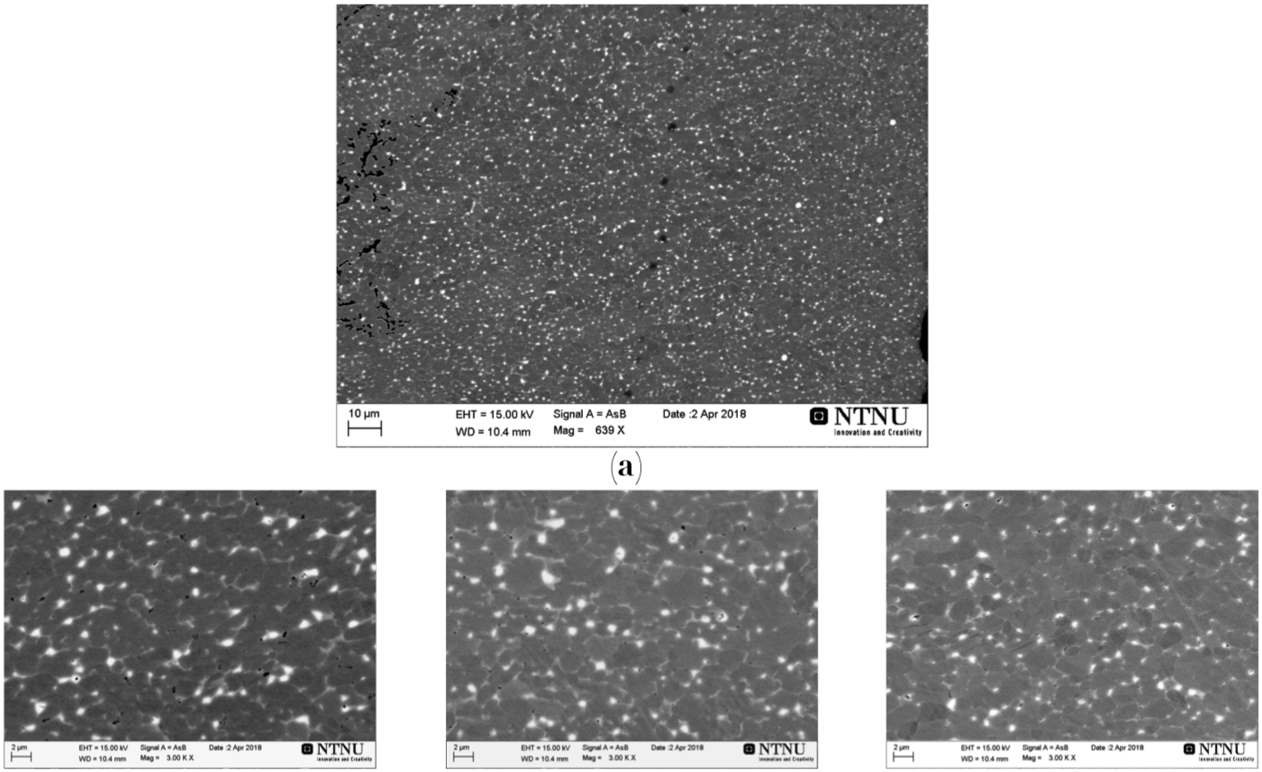

(a)

(b) (c) (d)

Figure 4.10: The cross sectional image of the sample N1-10-5 (a) where the bottom of the ribbon is on the right hand side, and the top of the ribbon is on the left hand side. Images at 3000x magnification is shown underneath of the top (b), the center (c) and the bottom (d).

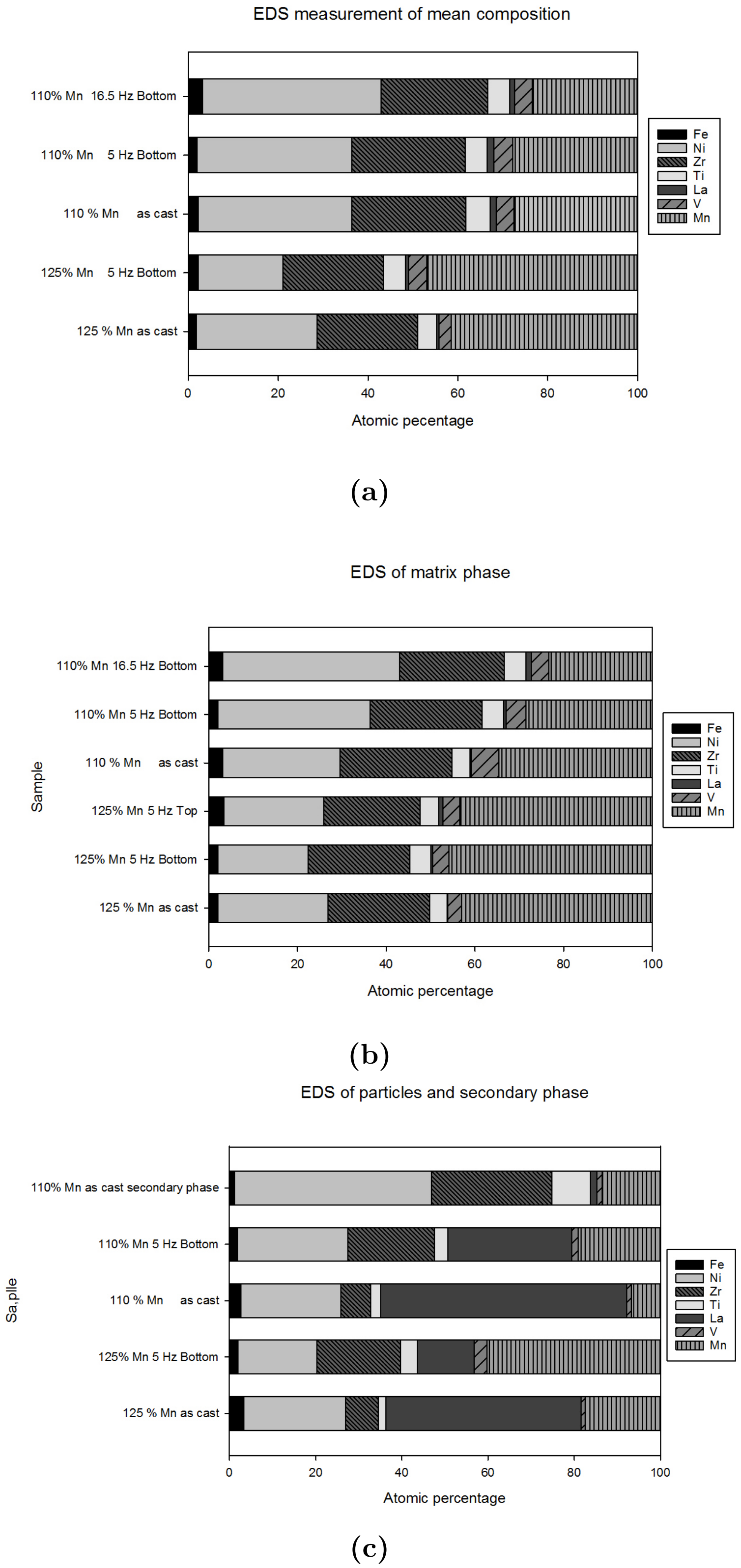

Figure 4.11: EDS results for the as casted and some of the ribbons of alloy 1 with both 10 and 25 % added Mn.

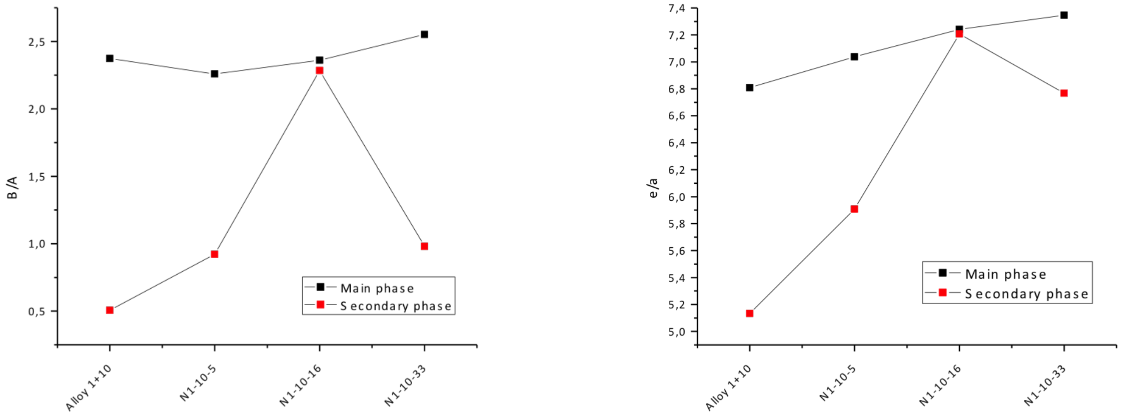

(a) **(b)**

Figure 4.12: The B/A ratio (a) and *e/a* (b) calculated from the EDS results for the alloy 1 with 10 % added Mn.

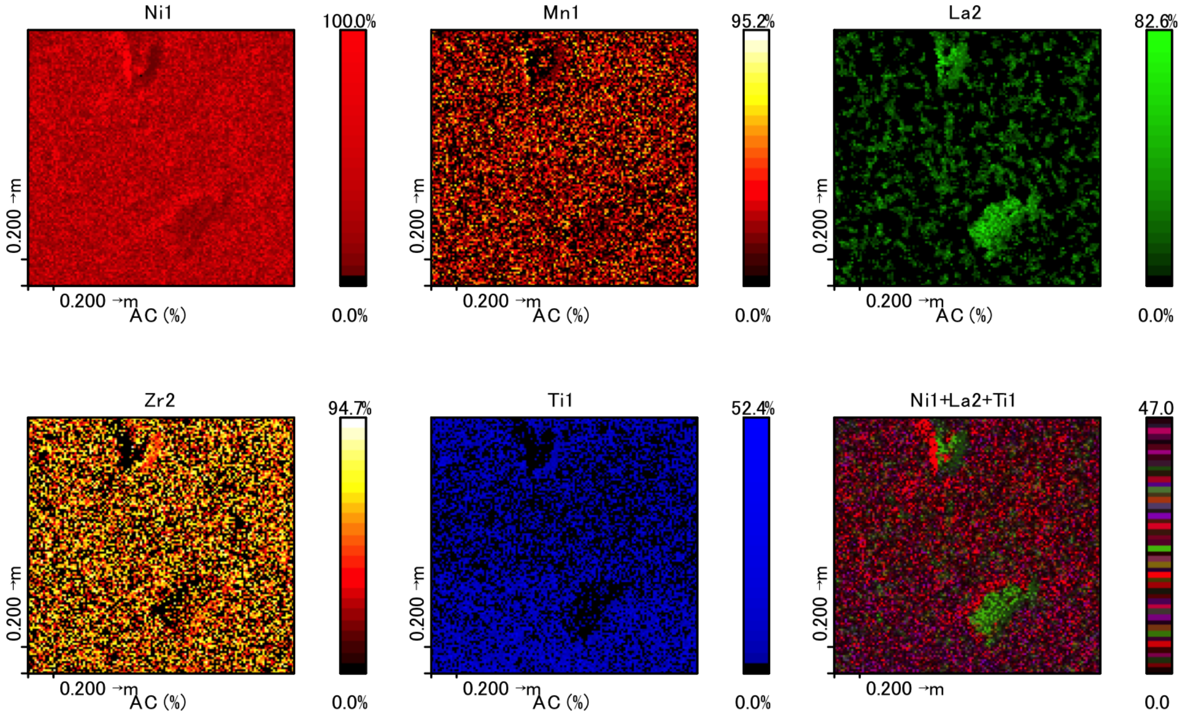

Figure 4.13: The elemental mapping from the Auger analysis of the sample N1-10-33.

The XRD refinement results for the samples of alloy 1 with 10 % added Mn are presented in Figure 4.14 and Table 4.9. The refinements were performed to a data residual, R_w, of 5.275-8.768 %. The graphs show that the amount of the C14 phase increases with rapid solidification, with a maximum for the sample N1-10-5. The unit cell of the C15 phase is almost unchanged with respect to the increase in solidification rate, although it is slightly smaller for the sample N1-10-33. This change is, however, within the margin of error. The trend for the unit cell parameter a of the C14 is unclear, although the c parameter follows a trend opposite to the content of the C14 phase, as the c parameter is at a minimum for the sample N1-10-5.

Table 4.9: XRD data for alloy 1-10

Cell parameter	As cast		N1-10-5		N1-10-16		N1-10-33	
	C14	C15	C14	C15	C14	C15	C14	C15
a (å)	4.995	7.028	4.983	7.030	4.987	7.032	5.002	7.014
c (å)	8.151		8.268		8.082		8.151	
Volume (å^3)	176.142	347.120	177.795	347.461	174.037	347.665	176.613	345.095
Abundance (wt%)	5.2 %	94.8 %	29.1 %	70.9 %	15.7 %	85.3 %	9.6 %	90.4 %
Residual	8.768 %		5.437 %		6.910 %		6.200 %	

Electrochemical Analysis

Furthermore, electrodes were prepared and tested for all 3 RS samples of this alloy as well as for the initial alloy with 10 % Mn addition. A comparison of the activation performance is shown in Figure 4.15. It is clear that the initial alloy shows the fastest activation performance. As expected, this effect is lost for the RS samples, where the sluggish activation is clear. The activation is best for sample N1-10-5 which after only 7 cycles has a stable discharge capacity of 300 mAhg^{-1}. Sample N1-10-16 also reaches stable capacity after only 7 cycles, however, the capacity is only 33 mAhg^{-1}. The reason for this is unknown. Lastly, sample N1-10-33 shows signs of a stable capacity after 17 cycles. When observing the shape of the voltage profiles, as are presented in Figure F.2, of the sample N1-10-33 compared to the initial alloy, it is clear that there is an additional overpotential for this sample, as the voltage plateau for this sample is approximately 0.5 V lower than that of the initial sample and the sample N1-10-5. The repeated electrodes of the sample N1-10-16 and N1-10-33 show that the activation performance of these electrodes are not reproducible.

The voltage profile of these electrodes at varying low current densities, presented in Figure

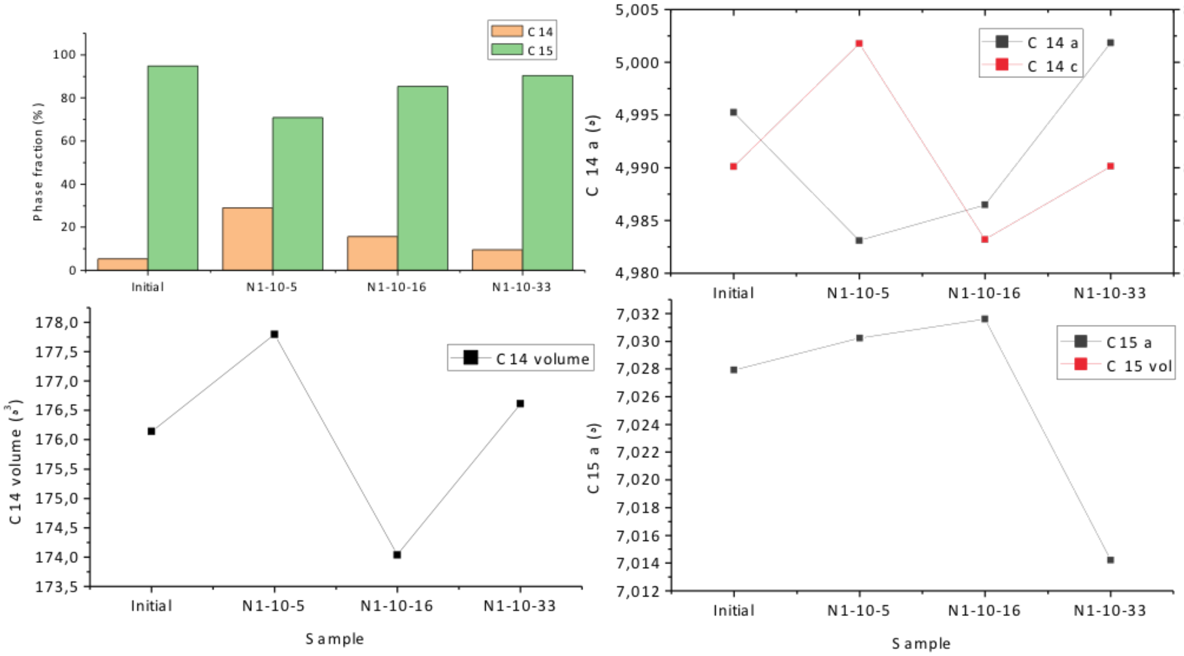

Figure 4.14: XRD results for the as casted and the melt spun ribbons of alloy 1 with 10 % added Mn.

4.16, show an increase in the discharge capacity. However, a second plateau region appears for current densities below 20 mAg^{-1}. The potential of the second plateau is around -0.675 V vs Hg/HgO. As this is a sign of side reactions like corrosion of the metal hydride, the programs of the remaining electrodes were adjusted to start at 10 mAg^{-1}, and a second set of electrodes of sample N1-10-16 and N1-10-33 were made to study the effect of these second plateaus. However, the repeated experiment of sample N1-10-33 shows signs of not having reached full activation, and so the second plateau is again observed for this sample.

The comparison of the discharge capacity as related to the applied current density for all four samples of alloy 1 with 10 % excess Mn, including the two repeated electrodes is presented in Figure 4.17. This shows that the rapidly solidified samples successfully increase the discharge capacity for all current densities for sample N1-10-5 and the repeated sample of N1-10-16. The second plateau region appears to have lowered the discharge capacity of the electrodes, as the three electrodes with the most prominent second plateaus show lower discharge capacities. The loss of discharge capacity with respect to current density shows the same trend for all electrodes, and is small, resulting in a discharge capacity of 286.3 mAhg^{-1} for an applied current density of 450 mAg^{-1} for the sample N1-10-16.

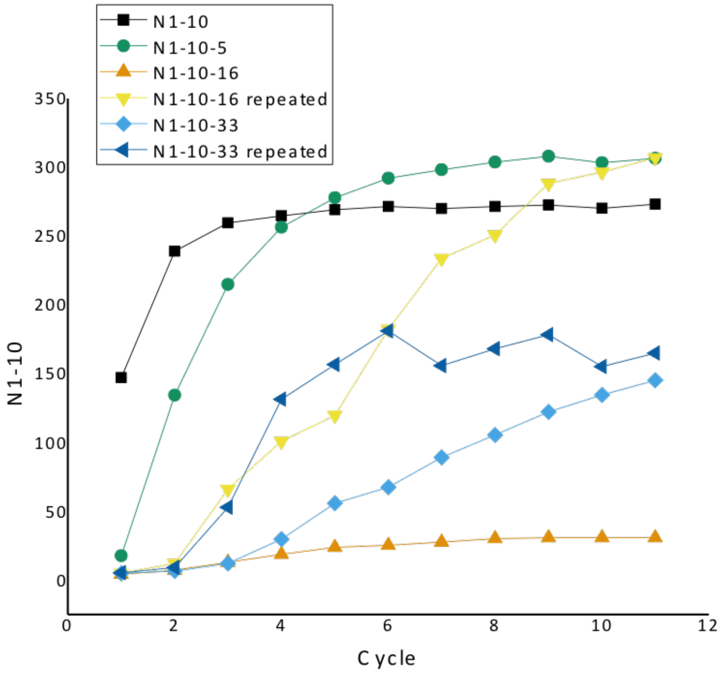

Figure 4.15: The activation performance as described by the discharge capacity as related to the cycle number for the four samples of alloy 1 with 10 % added Mn, with the repeated experiments for sample N1-10-16 and N1-10-33.

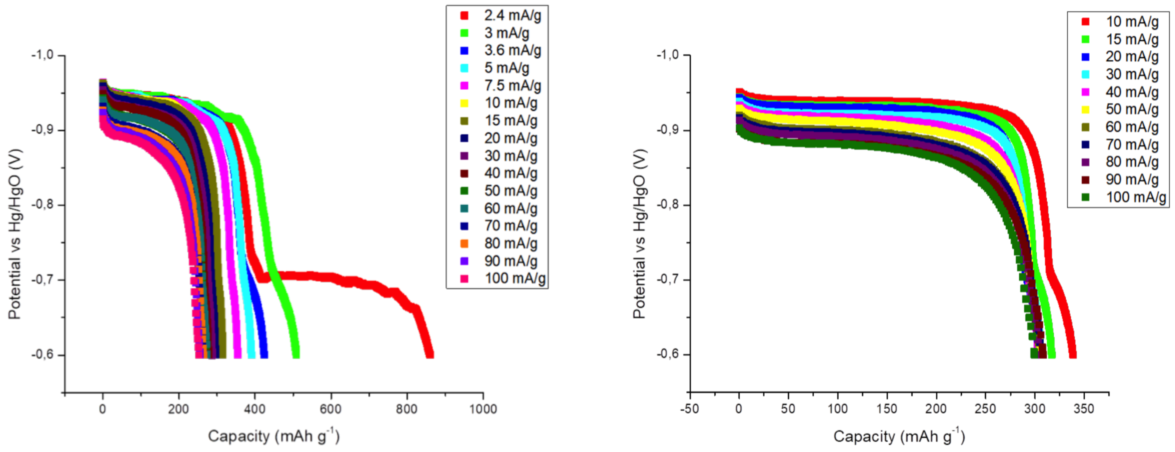

(a) Initial alloy 1-10

(b) N1-10-5

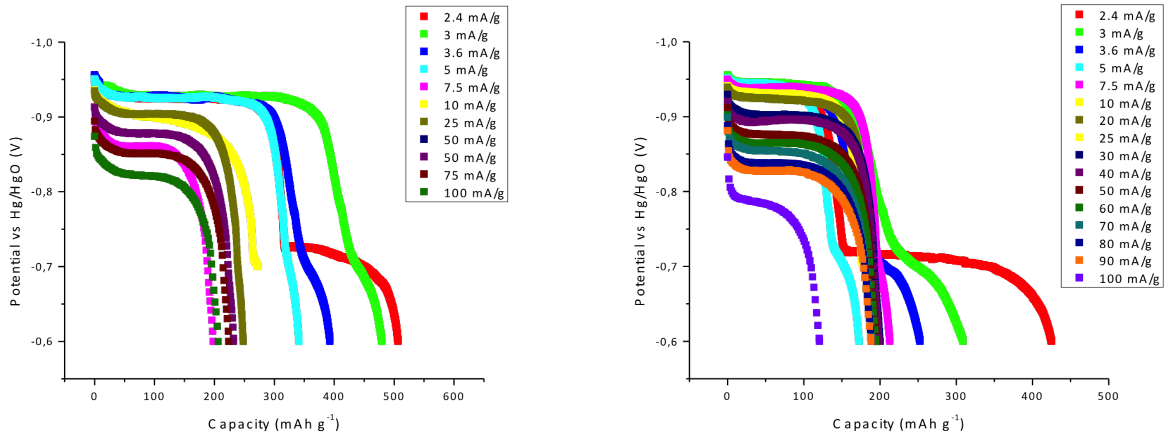

(c) N1-10-16

(d) N1-10-33

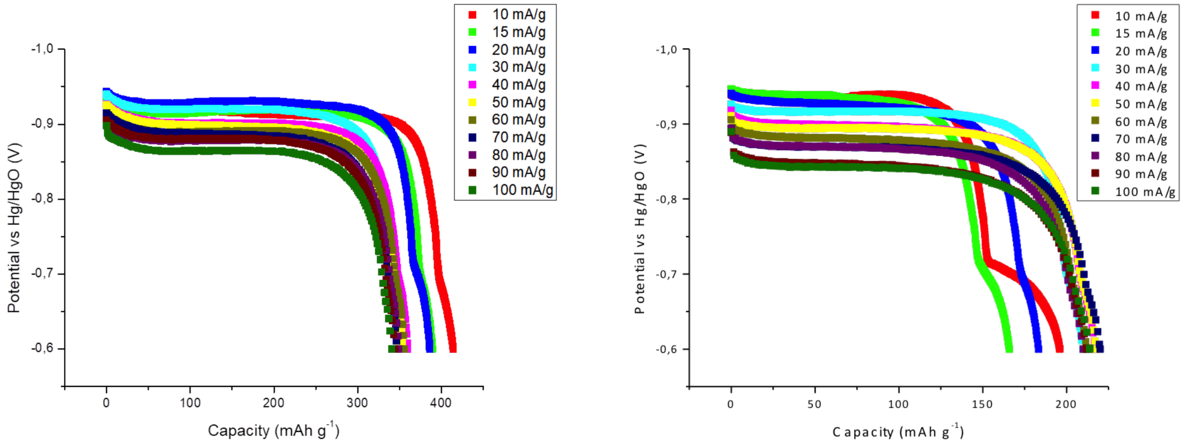

(e) N1-10-16 repeated

(f) N1-10-33 repeated

Figure 4.16: The voltage profiles for the four samples of alloy 1 with 10 % added Mn cycled with low applied current densities, with the repeated experiments for sample N1-10-16 and N1-10-33.

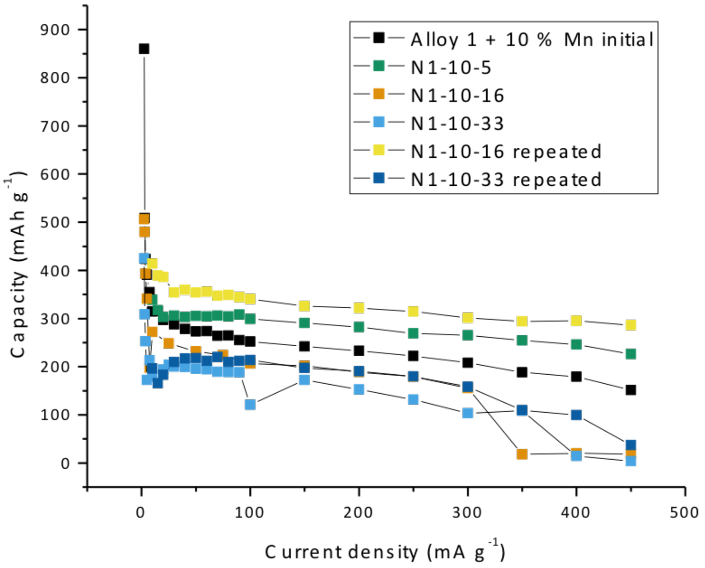

Figure 4.17: The discharge capacity as related to the applied current density for all samples of alloy 1 with 10 % added Mn.

PCT

The PCT result for the sample N1-10-33 compared to an annealed sample of alloy 1 as reference can is presented in Figure 4.18. As can be seen, the desorption plateau pressure is increased from 1.00 bar for the reference to 3.70 for the rapidly solidified sample. Simultaneously, the width of the plateau region is decreased. However, the hysteresis between the hydrogenation and dehydrogenation is reduced from the reference to the rapidly solidified sample, from 1.29 in the reference to only 1.095 in the RS sample, as seen in Table 4.10.

Table 4.10: PCT results for the sample N1-10-33 compared with an annealed sample of alloy 1 as reference.

		N1-10-33	Reference
Mid-plateau pressure (at 0.7 wt.%)	P_{abs} (bar)	4.05	1.29
	P_{des} (bar)	3.70	1.00
Hysteresis	P_{abs}/P_{des}	1.095	1.29
	$\ln(P_{abs}/P_{des})$	0.09	0.25

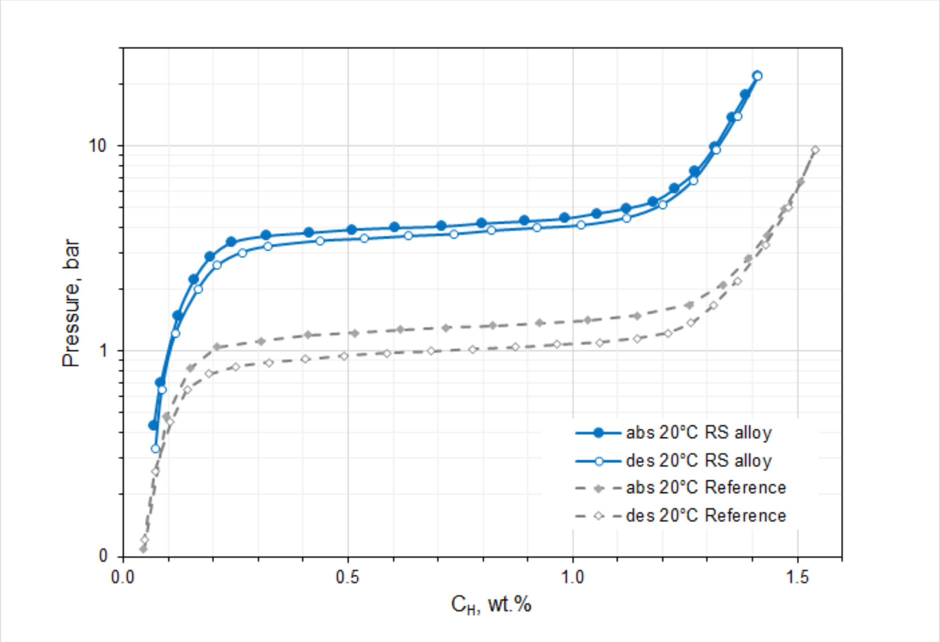

Figure 4.18: The PCT diagram of the sample N1-10-33, with an annealed sample of alloy 1 without Mn addition as a reference.

Impedance

The Nyquist plots from the EIS measurements are presented in Figure 4.19. Evidently, the shape of the Nyquist plots change significantly from the initial alloy to the RS samples. In the initial alloy a single semicircle is the dominant shape, with the exception of the measurement performed at 70 % DOD which appear to have several semicircles superimposed with a shift in the time constant. After the RS the Warburg line is added to the semicircle. For both RS sample, the trend is shown that all impedance measurements are equal in the high frequency region (closest to origo in the graphs), but with higher DOD, the semicircle is elongated further into the low frequency region, and the Warburg line is similarly shifted. Furthermore, a second semicircle is evident for the measurement at 100 % DOD for sample N1-10-16.

The equivalent circuit which gave the best fitting is shown in Figure 4.20, and is based on the model proposed by Kuriyama et al.[48]. This was chosen due to the appearance of a second semicircle for some of the spectra, proving that at least two sets of parallel resistance and capacitances in series must be included. The capacitances were fitted to constant phase elements due to the depressed nature of the semicircles. As the initial alloy has a simpler shape, Q3 and R3 were assumed negligible for this sample to improve the fit.

The physical parallels to the circuit elements are described in several papers [48, 49, 50]. R1 is the electrolyte resistance, and Q_4, R_4 and W_4 can be recognized from Figure 2.15b as the

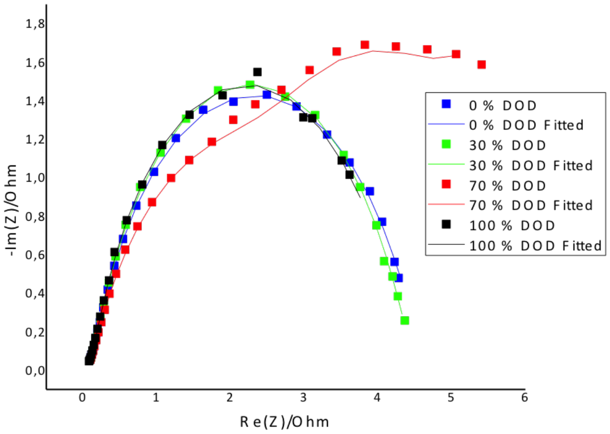

(a) Initial

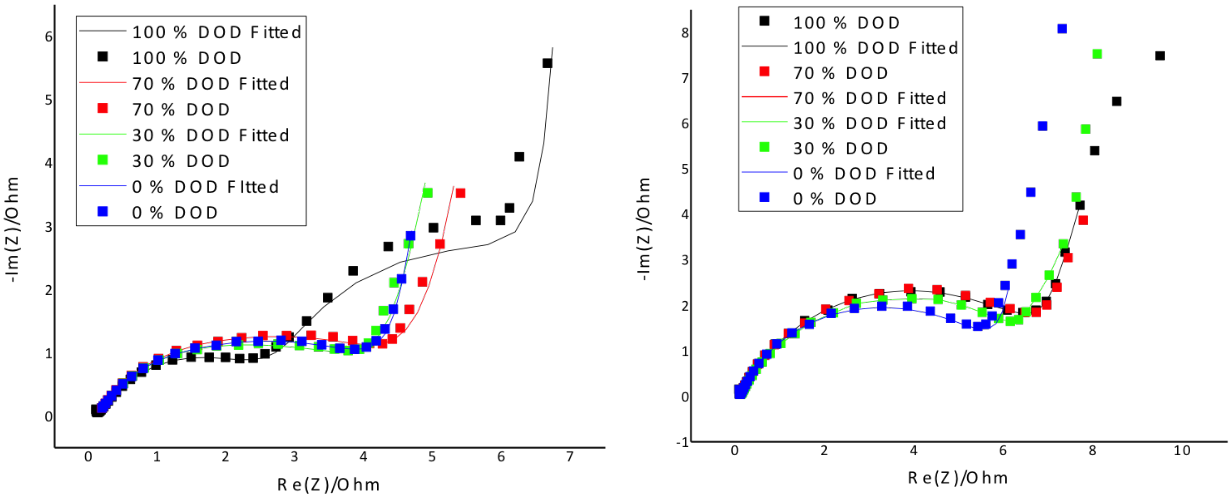

(b) N1-10-16

(c) N1-10-33

Figure 4.19: The Nyquist plots of the experimental results and the fittings for the EIS measurements for the initial (a) as well as the RS samples with rotation frequency 16.5(b) and 33 Hz(c), all three samples of alloy 1 with 10 % added Mn.

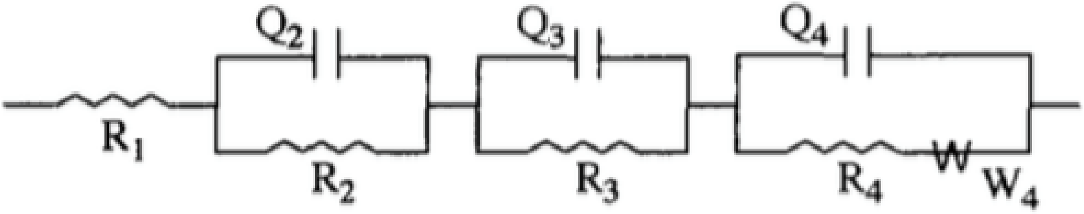

Figure 4.20: The equivalent circuit used to fit the experimental data from the EIS experiments.

double layer capacitance, charge transfer resistance and Warburg impedance, respectively. In addition, Q_2 and R_2 are the capacitance and resistance between the MH particle and the current collector, and Q_3 and R_3 are the capacitance and resistance between the MH particles. Finally, s1 is the Warburg coefficient.

The results of the fitting are presented in Table 4.11, and are shown graphically in Figure 4.21. From the results, it is clear that the initial alloy in general has lower resistances and capacitances, while sample N1-10-33 in general has higher values, with the exceptions of R1 and Q2, where sample N1-10-16 has the highest average values. The particle-current collector capacitance, Q2, appear to have an increase with depth of discharge, especially for sample N1-10-16, while the corresponding resistance, R2, is largest for 30 and 70 %DOD. The particle-particle capacitance, Q3, also shows a trend of having a peak at medium DOD, while the particle-particle resistance, R3, increases with DOD.

The double layer capacitance, Q4, shows an increase for sample N1-10-33, while it shows a small decrease for sample N1-10-16.The charge transfer resistance, R4, is small for both the initial alloy and sample N1-10-16, but shows an increase with DOD for sample N1-10-33. Also the Warburg term, s1, increase with DOD for sample N1-10-33. The initial alloy and sample N1-10-16 however have a significantly larger s1 at low DOD, that decreases with increasing DOD.

4.2.3 Alloy 1-5: $\mathbf{Ti_{0.15}Zr_{0.85}La_{0.03}Ni_{1.2}Mn_{0.70}V_{0.12}Fe_{0.12}}$ with 5 % excess Mn

Metallographic Analysis

SEM images of alloy 1 with 5 % added Mn, Figure 4.22, are consistent with the other alloys in showing a reduction in grain size from the top of the ribbon with an average grain size of 500 nm to the bottom of the ribbon with an average grain size of 300 nm.

The XRD refinement results for alloy 1 with 5 % excess Mn are presented in Table 4.12. Opposite to the other samples, this alloy has a reduction of C14 in the rapidly solidified sample. This may be related to the change of crucible for this sample, resulting in a faster melting of the sample. The unit cell of the C14 is slightly increased in the c parameter, while the C15 decrease in size from the rapid solidification.

Electrochemical Analysis

The activation of the initial alloy 1 with 5 % Mn addition shows the best activation performance of all of the alloys, with stable discharge capacity after only 3 cycles, as presented in

Table 4.11: The results of the impedance fittings using Zfit for the initial alloy with 10 % added Mn as well as sample N1-10-16 and N1-10-33. a3 was found to be 1 for all samples and is thereby excluded.

	Alloy 1 + 10 % Mn as cast				N1-10-16				N1-10-33			
DOD	0 %	30 %	70 %	100 %	0 %	30 %	70 %	100 %	0 %	30 %	70 %	100 %
R1 (Ω)	0.018	1.67e-03	3.60e-04	2.89e-04	0.101	0.093	0.121	0.142	0.104	0.094	0.092	0.085
Q2 (Fs^{a-1})	0.026	0.028	0.029	0.026	0.061	0.037	0.274	0.728	0.034	0.038	0.039	0.132
a2	0.738	0.857	0.863	0.875	0.604	0.659	0.863	1.000	0.746	0.698	0.732	0.980
R2 (Ω)	4.399	2.956	2.760	2.773	4.264	3.921	1.296	3.493	5.000	6.186	5.148	0.288
Q3 (Fs^{a-1})					0.040	0.000	0.032	0.030	0.501	1.097	0.249	0.045
R3 (Ω)					0.360	0.012	3.136	2.706	0.638	0.385	1.786	6.931
Q4 (Fs^{a-1})	9.037	0.586	0.638	0.502	2.336	1.544	1.844	1.113	0.511	1.862	1.979	2.091
a4	0.014	2.22e-16	5.85e-14	5.00e-16	1.000	0.807	0.903	1.000	1.000	0.828	0.997	1.000
R4 (Ω)	3.51e-03	0.058	0.053	0.050	0.015	1.197	0.311	0.607	0.116	1.913	4.957	2.247
s1 ($\Omega s^{1/2}$)	8.835	3.473	3.379	3.628	8.020	8.005	4.717	0.024	0.374	0.047	1.121	2.912
χ^2	0.018	0.023	0.080	0.199	0.015	0.083	0.065	0.698	0.055	0.096	0.021	0.012

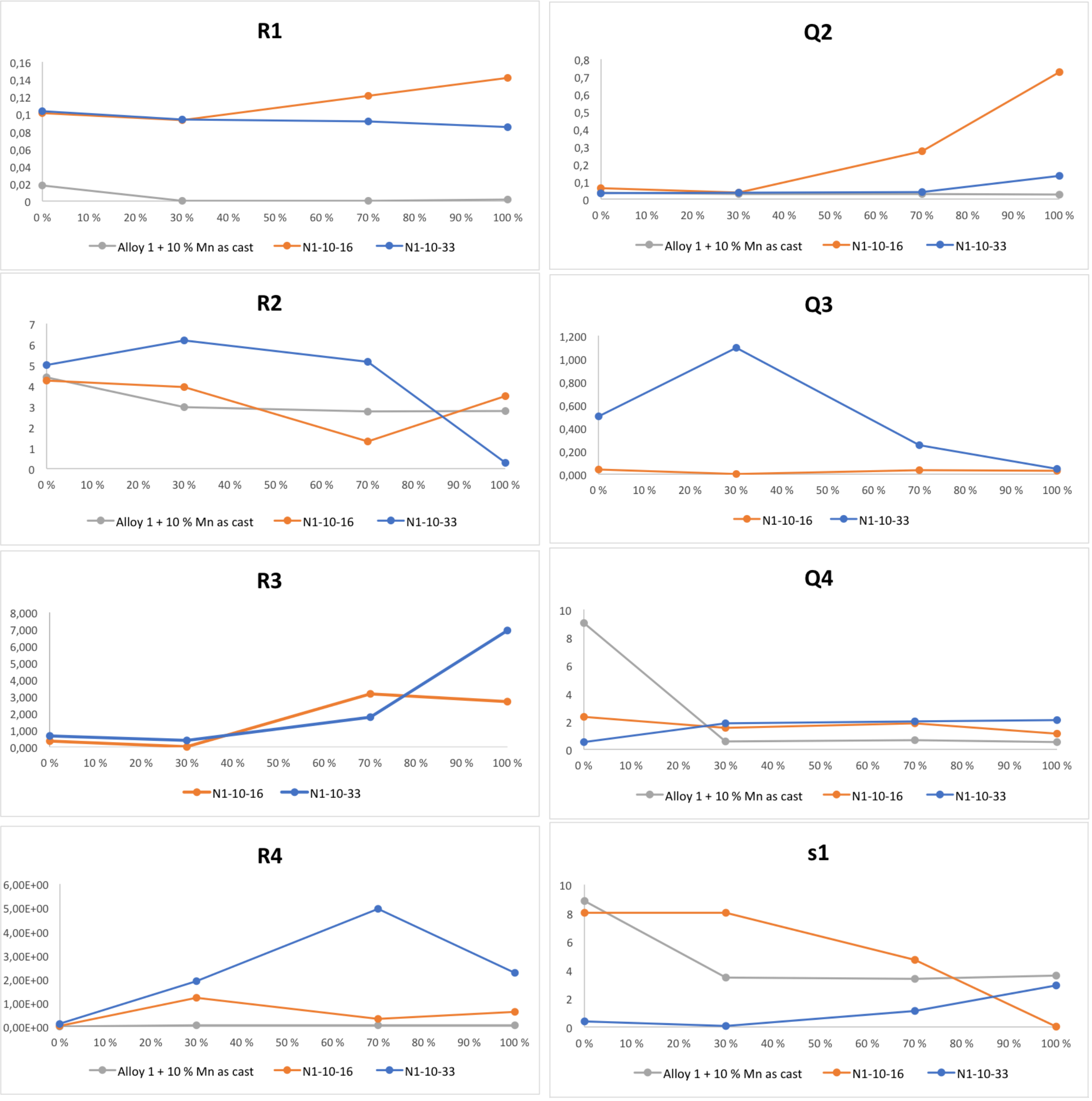

Figure 4.21: The fitted resistances and capacitances and Warburg coefficient of the three samples, as related to the depth of discharge(DOD).

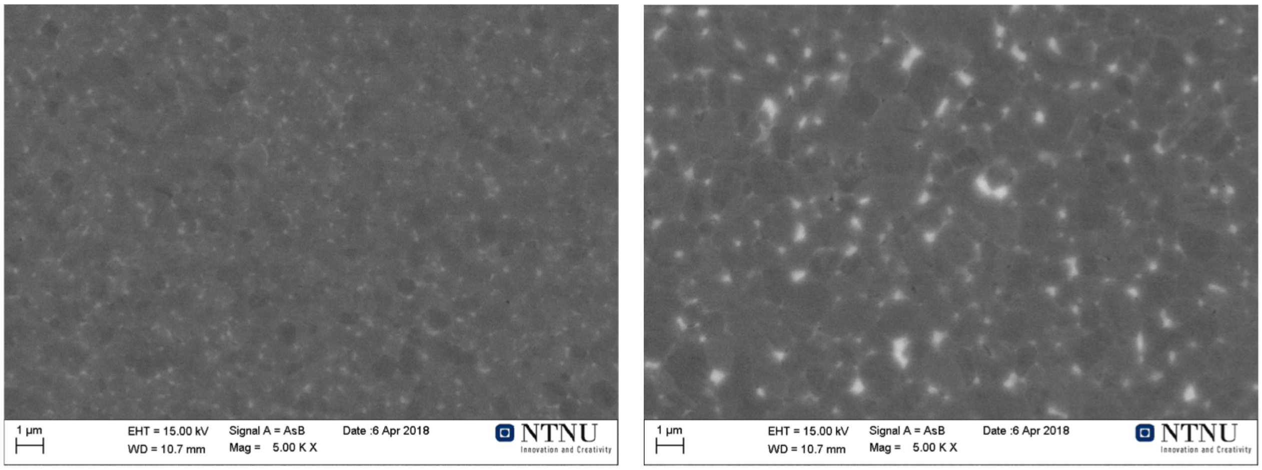

(a) **(b)**

Figure 4.22: SEM images of alloy 1 with 5 % excess Mn from (b) the bottom and (c) the top of the melt spun ribbon with rotation frequency 33 Hz.

Table 4.12: XRD data for alloy 1 with 5 % added Mn

Cell parameter	As cast		N1-5-33	
	C14	C15	C14	C15
a (å)	4.970	7.024	4.968	7.015
c (å)	8.094		8.111	
Volume (å^3)	173.136	346.478	173.359	345.263
Abundance (wt%)	5.5 %	94.5 %	0.7 %	99.3 %
Residual	8.843 %		7.670 %	

Figure 4.23a. The rapid solidification has the same effect as for the other samples in giving a more sluggish activation.

The discharge capacity as related to the applied current density for both the initial and rapidly solidified sample is presented in Figure 4.24. This shows that RS has improved the discharge capacity for all applied current densities.

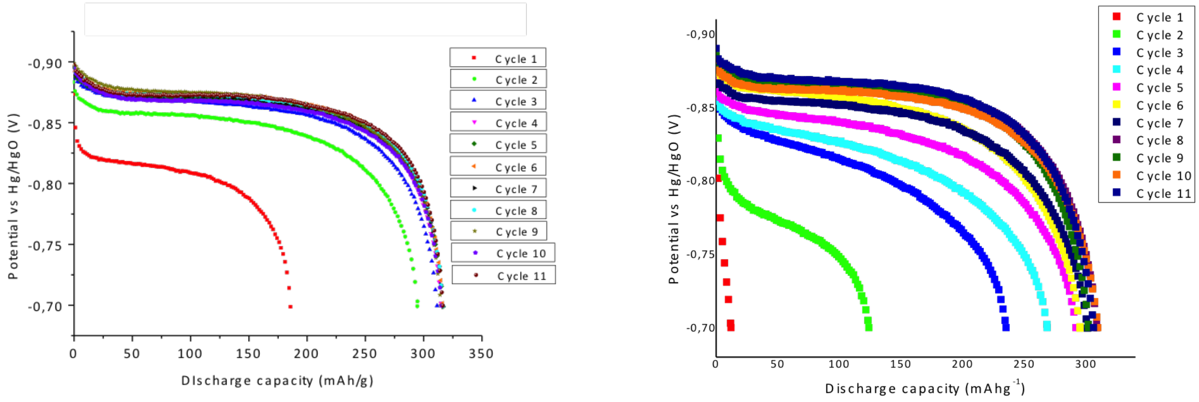

(a)

(b)

Figure 4.23: The voltage profiles of the activation of alloy 1 with 5 % added Mn in the (a) as casted and (b) rapidly solidified state.

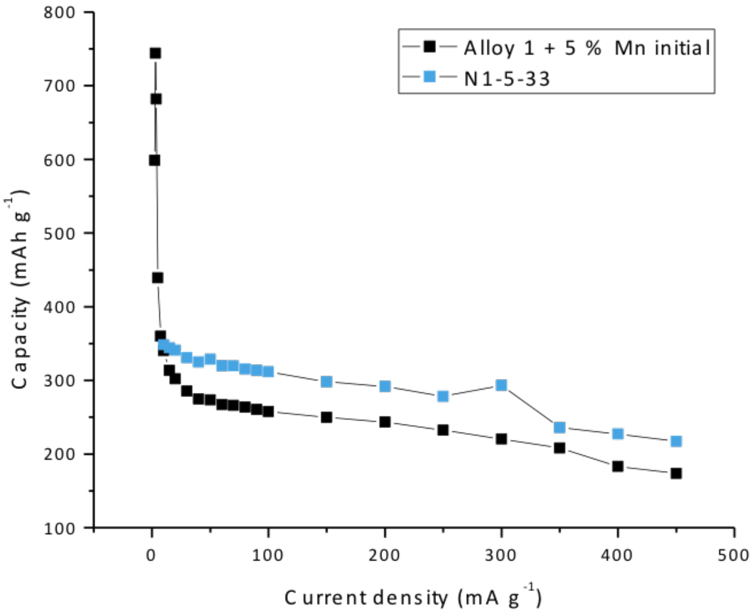

Figure 4.24: The discharge capacity as related to the applied current density for both samples of alloy 1 with 5 % added Mn.

5. Discussion

5.1 Effect of RS on Microstructure

The effect of the variation in cooling speed on the morphology of the casted ribbons is clearly observed by the change in their size. The thickness, which follows the change in solidification rate, is decreased when increasing the cooling speed. However the homogeneity of the ribbons vary. For the ribbons obtained using a rotation frequency of 5 and 16.5 Hz, the width of the ribbons are fairly constant, which is accompanied by a formation of longer ribbons. Although, when looking at the cross sections of these ribbons, the edges are thinner than the center, which could give a variation in solidification rate, and eventually in the grain size of the final product.

For the ribbons obtained with higher cooling rates, the change in thickness is not as large, but the width is more uneven. This could signify a less stable melt puddle during the casting. For the rotation speed 66 and 100 Hz, the casted products could at best be described as individual flakes. This indicates that for these solidification rates, the wheel speed is reaching the limit of the operability window, and the melt is transported away from the puddle region before continuous ribbons are formed. The inhomogeneity of some of the samples casted at 33 Hz shows that the solidification rate for these alloys has not been constant throughout the casting.

The microstructure analysis of the ribbons using SEM shows a successful refinement of the microstructure with increasing solidification speed. Furthermore, the two sets of alloys show different morphological changes in response to the increase in the solidification rate. Both initial alloys contain one main phase with one or two secondary phases. When alloy 1 is rapidly solidified, both the matrix phase and the secondary phase go thorough a grain refinement, and so microstructures with grain size below 1 μm are formed, containing the main matrix phase and particles of the secondary phase on the grain boundaries. As the solidification rate is increased, the number of particles increase as well, but their size decreases. For the sample N1-10-33, the particles are not distinguishable in the SEM image. The XRD-results show that it is still a two-phase system, but probably the particles are too small to be distinguished by SEM.

For the second alloy, the secondary phase is present in the sample B2-5, but for a rotation frequency 16.4 Hz the particles disappear. Instead a lamellar structure is formed. The lamellar structure is also present in some areas of the sample B2-33, but here small equiaxial grains with secondary particles are present in other areas as well. This is, as mentioned earlier, a result of variable casting conditions, although it could also be a result of the change in solidification rate from one side of the ribbon to the other, as described by Liebermann[32]. As the solidification rate of this sample lies at the boundary between the lamellar and equiaxed grain growth, the changes in solidification rate from the bottom to the top, as well as the variation due to an unstable melt puddle, result in an inhomogeneous microstructure obtained during the casting. Finally, the sample obtained at a rotation frequency of 100 Hz shows a microstructure where the secondary phase instead of forming particles has formed a continuous layer on the grain boundaries of the smaller, equiaxed grains.

When discussing the effect of the grain size reduction, the fact that the ribbons are crushed into a powder with a particle size of 40-60 μm to test the materials as anode electrodes has to be considered. While powders made from the initial alloys can have some powder particles containing only the matrix phase or be two phase materials, the RS-samples are much more homogeneous. Thus, smaller particles will still be representative of the properties of the RS materials in contrast to the initial alloys.

5.2 Effect of RS on Phase Composition

The reason for the difference in microstructure between the two sets of alloys is more clear when the results of the EDS and Auger analyses are accounted. It is clear that the secondary particles formed are enriched by La. As the amount of La in the alloys is very small and the radius of La is significantly larger than the other alloying elements, La adds strains to the crystal lattice. Eventually, this leads to easy segregation of La, and is related to the formation of individual La-rich intermetallic particles. As alloy 1 contains three times as much La as compared to alloy 2, it is clear that the segregation of La is larger in alloying system 1. Furthermore, the particles of the secondary phase may hinder the growth of larger grains, and might be one of the reasons why there is no lamellar structure found in alloy 1.

Likewise, the reduction of La content in alloy 2 could be one of the reasons for the lack of particles, as the level of strain in the lattice is lower.

From the Auger analysis of the matrix phase and the particles of alloy 1, the amount of oxygen was clearly higher in the particles. As La is the most easily oxidized out of all the alloying elements, this shows that La-segregation also purifies the matrix phase as the La binds with O when segregating.

The B/A ratio calculated from the EDS data for alloy 1 with 10 % added Mn shows that the matrix phase is hyperstoichiometric. Furthermore, the matrix phase has $e/a>6.8$ which makes it likely that the main phase has the C15 crystal structure. This is confirmed by the XRD data showing presence of >70 wt% C15 phase in all samples of this group. Furthermore, it can be seen that the sample N1-10-5 has the lowest ratio of B/A, and highest content of C14. This could indicate that the increase in the content of the C14 phase for the lowest RS speed is a result of the decrease in the amount of B elements, mainly Mn, after the melt spinning.

Although the EDS analysis of the particles can not be considered as quantitative data, since the particles are smaller than the interaction volume of EDS, the trend that B/A is reduced compared to the matrix phase is clear. The effect of RS on the B/A ratio is however unclear, as the increase in B/A is dominated by the increased contribution of the matrix phase to the detected signal, and not the compositional change of the particles. However, as the $e/a<6.6$ for three of the samples, and the XRD data shows a content of up to 30 wt% of the C14 phase, it can be concluded that these particles mainly consist of the intermetallic with the C14 type crystal structure.

5.3 Activation Performance

When comparing the activation performance of the two sets of alloys, it is clear that the alloy composition is a major contributor to this aspect of the electrochemical performance. While the initial alloy 1 shows a rapid activation, reaching full capacity after only four cycles, the initial alloy 2 is still showing an increase in capacity after 15 cycles. This shows that the increase in the content of La from 0.01 to 0.03 and the change in Ti:Zr ratio from 0.2:0.8 to 0.15:0.85 significantly improves the activation performance as both La and Zr are beneficial for a rapid activation.

In addition, when studying the voltage profiles of the activation there is a change from the stable plateau potential found for alloy 1, to a sloped plateau for alloy 2. Also for the plateau, La has earlier been shown to have a stabilizing effect, which contributes to the observed improvement.

It is clear that the rapid solidification has a negative effect on the activation performance of the alloys. All RS samples have sluggish activation where at least eight cycles must be performed before a full discharge capacity is reached, and after up to 20 cycles an increase in capacity is observed for some samples. One contributor to this behavior could be the refined microstructure, as it is a possibility that the initial hydrogenation process is slowed down by the state of the surface of the ribbons after the melt spinning, as it is probably subjected some surface oxidation. Pretreatments of the metal powders as well as using catalyzing additives should be explored to mitigate the sluggish activation of the RS samples.

Furthermore, the discharge capacity for the final activation cycles is lower for the samples of alloy 2. This could be related to the fact that the activation is not completed as the capacity, although almost stable, still shows a slight increase with additional cycling.

5.4 Effect of Low Rate of Discharge

The discharge capacity of the samples at low current density is high, some samples reaching a maximum at 750 $mAhg_{-1}$, which is above the theoretical limit for this group of metal hydrides. However, while the reason for poor discharge capacity at higher rates is that not all hydrogen can be extracted from the metal hydride, the opposite is the case at lower rates of applied current densities. It is clear that a second plateau region appears when the discharge current densities are low. The assumption can be made that nearly all hydrogen is extracted from the sample, and that another electrochemical half-reaction becomes dominating at the anode. This corresponds to the corrosion of Mn as the alloying element most subjected to the selective corrosion. The second plateaus appear at a potential of approximately 0.65 V, which is also one of the reasons why a cut-off potential of 0.7 V is frequently used when characterizing anodes of the Ni-MH battery, as this will effectively stop the discharging process before the corrosion of the metals begins.

It can be seen that these plateaus gradually decrease with increasing current density, corresponding to increasing overpotentials. From the data obtained for the low current densities, it can be concluded that above 20 mAg^{-1} the corrosion process for all alloys becomes negligible.

5.5 Effect of Alloy Composition on HRD

The high rate discharge ability testing of the alloys prove that even though alloy 2 has a poor activation performance, this alloy has a higher discharge capacity at the lower current densities. However, as can be seen in Figure 5.1, the loss of discharge capacity is higher for alloy 2, and so for current densities of 200 mAg^{-1} and higher, alloy 1 has the highest discharge capacity. This proves that similarly as was concluded by Young et al.[4], the C15 phase, which is dominant for alloy 1, is the most suitable for applications requiring high rates of discharge. However, if the aim of the development is a high capacity and lower current densities can be accepted, the mix of C14 and C15 in alloy 2 is a preferred choice. This also reflects the change in A-element composition, with more Ti in alloy 2.

Furthermore, it can be seen that the two samples with Mn addition show a negative effect on the HRD performance, so the initial alloy 1 without Mn addition has the highest discharge capacity at high current density. This is as expected, since the excess Mn is an addition made to compensate for the loss of Mn during the melt spinning process. However, it shows the sensitivity of the electrochemical performance to the Mn content. However, the initial alloy without any Mn addition was only tested down to 10 mAg^{-1}, while the two alloys with Mn addition were tested down to 2.4 mAg^{-1}, and so the increased loss of capacity at high current density could also be a result of selective corrosion, leading to a decreased amount of Mn as compared to the initial alloy composition. Consequently, studies of the cycled electrodes should be performed to fully characterize both the corrosion product and electrode composition after the cycling. However, we were limited in time to do that during the current project.

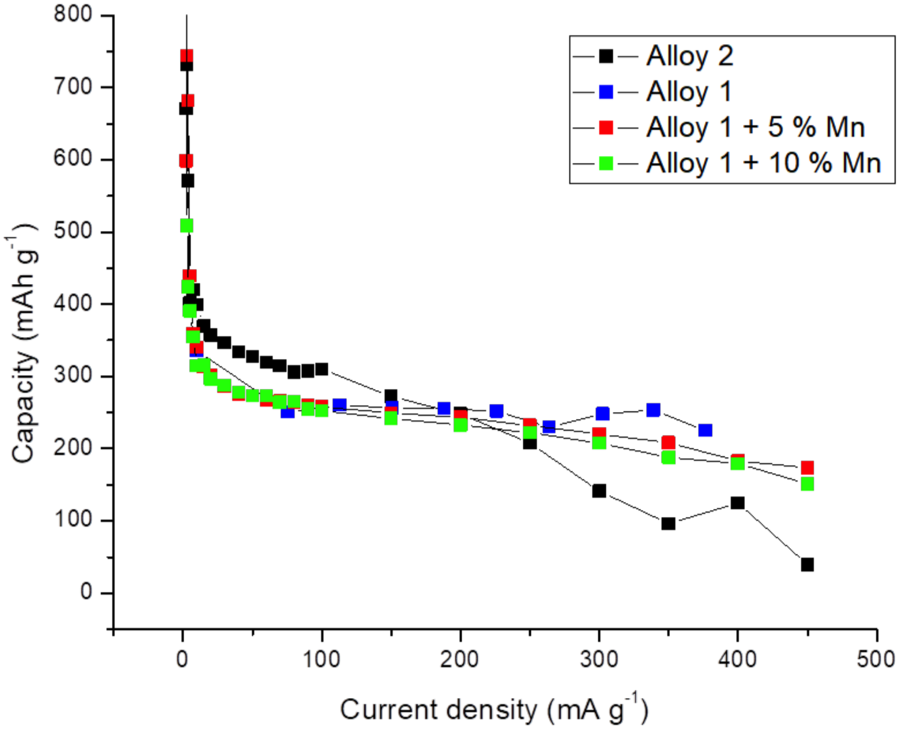

Figure 5.1: The discharge capacity as related to the applied current density for alloy 1 without Mn addition and with 5 and 10 % excess Mn, together with the data for alloy 2.

5.6 Effect of RS on HRD

After the RS both the composition and microstructure of the alloys changed. Figure 5.2 presents a comparison of the rate performance of all the alloys after the performed RS with a rotation frequency of 33 Hz. In addition, rate performance of sample N1-10-16 is added as this was the highest HRD performance for alloy 1 with 10 % Mn which has not undergone corrosion. This shows that the addition of 10 % Mn, which from EDS proved to have a composition very close to the target composition after the RS, has the highest capacity at the high current densities. Consequently the conclusion can be drawn that a Mn content of at least 25 wt%, which requires an addition of 10 % excess Mn before melt spinning, is ideal for this alloy composition as this allows to obtain the targeted composition of the alloy for the electrode.

Furthermore, it can be seen that the loss of discharge capacity for the rapidly solidified sample of alloy 2 and the most corroded samples of alloy 1 follows a similar trend. This further confirms that the corrosion process is likely due to electrochemical oxidation of Mn, and shows the stabilizing effect of Mn on the HRD performance.

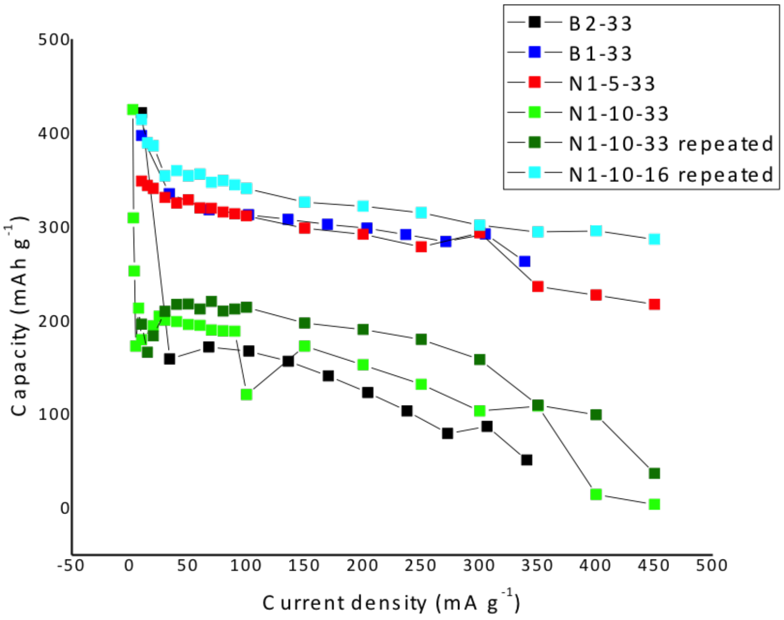

Figure 5.2: The discharge capacity as related to the applied current density for alloy 1 without Mn addition and with 5 and 10 % excess Mn, and for alloy 2, all rapidly solidified at 33 Hz rotation frequency, as well as sample N1-10-16 repeated.

5.7 Effect of RS on the Metal-Hydrogen Interactions

The study of the metal-hydrogen interactions for the sample N1-10-33 shows that the hydrogen plateau pressure is significantly increased by the rapid solidification processing. Indeed, for the annealed reference alloy it is around 1 bar H_2 at room temperature, while for the RS alloy it is increased to approximately 4 bar H_2. Thus, stable hydrides can not be formed in an open electrochemical cell for the RS sample and its electrochemical capacity significantly decreases. As the metal hydride phase is less stable, this further suggests that the phase transition from metal to metal hydride is less favorable in the RS samples during their electrochemical charging in an open cell. This is one of the reasons for the very sluggish activation of the rapidly solidified ribbons compared to the initial alloys.

Furthermore, the electrochemical tests show that the sample N1-10-33 prove to be easily corroded, as both attempts to test the electrode ended with selective corrosion even when the lowest current density applied was as high as 10 mAg^{-1}. The decrease in the metal hydride stability, which has a negative effect on the hydrogenation process occurring during the charging, and slowing down the activation, will have a positive effect on the dehydrogenation process. It can further explain why the RS alloys in a larger degree become dehydrogenated at low current densities, leaving the metal alloy unprotected from the corrosion process.

Electrochemical tests in closed cells with this type of alloys would be interesting to perform, as they will allow to stabilize the hydrides, thus increasing their electrochemical capacity.

5.8 Effect of RS on the Electrode Reactions

From the shape of the impedance diagrams, it appears that the charge transfer reaction is the rate limiting step for the initial alloy due to the single semicircle observed in the diagram in Figure 4.19a. The RS samples show a mixed control mechanism with contributions coming from the charge transfer reaction as well as from the diffusion of hydrogen into the particles, as seen by the semicircle combined with the Warburg line in Figure 4.19b and c. This indicates that the refined microstructure in addition to having increased amounts of grain boundaries for hydrogen diffusion, also shows a catalytic effect on the charge transfer reaction. The presence of the La-rich particles supports this hypothesis, as La acts as a catalyzer of the hydrogenation during the charging process.

As the DOD is increased, the width of the semicircle of the impedance diagram broadens into the low frequency domain, which indicates an increase in the overall resistance of the electrodes.

From the impedance fitting, it can be seen that the resistances of the anode increase after the RS. This indicates that the electrical conductivity of the metal hydride powder is reduced as a consequence of the change in microstructure and elemental composition. Pretreatments of the metal powder to increase the conductivity would therefore improve the electrochemical performance of the alloys.

Furthermore, the Warburg coefficient of sample N1-10-33 is significantly decreased. Additionally, at 100 % DOD, the Warburg coefficient of sample N1-10-16 has decreased to lower values as compared to the initial alloy. This shows that the Warburg coefficient of the alloy is decreased by the nanostructuring, but the effect is mainly observed when the anode is in the metal phase. As the sample goes through the transition from the metal hydride to the metal phase the Warburg coefficient reduces significantly. As the diffusion coefficient is inversely proportional to the square of the Warburg coefficient, this shows that the diffusion coefficient increases as a result of the rapid solidification, especially at high DOD. This is in accordance with the initial hypothesis that the nanostructuring of the metal will increase the diffusion coefficient of the alloys, and hence improve the electrochemical performance when used as an anode material in the Ni-MH battery.

6. Conclusions

This work proved that rapid solidification can successfully be applied to introduce nanostructuring into the TiZr-based Laves phase alloys for battery electrode materials, achieving a reduction in grain size from 2-6 μm to the submicron size as low as 250 nm.

The work has been focused on two groups of alloys with a complex composition which differ from each other by the ratio between Zr and Ti being $Ti_{0.15}Zr_{0.85}$ (alloy 1) or $Ti_{0.2}Zr_{0.8}$ (alloy 2). Changing the ratio Zr/Ti allowed to increase the stability of the hydride (more Zr) or to correspondingly decrease it (more Ti).

Furthermore, the samples contained La, Ni, Mn, V, Fe. Their roles were different and included the following features:

- Small amounts of lanthanum caused formation of La-rich particles acting as a catalyzer of the hydrogenation during the charge of the battery anodes;
- Ni, Fe provided a constant voltage discharge plateau / stable plateau pressure of the metal-gas interaction;
- V, Fe decreased overpotential in the electrochemical system / decreased hysteresis in the phase diagram of metal-gas interactions;
- Mn allowed fine tuning of the stability of the metal hydride.

Particular compositions of the selected alloys were based on the earlier works performed at IFE and were as follows:

Alloy 1 $Ti_{0.15}Zr_{0.85}La_{0.03}Ni_{1.2}Mn_{0.7}V_{0.12}Fe_{0.12}$

Alloy 2 $Ti_{0.2}Zr_{0.8}La_{0.01}Ni_{1.2}Mn_{0.7}V_{0.12}Fe_{0.12}$

The nanostructuring achieved by RS affects the microstructure, the phase-structural composition and the electrochemical properties, allowing to increase the diffusion rate of hydrogen in the alloys and to achieve advanced performance at high rates of charge and discharge of the Ni-MH battery.

The morphology study of the two alloys showed a segregation of La-rich particles in the alloy 1, contributing to the formation of a homogeneous microstructure throughout the ribbons, and hindering the dendrite formation. This resulted in a uniform reduction of the grain size following the increase in solidification rate. Alloy 2, with a lower content of La, does not contain such La-rich particles after the RS, and hence forms dendrites at medium solidification rates.

Furthermore it was proven that the melt spinning process reduces the amount of Mn in the solidified ribbons because of easy vaporization of this metal; thus approximately 10 wt% excess Mn should be added to achieve the desired composition of the product.

From XRD and EDS it was established that the main phase constituent in both alloys were a cubic C15 type Laves phase, with the secondary phase constituent being a hexagonal C14 Laves type intermetallic. The reduction in Mn content by RS resulted in a decrease in the stability of the C15 phase. Alloy 2, which was casted without Mn addition showed the largest increase in the content of the C14 phase by RS.

The activation performance of the alloy 2 with a higher content of Ti, proved to be sluggish. Moreover, alloy 2 has an increased slope of the electrochemical plateau region, both for the initial alloy and the RS samples. Although this alloy has the highest capacity at low current density, the decreased hydride stability by increasing Ti content proved to also reduce the HRD performance, showing that this alloy is inferior to alloy 1 for use in Ni-MH batteries.

Furthermore, RS resulted in sluggish activation also for alloy 1, indicating that additional pretreatments should be applied to improve the activation performance. A probable reason for the sluggish activation is the decreased hydride stability as indicated by an increase in equilibrium desorption plateau pressure in the PCT diagram from 1 to 3.7 bar.

The electrodes were tested at low current density to determine the maximum capacity of the alloys, reaching a maximum of 414 mAhg^{-1} for a melt spun alloy of alloy 1. However, the RS alloys proved to be easily corroded.

The electrochemical impedance spectroscopy showed higher hydrogen diffusion coefficient for the RS samples, confirming that the reduction in grain size improves the diffusion of hydrogen through the alloys.

Finally, the discharge capacity was increased by 135 mAhg^{-1} from the initial to the RS alloy at the highest applied current density of 450 mAg^{-1}. This confirmed that the microstructural refinement by RS increases the diffusion coefficient of hydrogen through the material, improving the HRD performance of the alloy.

Bibliography

[1] L. A. Hammond. Toyota battery for Electric Vehicle breakthrough. *Driving the Nation*, July 2017.

[2] NiMH Batteries Could Yet Again Power Electric Cars Says BASF, Thanks to Ten-Fold Increase in Energy Density.

[3] T.-K. Ying, X.-P. Gao, W.-K. Hu, F. Wu, and D. Noréus. Studies on rechargeable NiMH batteries. *International Journal of Hydrogen Energy*, 31(4):525–530, March 2006. ISSN 0360-3199.

[4] K. Young, J. Nei, C. Wan, R. V. Denys, and V. A. Yartys. Comparison of C14- and C15-Predomiated AB2 Metal Hydride Alloys for Electrochemical Applications. *Batteries*, 3(3), 2017. ISSN 2313-0105.

[5] C. Wan, A.A. Volodin, R. V. Denys, M. Lelis, D. Milčius, B.P. Tarasov, and V. A. Yartys. Presented at International Symposium on Metal-Hydrogen Systems. Fundamental and Applications., August 2016.

[6] N. S. Nazer. *High power batteries probed by neutron scattering.* PhD Thesis, NTNU, Trondheim, Norway, May 2017.

[7] K. B. Oldham. *Electrochemical Science and Technology : Fundamentals and Applications (1).* John Wiley & Sons, Incorporated, Hoboken, November 2011. ISBN 978-1-119-96684-5.

[8] C. G. Zoski. *Handbook of electrochemistry.* Elsevier, 2006.

[9] Y. Liu, H. Pan, M. Gao, and Wang. Q. Advanced hydrogen storage alloys for ni/mh rechargeable batteries. *Journal of Materials Chemistry*, 21:4743–4755, March 2011. ISSN 1364-5501.

[10] W. B. Pearson. In *The crystal chemistry and physics of metals and alloys*, Wiley series on the science and technology of materials, pages 24–31. Wiley-Interscience, New York, 1972. ISBN 978-0-471-67540-2.

[11] L. Chen, F. Wu, M. Tong, D. M. Chen, R. B. Long, Z. Q. Shang, H. Liu, W. S. Sun, K. Yang, L. B. Wang, and Y. Y. Li. Advanced nanocrystalline Zr-based AB2 hydrogen storage electrode materials for NiMH EV batteries. *Journal of Alloys and Compounds*, 293(Supplement C):508 – 520, 1999. ISSN 0925-8388.

[12] J. Nei, K. Young, S. O. Salley, and K. Y. S. Ng. Determination of C14/C15 phase abundance in Laves phase alloys. *Materials Chemistry and Physics*, 136(2):520–527, October 2012. ISSN 0254-0584.

[13] S. Hong and C. L. Fu. Hydrogen in Laves phase ZrX2 (X=V,Cr,Mn,Fe,Co,Ni) compounds: Binding energies and electronic and magnetic structure. *Physical Review B*, 66(9):094109, September 2002.

[14] K. Young, J. M. Koch, C. Wan, R. V. Denys, and V. A. Yartys. Cell Performance Comparison between C14- and C15-Predomiated AB2 Metal Hydride Alloys. *Batteries*, 3(4):29, September 2017.

[15] L. O. Valøen, A. Lasia, J. O. Jensen, and R. Tunold. The electrochemical impedance of metal hydride electrodes. *Electrochimica Acta*, 47(18):2871–2884, July 2002. ISSN 0013-4686.

[16] M. V. Lototskyy, V. A. Yartys, B. G. Pollet, and R. C. Bowman. Metal hydride hydrogen compressors: A review. *International Journal of Hydrogen Energy*, 39(11): 5818–5851, April 2014. ISSN 0360-3199.

[17] K. Young, J. Nei, T. Ouchi, and M. A. Fetcenko. Phase abundances in AB2 metal hydride alloys and their correlations to various properties. *Journal of Alloys and Compounds*, 509(5):2277–2284, February 2011. ISSN 0925-8388.

[18] V. Yartys, D. Noreus, and M. Latroche. Metal hydrides as negative electrode materials for Ni–MH batteries. *Applied Physics A*, 122(1):43, January 2016. ISSN 0947-8396, 1432-0630.

[19] E. Jankowska, M. Makowiecka, and M. Jurczyk. Electrochemical performance of sealed NiMH batteries using nanocrystalline TiNi-type hydride electrodes. *Renewable Energy*, 33(2):211–215, February 2008. ISSN 0960-1481.

[20] Y. Zhang, J. Li, T. Zhang, T. Wu, H. Kou, and X. Xue. Hydrogenation thermokinetics and activation behavior of non-stoichiometric Zr-based Laves alloys with enhanced hydrogen storage capacity. *Journal of Alloys and Compounds*, 694(Supplement C): 300–308, February 2017. ISSN 0925-8388.

[21] L. E. O. C. Rodrigues and M. B. Mansur. Hydrometallurgical separation of rare earth elements, cobalt and nickel from spent nickel–metal–hydride batteries. *Journal of Power Sources*, 195(11):3735–3741, June 2010. ISSN 0378-7753.

[22] L. Pietrelli, B. Bellomo, D. Fontana, and M. Montereali. Characterization and leaching of NiCd and NiMH spent batteries for the recovery of metals. *Waste Management*, 25 (2):221–226, January 2005. ISSN 0956-053X.

[23] K. Young, T. Ouchi, J. Koch, and M. A. Fetcenko. The role of Mn in C14 Laves phase multi-component alloys for NiMH battery application. *Journal of Alloys and Compounds*, 477(1):749–758, May 2009. ISSN 0925-8388.

[24] K. Young, D.F. Wong, L. Wang, J. Nei, T. Ouchi, and S. Yasuoka. Mn in misch-metal based superlattice metal hydride alloy – Part 1 structural, hydrogen storage and electrochemical properties. *Journal of Power Sources*, 277:426–432, March 2015. ISSN 0378-7753.

[25] X. B. Yu, Z. X. Yang, S. L. Feng, Z. Wu, and N. X. Xu. Influence of Fe addition on hydrogen storage characteristics of Ti–V-based alloy. *International Journal of Hydrogen Energy*, 31(9):1176–1181, August 2006. ISSN 0360-3199.

[26] K. Young, M. A. Fetcenko, F. Li, T. Ouchi, and J. Koch. Effect of vanadium substitution in C14 Laves phase alloys for NiMH battery application. *Journal of Alloys and Compounds*, 468(1):482–492, January 2009. ISSN 0925-8388.

[27] G. H Aylward. *Si chemical data.* Wiley, Milton, 6th ed. edition, 2008. ISBN 978-0-470-81638-7.

[28] R. R. Hultgren. *Selected values of thermodynamic properties of metals and alloys,.* New York,, 1963.

[29] W. D. Callister and D. G. Rethwisch. *Materials Science and Engineering.* Wiley, 8th edition si version edition, 2011. ISBN 978-0-470-50586-1.

[30] M. Telford. The case for bulk metallic glass. *Materials Today*, 7(3):36–43, March 2004. ISSN 1369-7021.

[31] M. Kamal and U. S. Mohammad. *A review: chill-block melt spin technique, theories & applications.* Bentham Science Publishers, 2012.

[32] H. H. Liebermann. Rapidly solidified alloys made by chill block melt-spinning processes. *Journal of Crystal Growth*, 70(1):497–506, December 1984. ISSN 0022-0248.

[33] T. J. Praisner, J. S. J. Chen, and A. A. Tseng. An experimental study of process behavior in planar flow melt spinning. *Metallurgical and Materials Transactions B*, 26 (1):1199–1208, February 1995. ISSN 1543-1916.

[34] P. H. Steen and C. Karcher. Fluid Mechanics of Spin Casting of Metals. *Annual Review of Fluid Mechanics*, 29(1):373–397, 1997.

[35] Y.G. Su, F. Chen, C.M. Chang, C.Y. Wu, M.H. Chang, and C. A. Chung. Tuning the Planar-Flow Melt-Spinning Process Subject to Operability Conditions. *JOM*, 66(7): 1277–1286, July 2014. ISSN 1047-4838, 1543-1851.

[36] B. D Cullity. *Elements of X-ray diffraction*. Prentice Hall, Upper Saddle River, N.J, 3rd ed. edition, 2001. ISBN 0-201-61091-4.

[37] electron diffraction, . URL `http://www.microscopy.ethz.ch/bragg.htm`.

[38] S. J. L. Billinge and Robert E. Dinnebier. Rietveld refinement. In *Powder Diffraction : Theory and Practice*. Royal Society of Chemistry, Cambridge, 2008. ISBN 978-0-85404-231-9.

[39] E. J. Mittemeijer and U. Welzel. *Modern Diffraction Methods*. John Wiley & Sons, Incorporated, Weinheim, GERMANY, 2012. ISBN 978-3-527-64990-7. URL `http://ebookcentral.proquest.com/lib/ntnu/detail.action?docID=1124684`.

[40] Claudionico. Wikimedia Commons illustration, December 2013. URL `upload.wikimedia.org/wikipedia/commons/4/49/ElectronInteractionwithMatter.svg`.

[41] J. I. Goldstein and et al. *Scanning electron microscopy and X-ray microanalysis*. Kluwer Academic/Plenum Publishers, New York, 3rd ed. edition, 2003. ISBN 0-306-47292-9.

[42] M. Abd Mutalib, M. A. Rahman, M. H. D. Othman, A. F. Ismail, and J. Jaafar. Chapter 9 - Scanning Electron Microscopy (SEM) and Energy-Dispersive X-Ray (EDX) Spectroscopy. In *Membrane Characterization*, pages 161–179. Elsevier, 2017. ISBN 978-0-444-63776-5. doi: 10.1016/B978-0-444-63776-5.00009-7.

[43] J. Widheden and E. Ringström. 2.2 - Life Cycle Assessment. In I. Johansson and P. Somasundaran, editors, *Handbook for Cleaning/Decontamination of Surfaces*, pages 695 – 720. Elsevier Science B.V., Amsterdam, 2007. ISBN 978-0-444-51664-0. doi: 10.1016/B978-044451664-0/50021-8.

[44] A. K. Singh. Chapter 4 - Experimental Methodologies for the Characterization of Nanoparticles. In *Engineered Nanoparticles*, pages 125 – 170. Academic Press, Boston, 2016. ISBN 978-0-12-801406-6. doi: 10.1016/B978-0-12-801406-6.00004-2.

[45] T. P. Chernyayeva and Artem Ostapov. Hydrogen in zirconium part 1. *Problems of Atomic Science and Technology*, 87, July 2013.

[46] J. C. Lindon, G. E Tranter, and D. Koppenaal. *Encyclopedia of spectroscopy and spectrometry.* Academic Press, 2016.

[47] C.H Hamann. *Electrochemistry.* Wiley, Weinheim, 2nd, completely rev. and updated ed. edition, 2007. ISBN 978-3-527-31069-2.

[48] N. Kuriyama, T. Sakai, H. Miyamura, I. Uehara, H. Ishikawa, and T. Iwasaki. Electrochemical impedance and deterioration behavior of metal hydride electrodes. *Journal of Alloys and Compounds*, 202(1-2):183–197, 1993.

[49] Y. Liu, H. Pan, M. Gao, R. Li, X. Sun, and Y. Lei. Investigation on the characteristics of La0.7mg0.3ni2.65mn0.1co0.75+x (x = 0.00–0.85) metal hydride electrode alloys for Ni/MH batteries Part II: Electrochemical performances. *Journal of Alloys and Compounds*, 388(1):109–117, February 2005. ISSN 0925-8388.

[50] G. Hapçı Ağaoğlu and G. Orhan. Elaboration and electrochemical characterization of Mg–Ni hydrogen storage alloy electrodes for Ni/MH batteries. *International Journal of Hydrogen Energy*, 42(12):8098–8108, March 2017. ISSN 0360-3199.

[51] B. H. Toby and R.B. von Dreele. GSAS-II: the genesis of a modern open-source all purpose crystallography software package. *Journal of Applied Crystallography*, 46(2): 544–549, 2013.

[52] Periodic Table and X-Ray Energies, . URL `www.bruker.com/hhxrf`.

A. List of Abbreviations

AES Auger electron spectroscopy
BSE Back scattered electrons
CBMS Chill block melt spinning
CE Counter electrode
DOD Depth of Discharge
e/a Average electron density
EDS Energy dispersive spectroscopy
EIS Electrochemical impedance spectroscopy
HRD High rate discharge ability
LRD Low rate discharge ability
MH Metal hydride
Ni-MH Nickel metal hydride
PCT Pressure-Composition-Temperature
PFMS Planar flow melt spinning
RS Rapid solidification
REF Reference electrode
RE Rare earth metal
SD Standard deviation
SE Secondary electrons
SEM Scanning electron microscopy
WE Working electrode
XRD X-Ray diffraction

B. Table of the X-Ray Energies

Table B.1: The X-Ray energy of a selection of the periodic elements. Data from Bruker[52]

Element	Kα_1	Kβ_1	Lα_1	Lβ_1
C	0.277			
O	0.525			
Al	1.486	1.557		
Ti	4.512	4.933	0.452	0.458
V	4.953	5.428	0.510	0.518
Mn	5.900	6.492	0.637	0.648
Fe	6.405	7.059	0.705	0.718
Ni	7.480	8.267	0.849	0.866
Zr	15.775	17.668	2.044	2.126
La	33.442	37.797	4.647	5.038

C. Rietveld Refinement

Phase C14

The parameters used for initialization of phase C14 were as follows:

Space group P 63/m m c
a 4.967873
c 8.110987
alpha 90
beta 90
gamma 120
volume 173.359

Table C.1

label	element	mult	x	y	z	fraction	Uiso
Zr1	Zr	12	0.333333	0.666666	0.064000	0.850	0.1000
Ti1	Ti	24	0.333333	0.666666	0.064000	0.150	0.1000
Ni1	Ni	2	0.000000	0.000000	0.000000	0.560	0.1000
V1	V	2	0.000000	0.000000	0.000000	0.056	0.1000
Fe1	Fe	2	0.000000	0.000000	0.000000	0.056	0.1000
Mn1	Mn	2	0.000000	0.000000	0.000000	0.330	0.1000
Ni2	Ni	6	0.830000	0.660000	0.250000	0.560	0.1000
V2	V	6	0.830000	0.660000	0.250000	0.056	0.1000
Fe2	Fe	6	0.830000	0.660000	0.250000	0.056	0.1000
Mn2	Mn	6	0.830000	0.660000	0.250000	0.330	0.1000

Phase C15

The parameters used for initialization of phase C15 were as follows:

Space group F d-3 m
a 7.015359
alpha 90
beta 90
gamma 90
volume 345.263

Table C.2

label	element	mult	x	y	z	fraction	Uiso
Zr	Zr	8	0.125000	0.125000	0.125000	0.850	0.1000
Ti	Ti	8	0.125000	0.125000	0.125000	0.150	0.1000
Ni	Ni	16	0.500000	0.500000	0.500000	0.560	0.1000
V	V	16	0.500000	0.500000	0.500000	0.056	0.1000
Fe	Fe	16	0.500000	0.500000	0.500000	0.056	0.1000
Mn	Mn	16	0.500000	0.500000	0.500000	0.330	0.1000

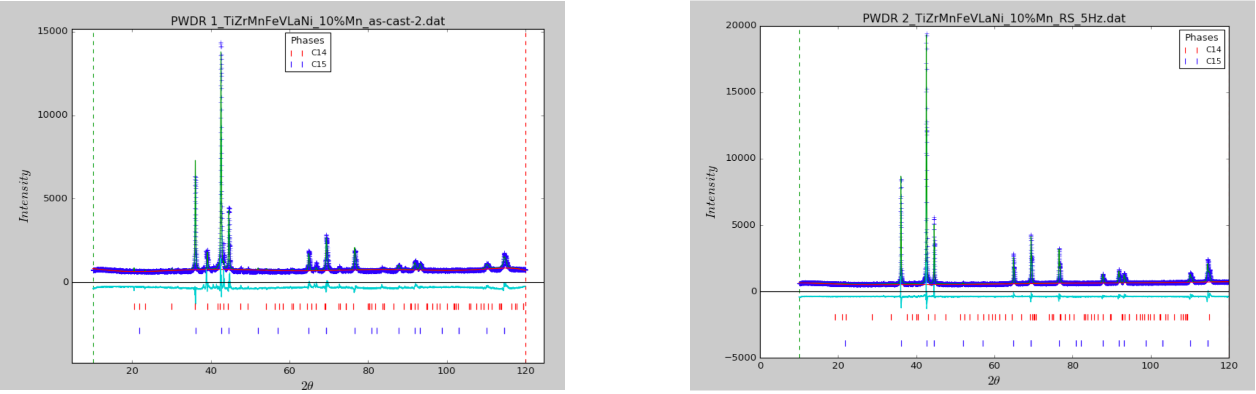

(a) Alloy 1 + 10% Mn as cast

(b) Alloy 1 + 10% Mn RS 5 Hz

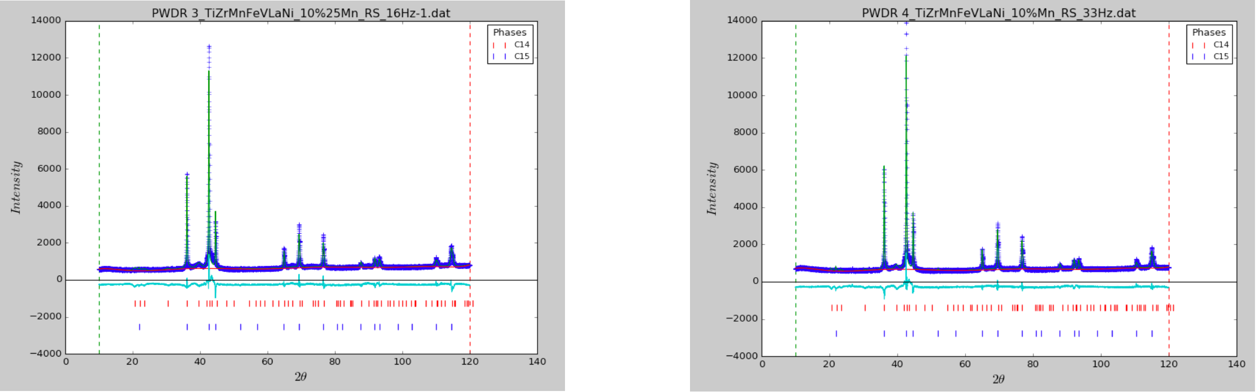

(c) Alloy 1 + 10% Mn RS 16.5 Hz

(d) Alloy 1 + 10% Mn RS 33 Hz

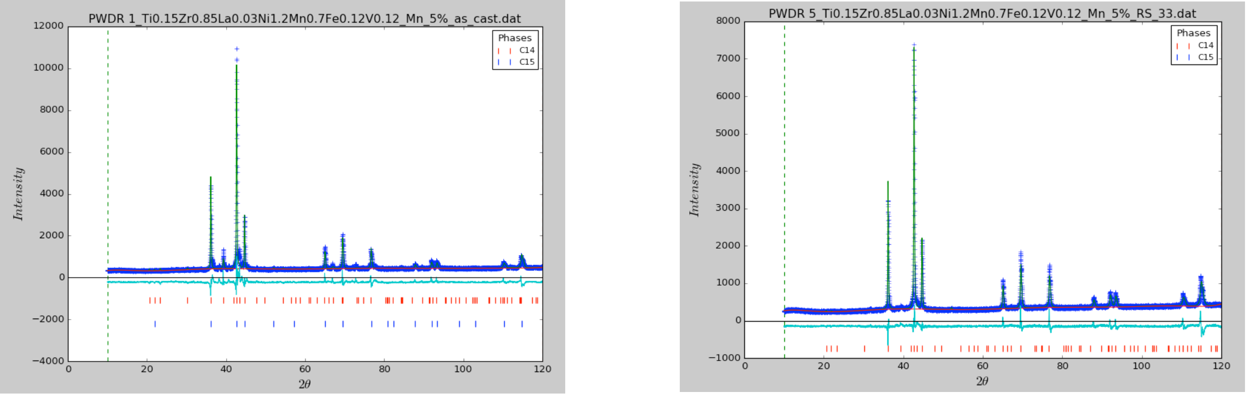

(e) Alloy 1 + 5% Mn as cast

(f) Alloy 1 + 5% Mn RS 33 Hz

Figure C.1: The XRD spectra of the obtained (blue), calculated (green), background (red) and the error between calculated and observed(turquoise) for all four samples of alloy 1 with 10 % added Mn as well as the initial and RS sample with 5 % added Mn.

D. Energy Dispersive Spectroscopy

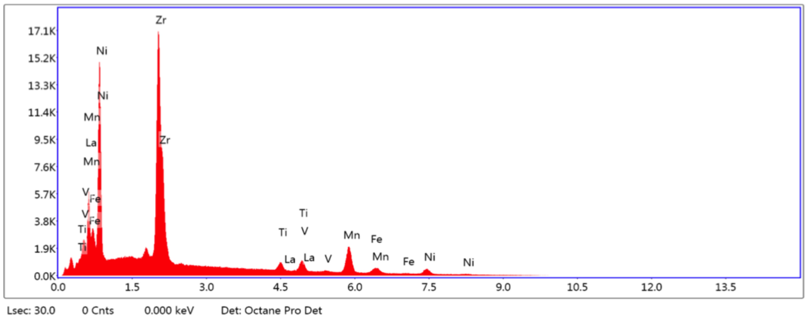

(a) EDS spectra from a larger area for initial alloy 1 with 10 % added Mn.

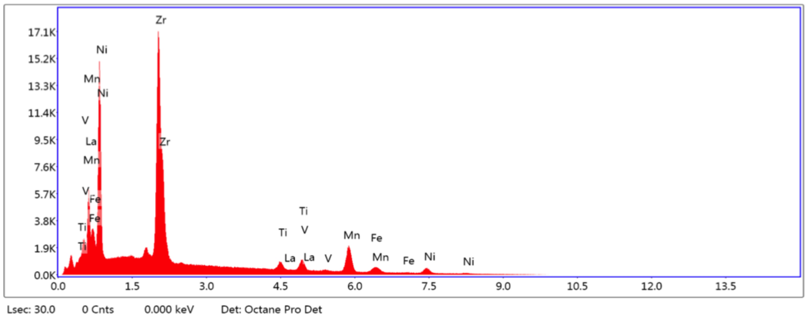

(b) EDS spectra from the main phase for initial alloy 1 with 10 % added Mn.

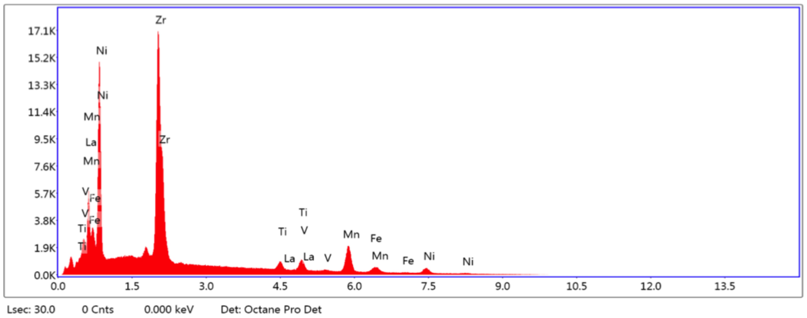

(c) EDS spectra from a particle of initial alloy 1 with 10 % added Mn.

Figure D.1

.

Table D.1: The EDS results for alloy 2 with the atomic percentage of each element, and the standard deviation. Datasets marked * are where the matrix appears to contain more than 1 phase.

	Matrix phase															
Sample	Alloy 2		Alloy 2*		B2-5 bottom		B2-5 top		B2-16		B2-33		B2-100		B2-100*	
	Mean	SD	Mean	SD	Mean	SD	Mean	SD	Mean	SD	Mean	SD	Mean	SD	Mean	SD
Zr	24.44	0.19	19.75	0.18	20.83	0.31	20.62	0.15	21.30	0.30	20.51	0.13	21.37	1.11	19.73	0.19
Ti	14.62	0.83	31.48	0.43	12.39	0.42	13.18	0.11	13.69	0.16	13.54	0.17	11.66	1.50	13.64	1.08
La	3.20	0.02	3.82	0.05	0.98	0.17	1.06	0.20	0.40	0.24	0.80	0.15	1.09	0.11	1.21	0.30
V	14.14	0.87	0.89	0.06	14.12	0.80	12.67	0.11	13.22	0.09	12.62	0.15	14.80	2.08	12.06	1.32
Mn	13.08	0.5	3.24	0.06	12.29	0.88	11.17	0.15	11.32	0.24	10.84	0.25	13.60	2.32	10.50	1.21
Fe	0.15	0.06	0.24	0.06	0.75	0.16	0.75	0.12	0.78	0.18	0.86	0.12	0.87	0.16	0.84	0.43
Ni	30.37	1.06	40.59	0.09	38.63	1.45	40.55	0.20	39.29	0.25	40.83	0.23	36.61	4.13	42.02	1.87
B/A	1.37		0.82		1.92		1.87		1.83		1.87		1.93		1.89	
e/*a*	6.33		6.51		6.85		6.91		6.86		6.93		6.78		6.98	

	Secondary phase											
Sample	Alloy 2		B2-5 bottom		B2-5 top		B2-16		B2-33		B2-100	
	Mean	SD	Mean	SD	Mean	SD	Mean	SD	Mean	SD	Mean	SD
Zr	50.17	0.63	20.31	0.31	20.55	0.17	21.35	0.22	20.61	0.28	19.60	0.21
Ti	8.65	0.41	13.75	0.95	13.22	0.18	13.74	0.18	13.58	0.24	14.04	0.47
La	0.92	0.06	0.91	0.19	1.03	0.18	0.56	0.09	0.73	0.26	1.09	0.20
V	0.29	0.04	9.21	1.25	12.65	0.24	12.47	0.32	12.95	0.26	10.43	1.04
Mn	3.23	0.07	8.34	1.06	11.22	0.10	10.70	0.39	11.17	0.24	9.08	0.89
Fe	0.97	0.05	0.55	0.14	0.73	0.13	0.87	0.13	0.79	0.25	0.61	0.14
Ni	35.78	0.25	46.92	1.89	40.60	0.22	40.31	0.53	40.17	0.32	45.15	1.82
B/A	0.67		1.86		1.87		1.81		1.86		1.88	
e/*a*	6.28		7.17		6.92		6.89		6.90		7.10	

Table D.2: The EDS results for alloy 1 with both 10 % and 25 % added Mn with the atomic percentage of each element, and the % error of the measurement given by the analysis software.

	Average composition										
Sample	Alloy 1-25		N1-25-5		Alloy 1-10		N1-10-5		N1-10-16		N1-10-33
	Mean	% error	Mean	% error	Mean	% error	Mean	% error	Mean	% error	Mean
FeL	1.82	8.18	2.21	7.42	2.24	7.06	1.96	7.05	3.12	3.99	2.85
NiL	26.81	5.94	18.81	6.16	34.12	5.39	34.49	5.22	39.79	3.23	38.47
ZrL	22.47	3.14	22.50	2.98	25.36	3.1	25.13	3	23.77	2.92	28.32
TiK	4.1	6.43	4.84	4.85	5.49	5.29	4.87	5.66	4.82	3.12	4.51
LaL	0.56	28.77	0.66	12.1	1.34	16.25	1.57	15.87	1.18	5.6	0.45
V K	2.75	9.33	4.09	5.67	3.91	6.93	4.17	6.84	3.92	3.35	3.39
MnK	41.49	5.79	46.89	5.4	27.55	5.89	27.82	5.84	23.41	2.91	22.03
B/A	2.69		2.57		2.11		2.17		2.36		2.01
e/a	6.95		6.66		6.99		7.01		7.24		7.11

Table D.3: The EDS results for alloy 1 with both 10 % and 25 % added Mn with the atomic percentage of each element, and the standard deviation.

Main phase

Sample	Alloy 1-25		N1-25-5 bottom		N1-25-5 top		Alloy 1-10		N1-10-5		N1-10-16		N1-10-33	
	Mean	SD	Mean	SD	Mean	SD	Mean	SD	Mean	SD	Mean	SD	Mean	SD
FeL	2.01	0.15	2.11	0.17	3.44	0.18	3.06	0.42	1.98	0.11	3.17	0.16	3.59	0.30
NiL	24.81	1.66	20.29	1.97	22.45	0.17	26.50	2.95	34.41	1.00	39.81	0.44	41.36	0.67
ZrL	22.99	0.42	22.86	0.38	21.75	0.13	25.22	0.13	25.15	0.43	23.68	0.27	22.54	0.48
TiK	3.86	0.30	4.85	0.36	4.13	1.18	4.14	0.33	4.94	0.21	4.82	0.07	5.00	0.07
LaL	0.24	0.06	0.33	0.19	1.02	1.13	0.28	0.04	0.59	0.22	1.26	0.46	0.62	0.19
V K	3.02	0.18	3.71	0.27	3.75	0.13	6.22	0.83	4.37	0.24	3.93	0.17	3.97	0.29
MnK	43.09	1.29	45.85	1.63	43.46	0.22	34.59	1.92	28.56	0.93	23.33	0.43	22.93	0.51
B/A	2.69		2.57		2.72		2.37		2.26		2.36		2.55	
e/a	6.89		6.71		6.82		6.81		7.04		7.24		7.35	

Particles

Sample	Alloy 1-25		N1-25-5 bottom		N1-25-5 top		Alloy 1-10		N1-10-5		N1-10-16		N1-10-33
	Mean	SD	Mean	SD	Mean	SD	Mean	SD	Mean	SD	Mean	SD	Mean
FeL	3.26	0.44	1.91	0.27	3.07	0.90	2.70	1.06	1.84	0.39	3.12	0.22	2.31
NiL	23.67	1.47	18.37	1.21	22.95	0.41	23.08	5.45	25.60	3.26	39.73	0.33	31.90
ZrL	7.64	8.49	19.43	2.06	21.46	0.40	6.99	7.64	20.18	2.08	22.89	0.44	28.32
TiK	1.67	1.45	3.89	0.64	4.33	0.15	2.29	1.98	3.06	0.53	4.67	0.17	3.82
LaL	45.34	24.47	13.21	7.79	1.73	0.82	57.14	19.76	28.80	7.39	2.88	1.22	23.89
V K	1.00	0.85	2.90	0.67	3.56	0.12	1.09	0.96	1.48	0.49	3.71	0.17	2.84
MnK	17.41	14.37	40.29	4.49	42.90	0.84	6.72	7.00	19.04	2.70	22.99	0.48	17.84
B/A	0.83		1.74		2.63		0.51		0.92		2.28		0.98
e/a	5.63		6.28		6.81		5.13		5.91		7.21		6.77

E. Electrochemical Testing Programs

Three different programs were used to test the electrochemical rate performance of the electrodes, and are preseented by the discharge current densities used for the cycling in Table E.1. For the first batch of samples, which were made in Bordeaux, a high rate discharge ability (HRD1) program based on C-rates were used. C rates are defined based on the total capacity of the electrode, and denotes how many hours it takes to discharge the battery. 1 C corresponds to fully discharging the battery in one hour, while 0.1 C corresponds to fully discharging the alloy in 10 hours. To simplify comparisons between the data, average values for the current densities corresponding to the C-rates are also given in the table.

The two other programs were used for the samples casted at NTNU. To be able to study the change in discharge capacity with respect to the applied current density in more detail, the program was spilt into the low rate discharge ability (LRD) program with current densities in the range from 2.4-100 mAg^{-1} and the high rate discharge ability (HRD2) program with current densities from 150-450 mAg^{-1}.

Table E.1: Specification of the applied discharge current densities used for cycling the batteries.

Cycle nr.	LRD	HRD1		HRD2
	[mAg^{-1}]	[C rate]	[mAg^{-1}]	[mAg^{-1}]
1	2.4	0.1	36	150
2	3	0.2	72	200
3	3.6	0.3	107	250
4	5	0.4	143	300
5	7.5	0.5	179	350
6	10	0.6	215	400
7	20	0.7	250	450
8	30	0.8	287	
9	40	0.9	322	
10	50	1	358	
11	60			
12	70			
13	80			
14	90			
15	100			

F. Supplementary Electrochemical Performance Results

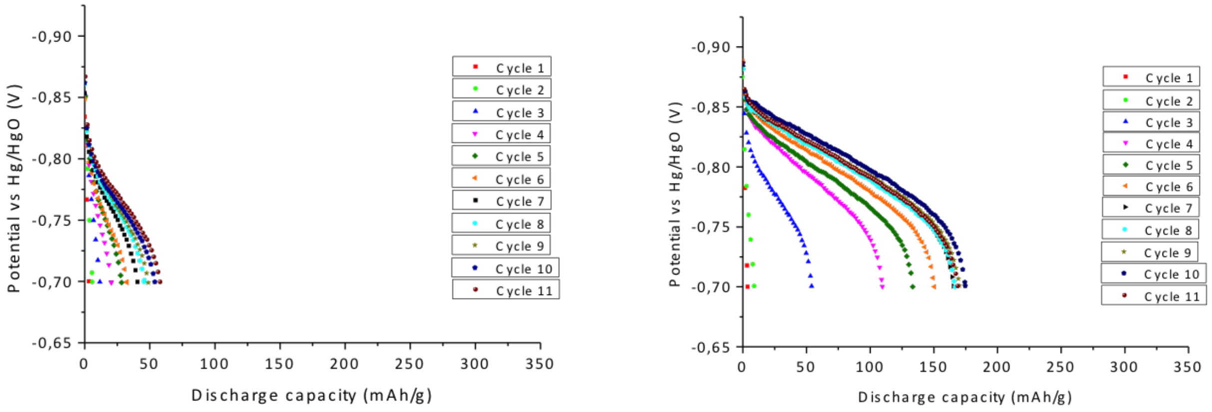

(a) B2-5

(b) B2-16

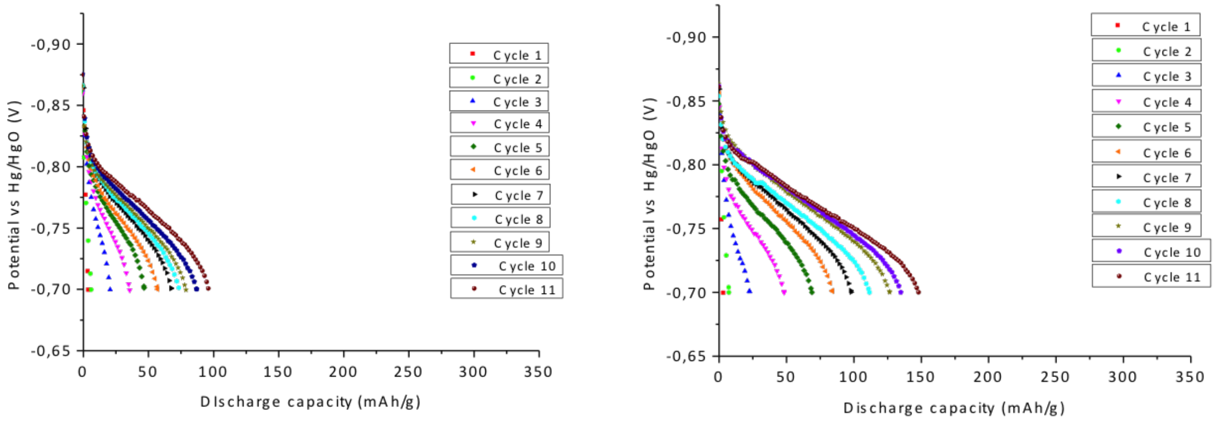

(c) B2-33

(d) B2-100

Figure F.1: The activation performance of alloy 2 melt spun with rotation frequency (a) 5 Hz, (b)16.4 Hz, (c) 33 Hz and (d) 100 Hz.

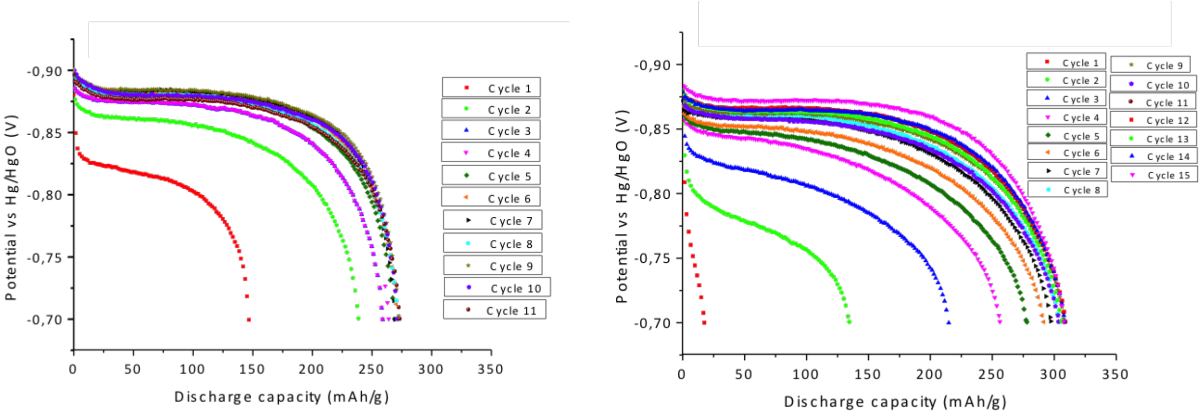

(a) Initial alloy 1-10

(b) N1-10-5

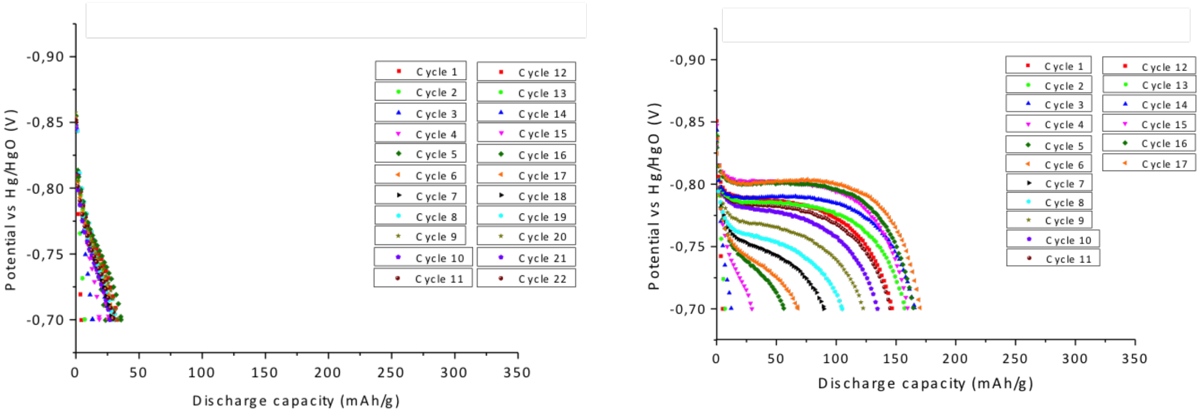

(c) N1-10-16

(d) N1-10-33

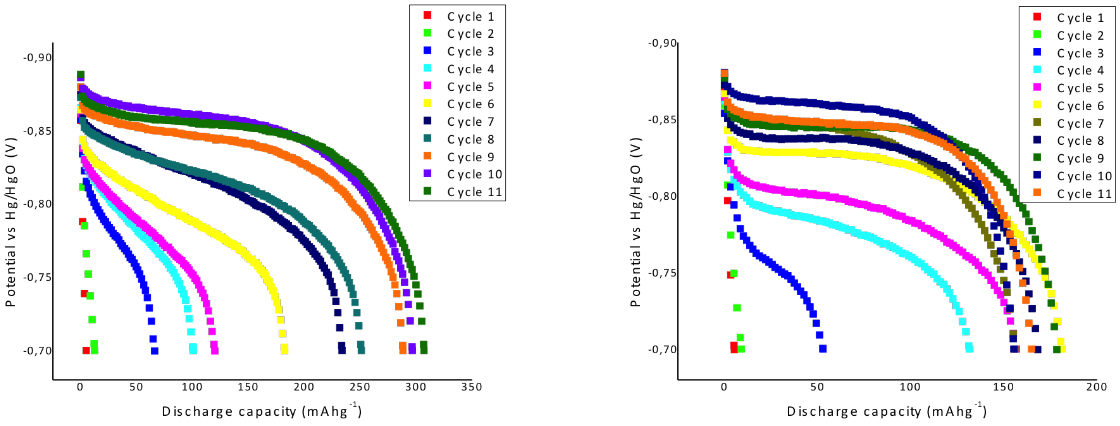

(e) N1-10-16 repeated

(f) N1-10-33 repeated

Figure F.2: The activation graphs for the four samples of alloy 1 with 10 % added Mn, with the 2nd electrodes for the samples N1-10-16 and N1-10-33

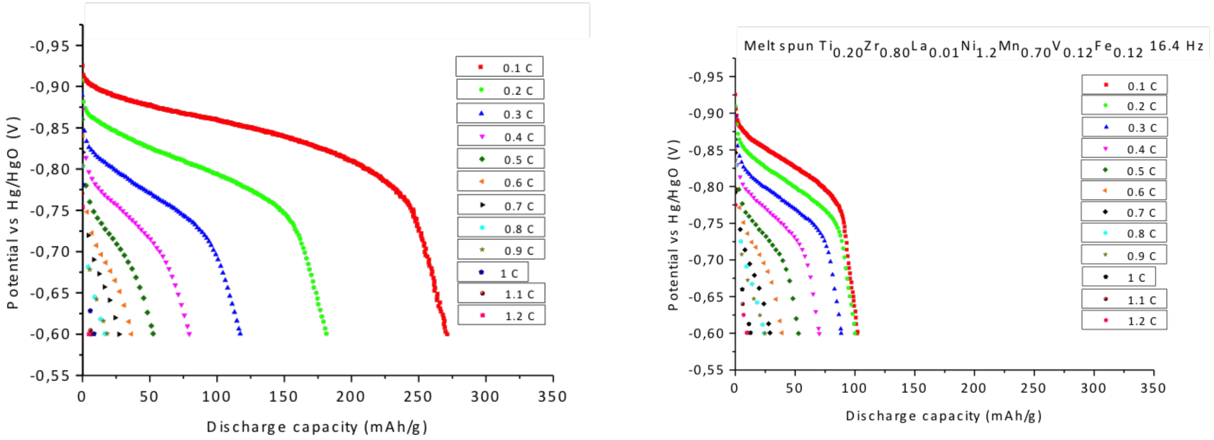

(a) B2-5

(b) B2-16

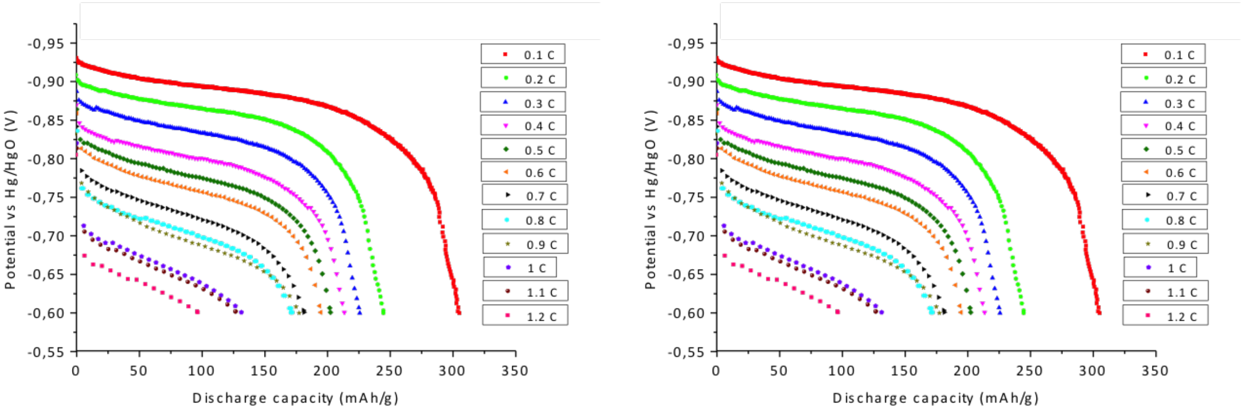

(c) B2-33

(d) B2-100

Figure F.3: The HRD performance of alloy 2 melt spun with rotation frequency (a) 5 Hz, (b)16.4 Hz, (c) 33 Hz and (d) 100 Hz.

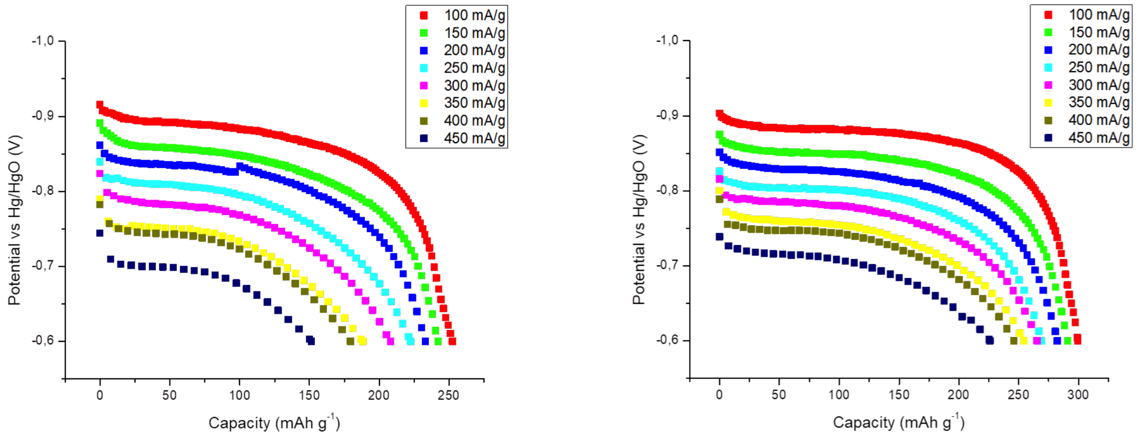

(a) Initial alloy 1-10 **(b)** N1-10-5

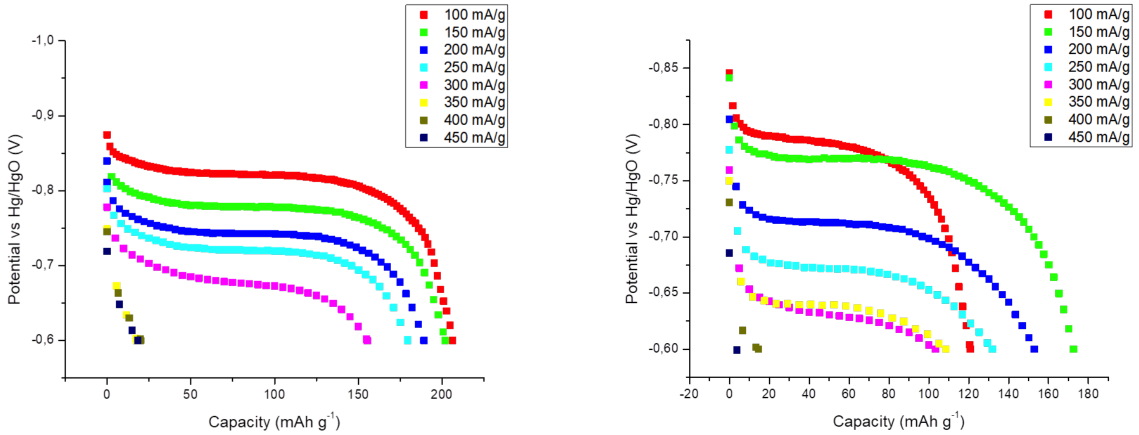

(c) N1-10-16 **(d)** N1-10-33

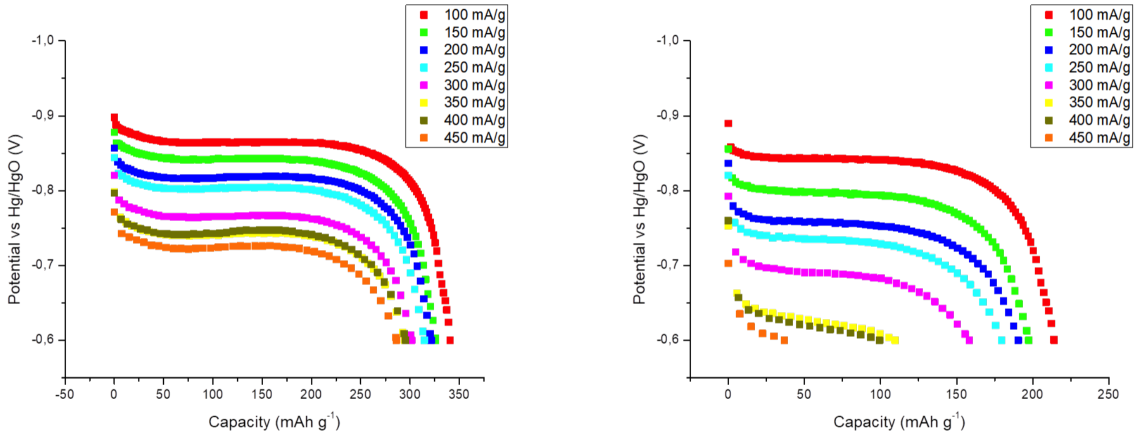

(e) N1-10-16 repeated **(f)** N1-10-33 repeated

Figure F.4: The HRD performance for the four samples of alloy 1 with 10 % added Mn

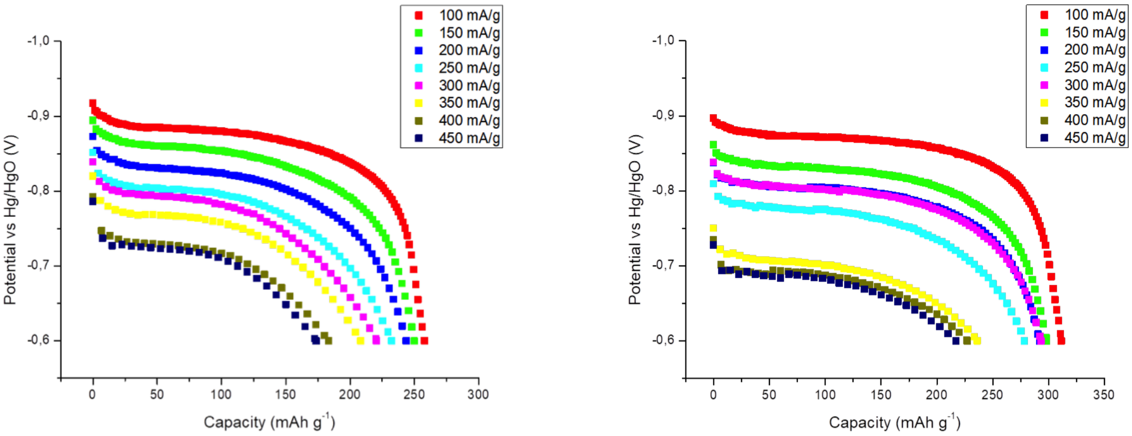

(a) Initial alloy 1-5

(b) N1-5-33

Figure F.5: The HRD performance for the two samples of alloy 1 with 5 % added Mn